Femtosecond Optical Pump-Probe Investigations of Ultrafast Electron and Spin Dynamics in Metals

by

Volodymyr Kruglyak

Submitted to the University of Exeter as a thesis for

the degree of Doctor of Philosophy in Physics,

August 2004.

This thesis is available for the library use on the understanding that it is copyright material and that no quotation from the thesis may be published without proper acknowledgement.

I certify that all material in this thesis which is not my own work has been identified and that no material has previously been submitted and approved for the award of a degree by this or any other University.

…… (signature)

Всем тем, кого я так сильно люблю!

Acknowledgements

If I have seen further it is by standing on the shoulders of giants.

Isaac Newton

It is both a great pleasure and a very difficult task to list here all those who have made this work possible. There is too little room to accommodate all of you on this piece of paper, but be sure that there is always room in my heart and in my memory to cherish all those gold strings of bright moments that will be connecting us forever.

First of all, many thanks to my parents Zinaida and Volodymyr Kruglyak for the great gift of life in this beautiful world full of so nice things and challenging tasks. Thanks to you and to my brother Vladik for your continuous support throughout all of my life. Thanks to my wife Lenochka who is doing so much to build up and to maintain peace in my soul and love in my heart. Thank you for our wonderful son Sanechka, with whom now all my hopes lie. Thanks to all my relatives, including Natalka Petrova, Mama Anya, Papa Yura and all the others who joined our big family later, for trusting in and hopes upon me. Thanks to my numerous friends for… their friendship in its BIG meaning. Separate thanks to Leshka Grashin, Grin Lazovskiy and Natalka Zolotuhina for the music and songs that will never be forgotten. Thanks to all from our small, but nice Ukrainian-Russian community in Exeter. So often you made Lenochka and me to feel as at home!

Thanks to my first teacher Valentina Shumskaya with whose help I solved my first arithmetical problems. Thanks to my school teachers Galina Chalova and Yuriy Chalov with whose help I won my first youth competitions in mathematics and physics. Thanks to my lyceum teachers Dr. Igor Hudyakov and Dr. Andrei Kuchko who gave me

appreciation of physics beyond educational programs. Thanks to all those who helped me to recover after the military service and to return to science. Thanks to all my university lecturers, especially to all those “evil” mathematicians, who so often made me to do more than I wanted to and sometimes even more than I could. Thanks to my railway colleagues, who did not mind me reading physics manuals instead of repairing coaches. Thanks to Alyona Korovnichenko and Prof. Igor Lyubchanskii for having persuaded me to undertake my PhD abroad - in Exeter. Separate thanks to Dr. Andrei Kuchko for continuing collaboration with me, which has already turned out to be so fruitful.

My group in Exeter, thank you all for such a good company! Thanks to Dr. Anjan Barman with whom we shared thoughts and accommodation for more than a year, and with whose help a good half of my field pumping measurements were made. Your name will be mentioned so often here. I thank you and Dr. Ralph Wilks for teaching me *in situ* doing pump-probe experiments. Thanks to my PhD supervisor Dr. Rob Hicken. In fact, this is not just gratitude – I am indebted to you for your time, for your dedication, for your advice, for your encouragement and all those things that constitute the meaning of the word SUPERVISION. No doubts, YOU are the BEST! Separate thanks to him for careful correcting my English style, and to Dr. Ralph Wilks and Paul Keatley for the critical reading of the manuscript and useful corrections and comments.

At last but not least, thanks to the University of Exeter and the Overseas Research Studentship scheme for the provision of funding for my PhD.

Abstract

In this thesis, the results of pump-probe investigations of electron and spin dynamics in thin film metallic samples are presented. The sample is stimulated by either an optically triggered magnetic field pulse or an intense light pulse. The sample response is probed by means of a stroboscopic measurement of the changes in either the intensity or the polarization state of a delayed light pulse (probe).

Due to the Magneto Optical Kerr Effect, this experimental technique is sensitive to small amplitude deflections of the magnetisation from the ground state. The magnetisation dynamics of small magnetic elements and element arrays were investigated by means of time resolved optical measurements and micromagnetic simulations. Most of the modes observed from the submicron elements could be identified as falling on two branches characterised by different frequencies. The micromagnetic simulations showed that the magnetisation dynamics are nonuniform, and so the frequencies and relative amplitudes of the modes from the two branches are determined by the interplay between the exchange and demagnetising fields. In particular, it was found that the dynamics are nonuniform even in the 64 nm element, where the dominant mode is confined by the demagnetising field within the edge regions of the element. Also, a theory of precessional magnetisation dynamics and relaxation in an exchange coupled magnetic double layer element of rectangular shape was developed in the macrospin approximation.

Using the optical pumping configuration with an elliptically polarised pump, the transient polarisation due to the Specular Inverse Faraday Effect and the Specular Optical Kerr Effect were simultaneously observed in thin films of Au, Cu, Ag, Ni, Pd, Ti, Zr, and Hf under identical experimental conditions. The magnitudes of the time

resolved signals were used to extract the real and imaginary parts of the non-vanishing components of the third-order optical susceptibility tensor. The temporal shapes of the signals were used to extract characteristic time scales for the decay of the transient polarisation, which were interpreted in terms of scattering of linear and angular momentum of hot electrons. A systematic variation of the signal magnitudes, the temporal shapes, and the extracted tensor components was observed between different metals that reflects their underlying band structure.

The optical pumping measurements were also used to detect the transient reflectivity of the samples listed above. By fitting the time resolved signals to analytical solutions of the two temperature model equations in the high and low perturbation limits, characteristic time scales for the electron-electron and electron-phonon thermalisation were derived. Two colour time resolved measurements, using a white light continuum pulse as the probe, were performed upon an Au thin film, allowing transient reflectivity spectra to be recorded for different values of the pump-probe time delay. The data may allow the dependence of the reflectivity upon the electron distribution function to be determined, and hence provide a means of determining the latter as a function of the time delay without introducing any assumptions about transient electron dynamics.

List of Contents

List of Figures

List of Tables

Declaration

Если ж в партию сгрудились малые,

Сдайся, враг,

Замри и ляг!

В. В. Маяковский[a]

This work represents the result of the joint effort of many people. The contributions of my colleagues to the research presented in this thesis are outlined below and will be acknowledged more specifically throughout the main text of the thesis.

Chapter 1. Background

The chapter represents my own work apart from a few Figures taken from works published by our group and other authors. All the Figures are clearly identified and the sources are referenced.

Chapter 2. Technique of Pump-Probe Experiments

The chapter represents my own work apart from the time resolved electro-optic data (Figure 2.4 (a) and (b)). I must also note that the experimental basis for time resolved measurements in Exeter had been built up by Dr. R.J. Hicken, Dr. J. Wu and Dr. R. Wilks before I started my PhD project. Dr. A. Barman constructed the time-resolved Kerr microscope. The two-colour optical pump-probe apparatus at the Rutherford Appleton Laboratory was set up by Dr. P. Matousek and Dr. M. Towrie.

---

[a] ***If little ones have joined into a party,***

Surrender, Enemy,

Stand still, and lie down!

Chapter 3. Theory of Uniform Mode Magnetisation Dynamics in Rectangular Double Layer Ferromagnetic Elements

The theory of uniform modes of a coupled ferromagnetic double layer element of square shape was developed by myself, although Dr. R.J. Hicken had solved a similar but less general problem in a slightly different way before me. The Figures used to illustrate an application of the theory to the experimental data were taken from works that were published by our group and are clearly referenced in the thesis. The time resolved measurements in those papers were performed by Dr. A. Barman and myself, with approximately equal contributions from two of us. The data analysis based upon the macrospin model was performed by Dr. A. Barman and myself.

Chapter 4. Time Resolved Scanning Kerr Microscopy Investigation of Spin Wave Excitations in Ultrasmall Magnetic Elements and Arrays

The samples and the transmission line structures were prepared by Dr. J.R. Childress and Dr. J.A. Katine from Hitachi Global Storage Technologies. The photoconductive switches were made Dr. J. Scott and Dr. M. Rahman from the University of Glasgow. Dr. A. Barman assembled the structure and performed some preliminary measurements on the 6 μm element. The rest of the measurements were performed by myself. The data analyses including the OOMMF simulations were performed by myself.

Chapter 5. Measurement of Hot Electron Momentum Relaxation Times and Third Order Nonlinear Susceptibility Tensor Components in Metals by Femtosecond Ellipsometry, and Chapter 6. Transient Temperature Dynamics

The samples were prepared by Dr. M. Ali and Prof. B. J. Hickey from the University of Leeds. Mr. A. T. G. Pym and Prof. B. K. Tanner from the University of

Durham performed X-ray analysis of the samples. I set up the single colour optical experiment and performed the measurements and the data analysis. Dr. P. Matousek and Dr. M. Towrie from the Rutherford Appleton Laboratory in Oxford set up the two colour experiment and helped me to perform the measurements. In both cases, I performed the data analyses using a theoretical model that I developed myself.

The Labview software used for data acquisition in the time resolved measurements was written by Dr. R. Wilks.

It is not possible to describe the contribution to this work by my PhD supervisor Dr. R.J. Hicken, since it is present in every part of this thesis.

Introduction

Есть только Миг между прошлым и будущим,

И этот Миг называется Жизнь!

Леонид Дербенев[a]

A characteristic feature of progress in modern solid state physics is the continuous revision of the notion of an instant. Indeed, processes that had always been assumed in classical physics to be infinitesimally short are now being accessed. The weapon of victory is an ultrashort light pulse that can be produced by modern lasers[1], and the strategy is the pump-probe measurement scheme[2]. The essence of the latter is that a sample is excited by either an intense light or magnetic field pump pulse, and the resulting dynamics are sensed by measuring changes in the energy and polarisation state of a delayed probe pulse reflected from the sample. In more involved techniques, electrons emitted to vacuum[3], or second harmonic light[4] have to be collected. While providing important information about various aspects of fundamental physics, including the mode spectrum of ultrasmall magnetic elements[5,6], and the strength and characteristic time scales of the interaction among electrons, phonons, magnons, and other quasiparticles[7-11], progress in ultrafast investigations is stimulated by the promise of a wealth of applications in future electronic devices[12-14].

The magnetic recording industry is the main benefactor of the results of ultrafast studies of magnetic systems, although other opportunities exist for their use within communication technology. The continuing trend towards storing larger amounts of

---

[a] ***There is just an Instant between the Past and the Future,***

And this Instant is what is called Life.

L. Derbenev

data has led to the reduction of bit and transducer sizes, on one hand, and to increased record and replay rates, on the other. At present, information in magnetic data storage devices is encrypted as the orientation of the in-plane magnetisation of small regions of a continuous magnetic film[15]. The writing process is accomplished through the application of a magnetic field in the direction opposite to that of the magnetisation, and proceeds via thermally assisted switching on time scales of nanoseconds. A faster recording scheme has been recently demonstrated that is characterized by precessional motion of the magnetisation of a small magnetic element on time scales of a few hundreds of picoseconds[16,17]. However, before this technique can be implemented in working data storage devices, several issues, including the coherence of the precessional switching[5,18] and the origin of the magnetic damping[19,20], are to be resolved.

Discovery of the ultrafast demagnetisation phenomenon[21] promised a further increase of the recording speed. This relies upon the collapse of the spontaneous magnetisation following the absorption of an ultrashort laser pulse[22]. The magnetisation vector may then recover in a new direction in a suitably applied small magnetic field[23]. For the latter, a circularly polarized light pulse might be used[24], in which case an all-optical magnetic switching would take place. Alternatively, the laser pulse may be used to locally induce a less drastic modification of magnetic parameters of the recording medium, such as the anisotropy[25,26] or the exchange bias[27]. The magnetisation reversal of the modified volume is then completed by application of a magnetic field pulse with amplitude that is too small to affect the unpumped volume of the medium. This technique has been called heat assisted magnetic recording[28]. A key issue for both of these approaches is the development of efficient sinks for the excess heat.

In this thesis, the results of my honest endeavours to further shorten the notion of an instant are presented. Once again, I want to note that these are results of collaborative research, and the contributions of my colleagues will be acknowledged in

the appropriate places within the thesis. I decided to include to the thesis only those results the major part of which was obtained solely by me. Hence, results of my field pumping experiments that were published in Ref. 6,29-34 do not constitute a separate chapter in this thesis, although I have performed about a half of the time resolved measurements for those papers. However, I use some of the data, as well as other data that are not presented separately in the thesis, for the purpose of illustration in the first two chapters, and for the testing of the theoretical model developed in chapter 3.

In chapter 1, the general physical background of my study is introduced. I start from a discussion of the physics of ferromagnetism and spin waves in micron sized magnetic elements. The basic equations and formulae are presented, including the Landau-Lifshitz equations of motion of the magnetisation and the Kittel formula. As the theory of the magnetisation dynamics in small magnetic elements is very complicated, I use both time resolved scanning Kerr microscopy and micromagnetic simulation images in order to introduce the reader into this field of magnetism. I continue with a short discussion of the physics of the interaction between short light pulses and matter in which the two-temperature model equations and the formulae describing the third order nonlinear polarisation effects in metals are introduced.

Chapter 2 is devoted to the description of the pump-probe apparatus used in the experiments. Special attention is paid to the discussion of the experimental artefacts that may be present in pump-probe measurements, and of the means of their separation from the measured signal.

In chapter 3, a theory of uniform mode magnetisation dynamics in double layer ferromagnetic elements of rectangular shape is developed. Analytical results for the dependence of the mode frequencies and damping, and the signal shapes in the time and frequency domains upon the magnitude and direction of the bias magnetic field are obtained in the macrospin approximation.

Chapter 4 is devoted to investigations of magnetisation dynamics in arrays of square magnetic elements. First, I present results of time resolved scanning Kerr microscopy experiments on a 6 μm element and square 4 μm arrays of sub-micron sized elements that were made of permalloy and had thickness of 2.5 nm. The elements of sub-micron size possessed modes with frequencies that differed from the macrospin prediction. Using the micromagnetic simulations performed for single elements of the same size, the frequencies could be identified as localized spin wave modes.

In chapter 5, I present results of time resolved ellipsometric measurements made upon Au, Cu, Ag, Ni, Pd, Ti, Zr, and Hf thin films. Using an elliptically polarised pump beam, the decay of the optically induced polarisation of the sample was observed. Characteristic relaxation times were extracted and interpreted in terms of scattering of linear and angular momentum of hot electrons through the application of a specially developed model. Also, the components of the third order optical susceptibility tensor are extracted. A systematic variation is observed between different metals that reflects their underlying band structure.

In chapter 6, I study time resolved reflectivity signals from the samples described in the previous chapter. I derive two analytical solutions of the two temperature model equations corresponding to the low and high perturbation limits, and apply them to the transient reflectivity signal, assuming proportionality between the transient reflectivity and electron temperature. This allowed the electron-electron and electron-phonon thermalization times of the samples to be extracted. Finally, two-colour TR experiments with a white light continuum pulse as the probe are described with the aim of understanding limits of applicability of the above made assumption of the proportionality between the transient reflectivity and electron temperature.

Chapter 1. Background

In this chapter, the physics underlying the phenomena studied in this thesis will be introduced.

1.1 Ferromagnetism

1.1.1 Ferromagnetism: Decisive Steps

Although it has been known since ancient times that some materials possess magnetic properties, the idea that magnetic materials contain smaller magnets, representing "molecular currents", was only introduced in the 19th century by Ampere[35]. The first quantitative theories of paramagnetism and ferromagnetism were developed in the 20th century by Langevin[36] and Weiss[37], respectively. The quantum mechanical nature of the Weiss molecular field was discovered twenty years later by Heisenberg[38], Dorfman[39] and Frenkel[40]. They showed that the molecular field is a crude representation of a more complicated exchange interaction. The latter originates in electrostatics and the Pauli exclusion principle. It was realised later that the magnetic anisotropy (Akulov[41], Becker[42], Honda and Kaya[43]) and the magneto-dipole interaction (Frenkel and Dorfman[44], Bloch[45], Heisenberg[46]) must be also taken into account in order to explain the domain structures observed in ferromagnets.

The decisive step was taken by Landau and Lifshitz[47] in 1935, who applied the variational principle to obtain a phenomenological description of the statics, dynamics and the relaxation of magnetisation of a magnetic body. According to this principle, the

equilibrium spatial distribution of the magnetisation **M**(**r**) corresponds to a minimum of the total free energy of the body. This approach was developed further by Brown[48]. All observed domain patterns could in principle be predicted from Brown's differential (so-called micromagnetic) equations[49]

$$\mathbf{M}\times\mathbf{H}_{\mathrm{E}}=0, \tag{1.1.1}$$

where $\mathbf{H}_{\mathrm{E}}$ is the effective field, defined as the functional derivative of the density of the free energy w with respect to **M**

$$\mathbf{H}_{\mathrm{E}}=-\frac{\delta w}{\delta \mathbf{M}}. \tag{1.1.2}$$

It follows from equation (1.1.1) that in equilibrium the magnetisation is aligned parallel to the effective magnetic field.

1.1.2 Energetics of Ferromagnetism

The static configuration of the magnetisation and, as we will see, its dynamics and relaxation are determined by the interplay between the different energy contributions to the total free energy w in the expression for the effective magnetic field (1.1.2). Both the material parameters and the shape and size of the system are important. The latter control fine features of the interplay between the exchange and dipolar interactions.

In a ferromagnetic material, the magnetic moments of individual atoms are strongly coupled and aligned by the exchange interaction. Hence, the material may possess a finite magnetisation even in the absence of any external magnetic field. The exchange energy density term w_{ex} may be defined phenomenologically as[50]

$$w_{\mathrm{ex}}=\sum_{i,j=1,2,3}A_{i,j}\left(\frac{\partial \mathbf{u}}{\partial x_i}\cdot\frac{\partial \mathbf{u}}{\partial x_j}\right), \tag{1.1.3}$$

where $A_{i,j}$ is the exchange stiffness constant and x_i are the Cartesian coordinates.

When the temperature is increased above the Curie temperature[51], the exchange energy becomes comparable to and then smaller than the kinetic energy of atoms[50]. The

spontaneous magnetisation disappears and the material becomes paramagnetic. Below the Curie temperature, a ferromagnetic specimen does not necessarily exhibit a macroscopic magnetic moment in the absence of an applied field. This is explained by the existence of magnetic domains[35]. The magnetisation inside each domain is aligned but the relative alignment of the different domains depends upon the magnetic history of the sample. This phenomenon is called magnetic hysteresis[52]. In particular, the magnetic moments of neighbouring domains may be aligned antiparallel so as to minimise the magneto-dipole contribution to the magnetic free energy. In this case, the entire specimen may have zero net magnetic moment.

The magnetodipole interaction is the magnetostatic interaction of the magnetic dipoles of atoms[49,53]. It plays a major role in ferromagnets in spite of the fact that it is several orders of magnitude weaker than the exchange interaction[50]. Because of the isotropy of the latter, the magneto-dipole interaction together with the magnetic anisotropy defines the non-uniform distribution of the magnetisation, i.e. the domain structure[35,a]. Its energy density may be written as

$$w_{\mathrm{md}} = -\frac{1}{2}\mathbf{H}_d \cdot \mathbf{M}, \tag{1.1.4}$$

where $\mathbf{H}_d = -\nabla\tilde{\varphi}$ is the demagnetising field and the magnetostatic potential $\tilde{\varphi}$ is determined from

$$\tilde{\varphi}(\mathbf{r}) = \int d\mathbf{r}' \left(\mathbf{M}(\mathbf{r}') \cdot \nabla_{\mathbf{r}'} \frac{1}{|\mathbf{r} - \mathbf{r}'|} \right), \tag{1.1.5}$$

where the integration is performed over the volume of the sample[50]. One of the most important features of the magneto-dipole energy is its long range nature. This means that its density is not a characteristic of the local magnetic state, but is defined by the

[a] The magnetodipole interaction becomes important on length scales greater that the so-called exchange length defined as $l_{ex} = \sqrt{A_{i,j} / 2\pi M^2}$ [35].

magnetic state of the entire sample, which involves additional integration[49]. It can be shown that the demagnetising field defined above represents a rigorous solution of the magnetostatic Maxwell equations[50].

For a uniformly magnetised sample, the demagnetising field can be represented as

$$\mathbf{H}_d(\mathbf{r}) = -\hat{\mathbf{N}}(r)\cdot\mathbf{M}, \tag{1.1.6}$$

where the demagnetising tensor is defined as

$$\hat{N}_{ij}(\mathbf{r}) = -\frac{\partial^2}{\partial x_i \partial x_j}\int \frac{d\mathbf{r}'}{|\mathbf{r}-\mathbf{r}'|}. \tag{1.1.7}$$

For a sample with the ellipsoidal shape, components of the tensor are constants and the demagnetising field is uniform across the sample[50]. Since the components of the demagnetising tensor are generally not equal, the demagnetising field is different for different orientations of the sample magnetisation, giving rise to the magnetic shape anisotropy. For an infinitesimally thin magnetic film, the shape of which can be considered as a limiting case of an ellipsoid, the energy density of the shape anisotropy can be written in a simple form[50]

$$w_f = 2\pi M^2(\mathbf{u}\cdot\mathbf{n})^2. \tag{1.1.8}$$

In a non-ellipsoidal sample, the shape anisotropy is also present, but has a much more involved character, as the magnetisation is generally not uniform in this case[49]. The demagnetising field varies strongly across the sample, which makes analysis of static and dynamic phenomena in such samples very complicated.

There are also other types of the magnetic anisotropy such as the crystalline, strain-induced, and surface anisotropies[12]. In bulk materials, the magnetisation is more easily saturated along certain crystallographic axes, which are called easy axes. This effect is due to the magneto-crystalline anisotropy. For instance, in magnets of cubic symmetry there are three mutually perpendicular easy axes, while for hexagonal symmetry, the easy axis lies along the hexagonal c-axis[54]. In thin magnetic films, the

magnetic anisotropy is very different from that in bulk materials because of the broken symmetry of surfaces and interfaces, and the strains induced either by the mismatch between the film and substrate lattice structures, or by magnetic field applied during the sample growth. For a discussion of the magneto-crystalline anisotropy in thin magnetic films see Chapter 2 of Ref. 55.

The main source of these types of the magnetic anisotropy in a thin film is the spin-orbit interaction that couples the total magnetic moment (spin plus orbital) to the crystal axes[50]. The lower symmetry at the surface of the ultrathin film strongly modifies this interaction, leading to the surface anisotropy[50]. Together with the overlap of the neighbouring atom's wave functions, the spin-orbit interaction is also responsible for the magneto-elastic or magnetostrictive anisotropy when the system is strained[50].

The most frequently observed anisotropies are the uniaxial anisotropy with energy density

$$w_2 = -K_2(\mathbf{u}\cdot\mathbf{k})^2, \tag{1.1.9}$$

and surface anisotropy which in the limit of an infinitesimally thin film has energy density

$$w_S = -\frac{2K_s}{d}(\mathbf{u}\cdot\mathbf{n})^2, \tag{1.1.10}$$

where d, K_2 and K_s are the film thickness, and the uniaxial and surface anisotropy constants, respectively. The unit vectors **k** and **n** are parallel to the uniaxial anisotropy easy axis and the film normal, respectively. The energies of the surface and thin film shape anisotropy have the same form, and are difficult to distinguish. Hence, a single effective shape anisotropy term is often used

$$w_{eff} = 2\pi M_{eff}{}^2(\mathbf{u}\cdot\mathbf{n})^2, \tag{1.1.11}$$

where M_{eff} is the effective sample magnetisation[50].

Finally, the energy density due to an external magnetic field is given by the Zeeman term

$$w_{\mathrm{Z}} = -\mathbf{H}\cdot\mathbf{M}. \tag{1.1.12}$$

The external field **H** in this expression may have various origins. For example, it may be a static bias field, a time dependent pulsed or harmonic field, or an exchange bias field. The latter is a representation of a more complicated effect caused by the presence of an antiferromagnetic layer in a multilayer sample. The antiferromagnetic layer causes the magnetisation of a neighbouring ferromagnetic layer to point in a particular direction when other effective fields are absent[15]. It is important to remember that the exchange bias is an interfacial effect, and its strength is inversely proportional to the magnetic film thickness.

1.1.3 Equation of Motion of Magnetisation

The magnetisation dynamics and relaxation due to the influence of forces that act to reduce the net free energy of the ferromagnet[19] are described by the Landau-Lifshitz equation[56]

$$\frac{\partial\mathbf{M}}{\partial t} = -\gamma[\mathbf{M}\times\mathbf{H}_{\mathrm{E}}] + \mathbf{R}, \tag{1.1.13}$$

where $\gamma = g\mu_{\mathrm{B}}/\hbar$ is the magnetomechanical ratio, g is the Landé g-factor, μ_{B} is the Bohr magneton, $\hbar$ is the Planck constant, and the most general form of the relaxation term is given by

$$\mathbf{R} = \hat{\boldsymbol{\lambda}}_1\mathbf{H}_{\mathrm{E}} - (\nabla\hat{\boldsymbol{\lambda}}_2\cdot\nabla)\mathbf{H}_{\mathrm{E}}, \tag{1.1.14}$$

where $\hat{\boldsymbol{\lambda}}_1$ and $\hat{\boldsymbol{\lambda}}_2$ are the relaxation tensors[19,50]. For a description of processes that preserve the magnitude of the magnetisation, this may be reduced to either the Landau-Lifshitz[47]

$$\mathbf{R}_{\mathrm{L}} = -\frac{\lambda}{M^2}[\mathbf{M}\times[\mathbf{M}\times\mathbf{H}_{\mathrm{E}}]], \tag{1.1.15}$$

or Gilbert[57]

$$\mathbf{R}_{\mathrm{G}} = \frac{\alpha}{M}\left[\mathbf{M} \times \frac{\partial \mathbf{M}}{\partial t}\right] \tag{1.1.16}$$

form, where λ and α are the Landau and Gilbert damping constants, respectively. The two relaxation terms are equivalent in the limit of small damping[19].

As shown in Figure 1.1, the first term on the right hand side of equation (1.1.13) makes the magnetisation precess around the effective field vector, while the second (relaxation) term, which is assumed to be of the Landau form, makes it relax towards the instantaneous equilibrium direction that is parallel to the effective field vector. Note that the damping constants are usually very small so that the relaxation term has a much smaller magnitude than shown in Figure 1.1.

For a description of phenomena with a varying magnetisation magnitude, such as heat assisted magnetic recording[23], the modified Bloch equation (also known as the Bloch-Bloembergen equation) may be used[56].

1.1.4 Kittel Formula

According to equation (1.1.13), after having been displaced from the equilibrium orientation, the sample magnetisation begins to precess about the direction of the

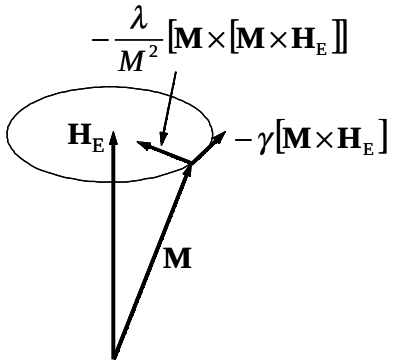

Figure 1.1 Directions of the different vectors in the Landau-Lifshitz equation with a relaxation term of the Landau form are sketched.

instantaneous effective field, as shown in Figure 1.1. The precession may be spatially nonuniform. Any spatial nonuniformity can be represented as a superposition of Fourier components with different wavelengths. These components are known as spin waves[54]. The frequency of the spin wave depends upon the wavelength, and its calculation is generally a difficult task. However, the calculation becomes much simpler in the case of a body with uniform static magnetisation.

Let us consider an ellipsoid uniformly magnetised in the direction of a uniform constant external field **H** that is parallel to one of the axes of the ellipsoid. The demagnetising tensor (1.1.7) then becomes diagonal, and the frequency of the spatially uniform precession, in the absence of magnetic anisotropies other than the shape anisotropy, is given by the famous Kittel formula[58]

$$\omega = \gamma\sqrt{(H + (N_{xx} - N_{zz})M)(H + (N_{yy} - N_{zz})M)}\,, \qquad (1.1.17)$$

where the coordinate system is chosen so the z-axis is parallel to the applied field. For a thin film magnetised within its own plane, this formula reduces to

$$\omega = \gamma\sqrt{H(H + 4\pi M)}\,. \qquad (1.1.18)$$

As one can see the exchange interaction does not affect the uniform precession since the exchange energy (1.1.3) vanishes in this case.

1.1.5 Magnetostatic Wave Modes in Ferromagnetic Films

The wavelength of spin wave modes excited within a particular sample scales with the characteristic size of the nonuniformities of the internal effective field[59]. The latter in a patterned element are caused by the nonuniformities of the internal demagnetising field and scale with the element size. Hence, for an element of micron size the wavelengths of spin wave modes will be about 1 μm, which is long compared to the interatomic spacing. In this regime, the exchange interaction is of lesser importance than the magnetodipole interaction, and can be neglected in the first order

approximation. The modes excited under these conditions are known as magnetostatic or Walker modes[60].

The magnetostatic modes of an infinite ferromagnetic slab were studied first by Damon and Eshbach[61]. They represented the sample magnetisation as a sum of the saturation magnetisation in the z-direction, the ground state of the system, and a small time dependent perturbation. Hence, the internal magnetic field was the sum of the static field and the dynamic dipole field generated by the time dependent part of the magnetisation. By solving the Landau-Lifshitz equation and Maxwell magnetostatic equations[56] with appropriate boundary conditions, they obtained a general solution of the problem. The spectrum of the magnetostatic modes is graphically presented in Figure 1.2.

The spectrum consists of a surface mode and a manifold of volume modes. For zero wave number, the modes converge to the uniform mode. The mode with an in-plane wave vector perpendicular to the static magnetisation is called the surface or Damon-Eshbach mode. The component of the wave vector of this mode that is

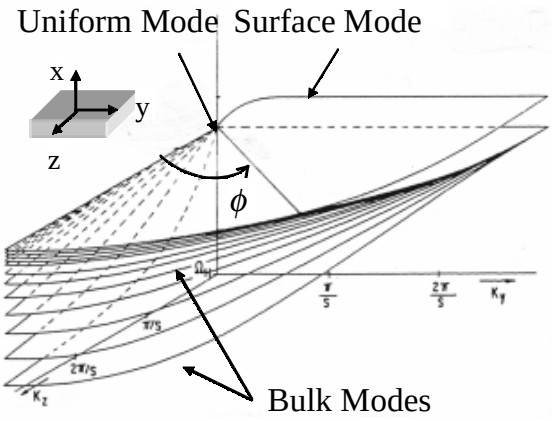

Figure 1.2 The Damon-Eshbach spectrum of magnetostatic waves is plotted (taken from Ref. 61). The coordinate system used in the calculation is also shown in the inset.

perpendicular to the film plane is imaginary, and the amplitude of the oscillation decays from the surface to the bulk of the film. The modes with an in-plane wave vector parallel to the static magnetisation are known as backward volume magnetostatic wave modes. Their wave vector component that is perpendicular to the film plane is real, and the amplitude of the oscillation in these modes can be greater in the bulk of the film than near the surface. They are called "backward" because their frequency decreases as the wave number increases, and hence the group velocity is negative.

1.1.6 Spin Waves in Ferromagnetic Elements. Time Resolved Scanning Kerr Microscopy and Numerical Micromagnetic Simulations

Magnetisation dynamics in small elements of non-ellipsoidal shape are very different and much more complicated. However, they may be investigated experimentally by time resolved scanning Kerr microscopy (TRSKM) and theoretically by numerically solving the Landau-Lifshitz equation using finite difference methods.

Figure 1.3 shows images of the distribution of the out-of-plane component of the magnetisation in a 10 μm square permalloy element of 150 nm thickness acquired at different times after excitation of the sample by a small in-plane pulsed magnetic field[31]. The grey scale represents the instantaneous value of the out of plane component of the magnetisation, so that black and white correspond to the magnetisation tilting in and out of plane. One can see that for the static field of 288 Oe the precession is initially uniform with nonuniformity developing from the edges as seen in the image at 170 ps. At later times a regular pattern of stripes forms with an antinode at the centre of the element (880 ps). The amplitude of the precession decays with time, and the contrast in the image at 1440 ps is seen to be decreased. The wave vector of the nonuniform magnetisation is perpendicular to the stripes and hence parallel to the applied static magnetic field. This suggests that the stripes are associated with backward volume magnetostatic waves excited in the sample. For the static field of 76 Oe, the precession

is nonuniform from the outset. The image at 100 ps suggests that a domain structure is present before the pulsed field is applied. The magnetisation dynamics begin by moving orthogonal to the in-plane pulsed field and the static magnetisation. The magnetisation may be deflected either in or out of the film plane within the different domains and so a strong contrast is observed within the dynamic image. At time delays of 200 and 950 ps the image shows an increasingly irregular pattern of contrast throughout the entire area of the element.

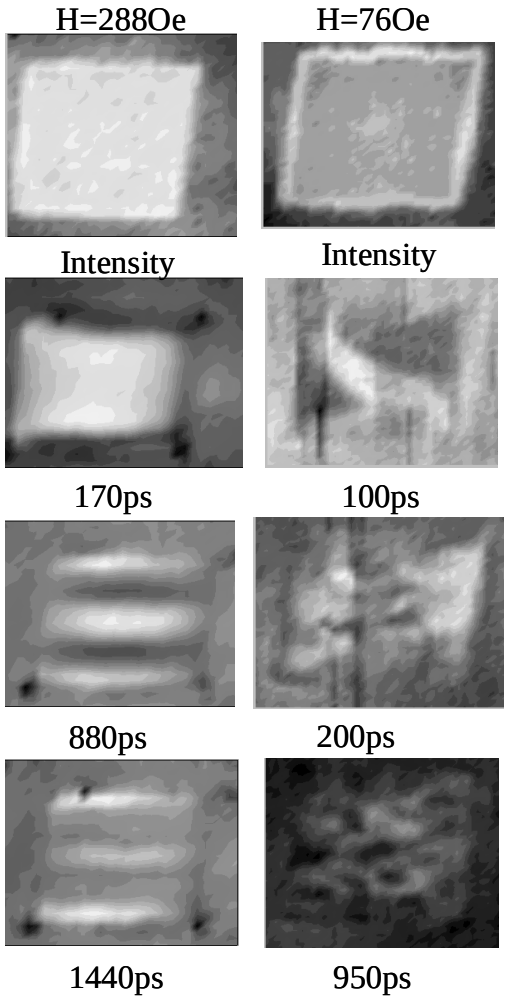

Figure 1.3 An intensity image and series of TRSKM images of the out of plane component of the magnetisation distribution at different pump-probe time delays are shown for two values of the static magnetic field applied in the vertical direction (taken from Ref. 31).

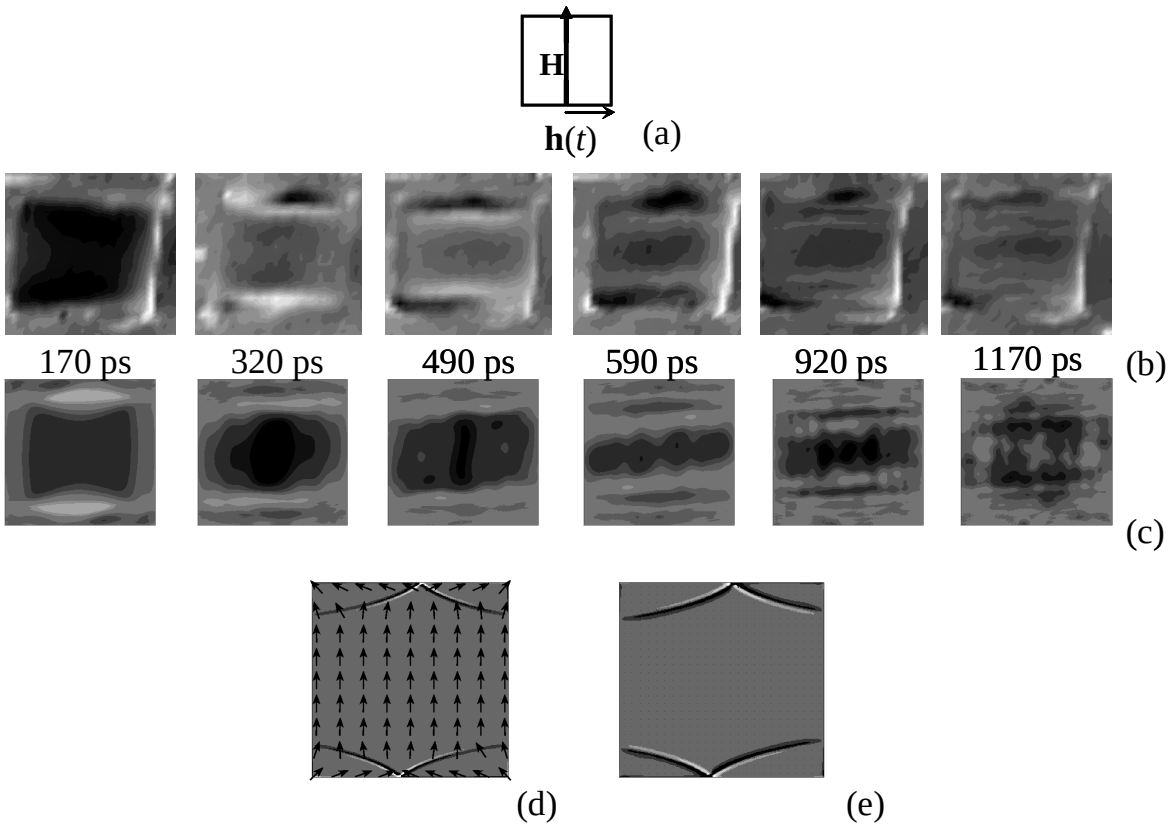

Figure 1.4 A series of TRSKM images of the out of plane component of the magnetisation distribution at different pump-probe time delays (b) are compared with OOMMF micromagnetic simulations (c) for the static and pulsed magnetic fields as shown in (a). The static magnetisation (d) and effective field (e) are also shown (taken from Ref. 33).

The micromagnetic simulations qualitatively reproduce the observed magnetic images. In order to illustrate this, Figure 1.4 (b) and Figure 1.5 (b) show experimental images of the distribution of the out-of-plane component of the magnetisation in the same element acquired at different times after excitation of the sample by a small in-plane pulsed magnetic field[33]. The relative orientation of the static and pulsed magnetic fields is shown in Figure 1.4 (a) and Figure 1.5 (a). Figure 1.4 (c) and Figure 1.5 (c) show the distributions of the out-of-plane component of the magnetisation in the element simulated using the object oriented micromagnetic framework (OOMMF)

package[62]. Using OOMMF, one can also simulate the static distributions of the magnetisation and the effective field in the element that are shown in Figure 1.4 (d) and Figure 1.5 (d), and Figure 1.4 (e) and Figure 1.5 (e), respectively. These allow us to understand why the magnetisation dynamics are different when the static field is applied parallel to an edge and a diagonal. In the latter case, the effective field is very nonuniform at the centre of the element, and the nonuniformity of the magnetisation propagates from the centre towards the corners of the element. In the case of the static field parallel to the edge, the effective field is nonuniform in the vicinity of the element

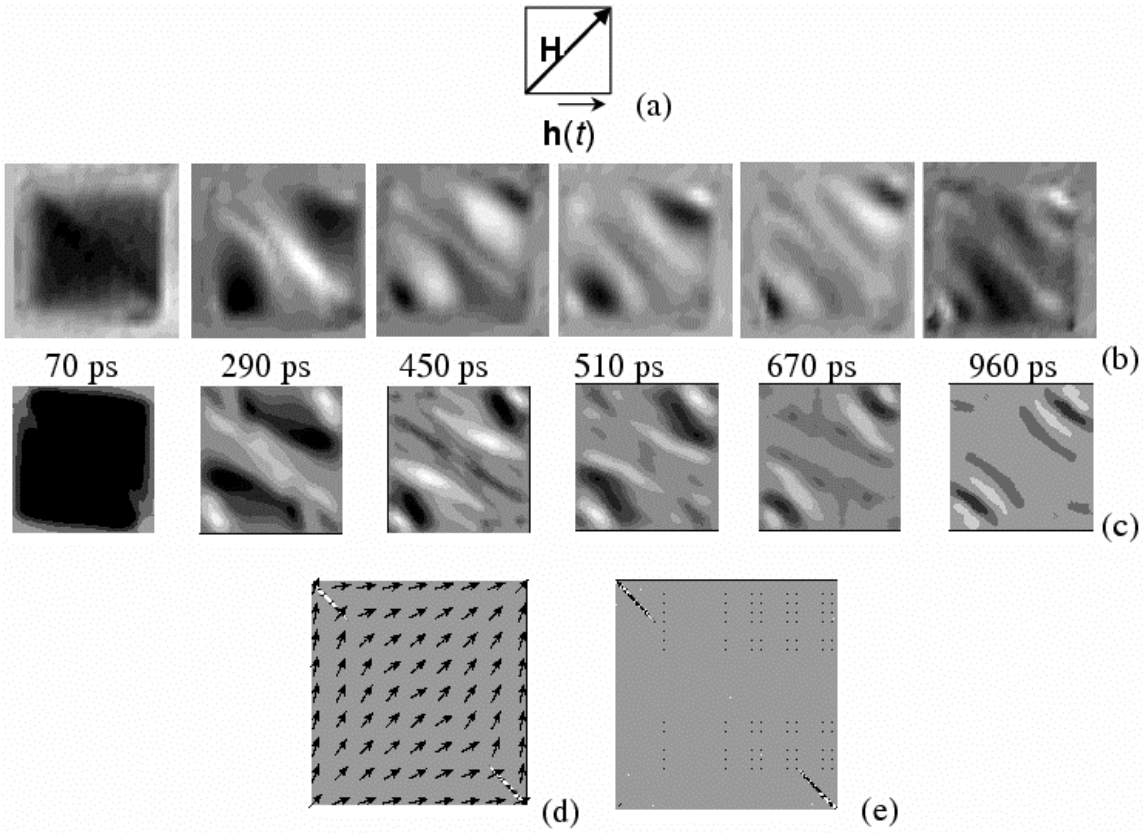

Figure 1.5 A series of TRSKM images of the out of plane component of the magnetisation distribution at different pump-probe time delays (b) are compared with OOMMF micromagnetic simulations (c) for the static and pulsed magnetic fields as shown in (a). The static magnetisation (d) and effective field (e) are also shown (taken from Ref. 33).

edges from where the nonuniformity in the magnetisation then propagates towards the centre of the element. The excitation and subsequent dephasing of spin waves explains the earlier observation of an anisotropic apparent damping of time resolved signals measured in this element[6].

1.2 Interaction of Pulsed Light with Matter

1.2.1 Generalised Reflection Coefficients

When light is incident upon a plane surface, only some part of its intensity is reflected. The reflected intensity I_r may be written as $I_r=I_iR$ (R<1), where I_i and R are the incident light intensity and the sample reflectivity, respectively[63]. The magnitude of R depends upon both the wavelength and polarisation of the incident light and the optical properties of the sample. Phenomenologically, the response of matter to any external electric field can be described by the dielectric tensor $\hat{\varepsilon}$. For an otherwise isotropic medium with magnetisation $\mathbf{M}=M\mathbf{u}$,

$$\hat{\varepsilon} = \varepsilon \begin{pmatrix} 1 & iu_zQ & -iu_yQ \\ -iu_zQ & 1 & iu_xQ \\ iu_yQ & -iu_xQ & 1 \end{pmatrix}, \tag{1.2.1}$$

where ε is the dielectric constant, and Q is the Voigt constant[64],[65].

Using the Jones matrix formalism, one can obtain the reflectivity for light linearly polarised at an angle θ to the plane of incidence

$$R = \left(\left|r_{ss}\right|^2 + \left|r_{ps}\right|^2\right)\sin^2\theta + \left(\left|r_{pp}\right|^2 + \left|r_{sp}\right|^2\right)\cos^2\theta + \frac{1}{2}\left(r_{ss}r_{sp}^{\ *} + r_{pp}r_{ps}^{\ *}\right)\sin^2\theta\,, \tag{1.2.2}$$

where r_{ss}, r_{pp}, r_{sp}, and r_{ps} are the complex Fresnel reflection coefficients for a non-magnetic[63]. For light reflected from the surface of a magnetic sample the reflection coefficients were derived in Ref. 66, 67 to the first order in Q by solving the Maxwell equations at the surface with appropriate boundary conditions

$$r_{ss} = \frac{\hat{n}_0\cos\theta_0 - \hat{n}_1\cos\theta_1}{\hat{n}_0\cos\theta_0 + \hat{n}_1\cos\theta_1}, \tag{1.2.3}$$

$$r_{pp} = \frac{\hat{n}_1\cos\theta_0 - \hat{n}_0\cos\theta_1}{\hat{n}_1\cos\theta_0 + \hat{n}_0\cos\theta_1} + \frac{2iQ\hat{n}_1\hat{n}_0\cos\theta_0\sin\theta_1 u_y}{\left(\hat{n}_1\cos\theta_0 + \hat{n}_0\cos\theta_1\right)^2}, \tag{1.2.4}$$

$$r_{ps} = -\frac{iQ\hat{n}_0\hat{n}_1\cos\theta_0(\sin\theta_1 u_x - \cos\theta_1 u_z)}{\cos\theta_1(\hat{n}_0\cos\theta_0 + \hat{n}_1\cos\theta_1)(\hat{n}_1\cos\theta_0 + \hat{n}_0\cos\theta_1)}, \quad (1.2.5)$$

$$r_{sp} = \frac{iQ\hat{n}_0\hat{n}_1\cos\theta_0(\sin\theta_1 u_x + \cos\theta_1 u_z)}{\cos\theta_1(\hat{n}_0\cos\theta_0 + \hat{n}_1\cos\theta_1)(\hat{n}_1\cos\theta_0 + \hat{n}_0\cos\theta_1)}, \quad (1.2.6)$$

where θ_0 and θ_1 are the angles of incidence and refraction shown in Figure 1.6, and $\hat{n}_0$ and $\hat{n}_1$ ($\hat{n}_i = \sqrt{\varepsilon}$, i=0,1) are the indices of refraction for air and the sample, respectively. For a metal, θ_1 and $\hat{n}_1$ are complex numbers[63]. The Cartesian coordinate system is defined so that the z-axis cants out of the sample perpendicular to its surface, and the x-axis points parallel to the projection of the optical wave vector onto the sample surface, as shown in Figure 1.6.

1.2.2 Magneto-Optical Kerr Effect

According to equations (1.2.3) and (1.2.4), the diagonal reflection coefficients r_{ss} and r_{pp} are generally not equal, and hence, linearly polarised light incident on a non-magnetised metal surface is reflected with elliptical polarisation. Only light polarised parallel (p-polarised) or perpendicular (s-polarised) to the plane of incidence does not change its polarisation. As soon as the metal is magnetised, an incident p- or s-polarised beam is also reflected with modified polarisation. Light that is initially

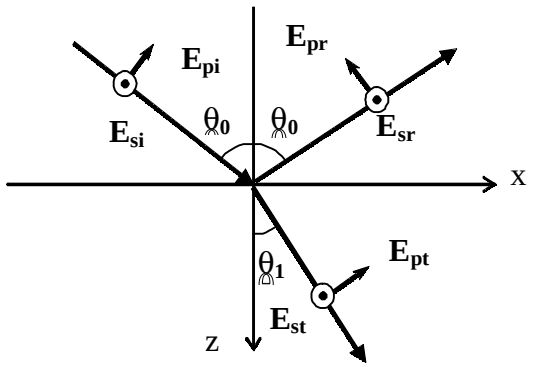

Figure 1.6 Geometry used in the calculation of the generalised reflection coefficients is shown (taken from Ref. 67).

linearly polarised is reflected with elliptical polarisation and the main axis of the ellipse is rotated with respect to the axis of the incident beam. This effect is called the magneto-optical Kerr effect (MOKE)[64,65]. For incident p-polarised light, the rotation of the major axis of the ellipse is given by the Kerr rotation angle

$$\theta_K = -\mathrm{Re}\left\{\frac{r_{sp}}{r_{pp}}\right\}, \tag{1.2.7}$$

and the ellipticity is given by the Kerr ellipticity angle

$$\eta_K = \mathrm{Im}\left\{\frac{r_{sp}}{r_{pp}}\right\}. \tag{1.2.8}$$

Using equations (1.2.4)-(1.2.8), one can distinguish three different MOKE geometries that differ by the direction of the magnetisation relative to the plane of incidence of light. In the polar Kerr effect, the direction of the magnetisation is perpendicular to the sample surface. The effect vanishes for grazing incidence. The polarisation change is larger than in the other two configurations. In the longitudinal Kerr effect, the direction of the magnetisation lies in the plane of the film and in the plane of incidence. The effect vanishes for perpendicular and grazing incidence. In the transverse Kerr effect, the direction of the magnetisation again lies in the plane of the sample but is perpendicular to the plane of incidence. In contrast to the other two effects, the intensity, but not the state of polarisation of p-polarised light is changed. In the first approximation, these effects are linearly proportional to the magnetisation of the sample, and hence this phenomenon is also referred to as the linear MOKE.

1.2.3 Transient Temperature and Two Temperature Model Equations

Formulae (1.2.2)-(1.2.8) have very important consequences. They show that measurements of the intensity and polarisation of the reflected beam can provide information about the electronic state and the magnetisation of the sample. If pulsed laser light is used, this information will correspond to a certain interval of time

determined by the time of arrival and duration of the pulse. Furthermore, a fraction 1-*R* of the incident optical intensity is absorbed in the sample, changing its electron distribution and, hence, also its reflectivity. This brings us to the idea of a pump-probe experiment in which the sample is excited by a pump pulse and the modified reflectivity is measured using a delayed probe pulse.

As shown in Figure 1.7, when an ultrashort pump pulse is absorbed, a so-called non-thermal (also referred to as hot, or non-Fermi) electron population is created[68,69]. The energy injected into the electron subsystem is redistributed among electrons via the electron-electron scattering. A new Fermi distribution, corresponding to the transient electron temperature T_e, is established on femtosecond time scales. This process is referred to as electron thermalisation. Energy is subsequently transferred to the lattice via electron-phonon scattering on picosecond time scales. Both thermal and non-

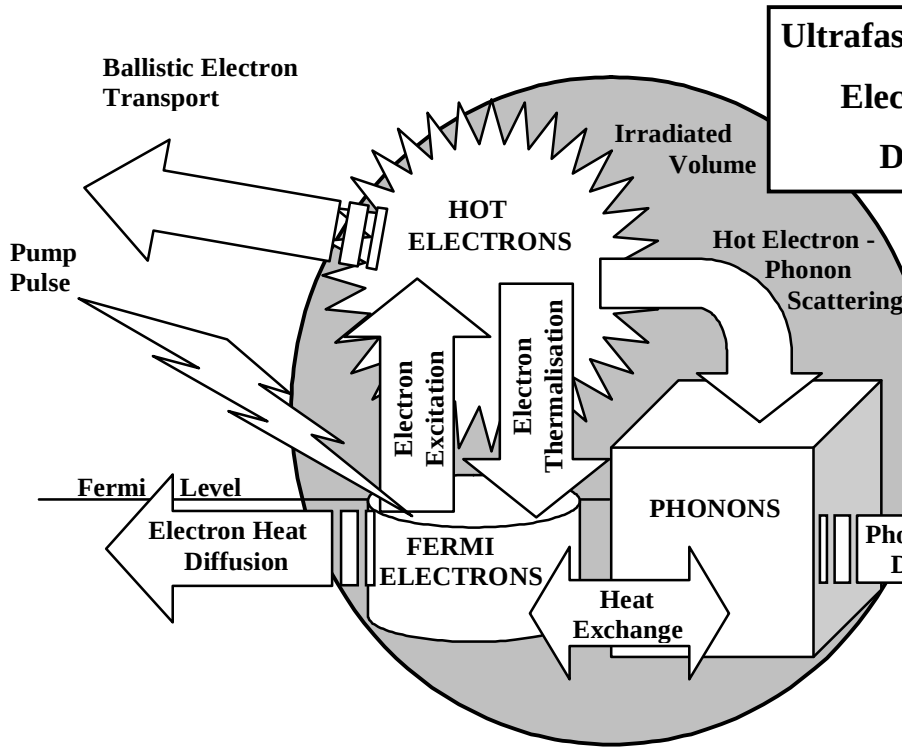

Figure 1.7 Ultrafast electron dynamics in metals are schematically presented.

thermal electrons may participate in the latter process, while the relative importance of the two processes is determined by the phonon spectrum[70]. At each stage, the combined electron-phonon system is continuously cooled by heat transport into the substrate and in the lateral directions [9]. These processes are often modelled using the two temperature model equations[71]

$$C_{\mathrm{e}}\frac{\partial T_{\mathrm{e}}}{\partial t} = -G\left(T_{\mathrm{e}} - T_{\mathrm{l}}\right) + \nabla\left(\kappa_{\mathrm{e}}\nabla T_{\mathrm{e}}\right) + \Xi_{\mathrm{e}}(t,\mathbf{r}), \tag{1.2.9}$$

$$C_{\mathrm{l}}\frac{\partial T_{\mathrm{l}}}{\partial t} = G\left(T_{\mathrm{e}} - T_{\mathrm{l}}\right) + \nabla\left(\kappa_{\mathrm{l}}\nabla T_{\mathrm{l}}\right) + \Xi_{\mathrm{l}}(t,\mathbf{r}). \tag{1.2.10}$$

In these equations, T_{l} is the transient lattice temperature, while C_{l}, κ_{l} and C_{e}, κ_{e} are the heat capacities and conductivities of phonons and electrons, respectively. These parameters are generally temperature dependent, and so the equations are non-linear. The equations are coupled through the term proportional to the difference between the transient temperatures of electrons and phonons, and the electron-phonon coupling constant G. Terms Ξ^{e} and Ξ^{l} describe the process of energy injection into the electron and phonon subsystems, respectively. These are calculated from the kinetic equations for the "hot" state of the system[72].

For the purpose of illustration, Figure 1.8 shows a time resolved reflectivity signal measured from an Al film of 45 nm thickness sputtered onto a Si substrate. The inset shows the same signal at short time delays. The signal was fitted to the analytical formula derived in a later chapter of this thesis. The different stages of the system equilibration can be observed. Stage 1 corresponds to the process of electron thermalisation with a characteristic relaxation time of about 30 fs. Stage 2 corresponds to the heat transfer from the electron subsystem to the lattice with a characteristic time of about 1.9 ps. During this stage a lattice strain develops that then propagates from the heated surface of the film towards the substrate[9]. Although not clear in this example,

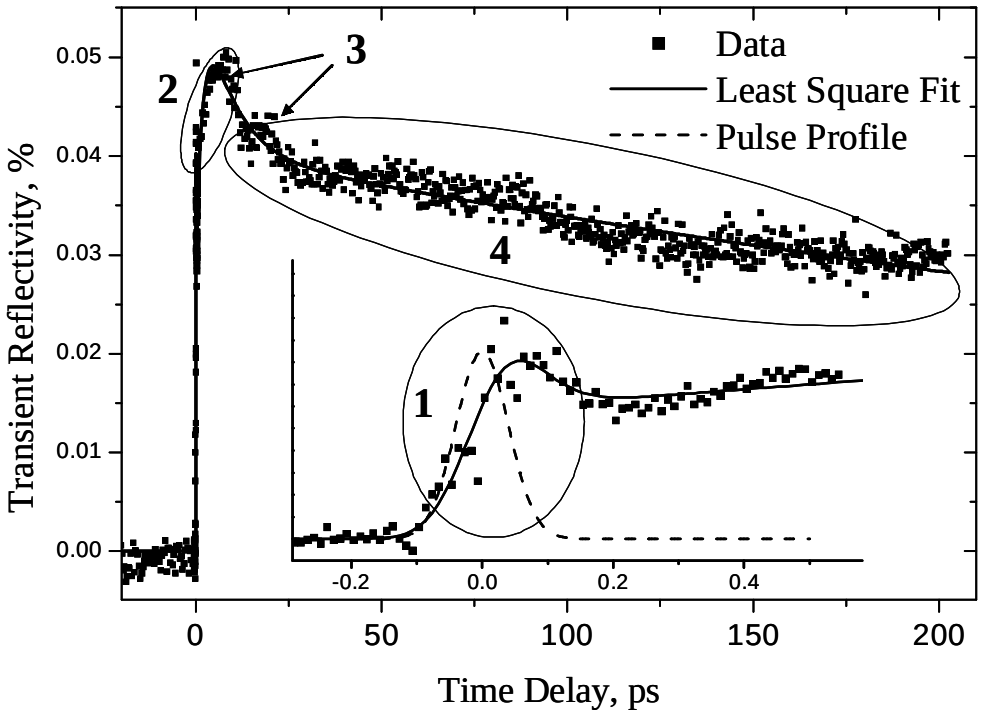

Figure 1.8 The transient change of the reflectivity of an Al thin film excited by a pump pulse is shown as a function of the time delay between the pump and probe pulses. The symbols are data points, and the solid line represents a theoretical fit. The dashed line shows the pump pulse profile.

this is seen as oscillations (3) with frequency of about 90 GHz that arise from reflection of the acoustic wave from the film-substrate interface. This is superposed upon the cooling due to heat transfer to the substrate during stage (4), which takes place on time scales of about 0.5 ns.

In order to interpret the reflectivity signal obtained from the pump-probe experiment, one needs to relate the transient electron temperature to the change in the dielectric tensor. For cubic nonmagnetic crystals where the diagonal components of the dielectric tensor are all equal to the same constant ε and the non-diagonal components are equal to zero, the relation was given in Ref. 4

$$\varepsilon(\omega) = 1 - \frac{\omega_p^2}{\omega\left(\omega + \frac{i}{\tau_c}\right)} - \frac{4\pi e^2 \hbar}{m^2 \omega^2} \times$$
$$\times \sum_{\mathbf{k}\mathbf{k}'bb'} \frac{\left(\omega + \frac{i}{\tau_{bb'}}\right) \langle b\mathbf{k}|p_i|b'\mathbf{k}'\rangle \langle b'\mathbf{k}'|p_i|b\mathbf{k}\rangle}{(E_{b'k'} - E_{bk})\left(E_{b\mathbf{k}} - E_{b'\mathbf{k}'} - \hbar\omega - \frac{i\hbar}{\tau_{bb'}}\right)} [f_0(E_{b'\mathbf{k}'}) - f_0(E_{b\mathbf{k}})], \quad (1.2.11)$$

where ω_p is the plasma frequency, τ_c is the energy dependent relaxation time of the conduction electrons, $\langle b\mathbf{k}|p_i|b'\mathbf{k}'\rangle$ is the matrix element for $b\mathbf{k} \to b'\mathbf{k}'$ transitions, $\tau_{bb'}$ is the corresponding relaxation time, $E_{b\mathbf{k}}$ is the energy of the state $|b\mathbf{k}\rangle$, and

$$f_0(E_{b\mathbf{k}}) = \frac{1}{\exp\left(\frac{E_{b\mathbf{k}} - E_F(T_e)}{k_B T_e}\right) + 1}, \quad (1.2.12)$$

is the Fermi-Dirac distribution function at energy $E_{b\mathbf{k}}$. The Fermi level E_F depends upon the electron temperature T_e as

$$E_F(T_e) = E_{F0}\left(1 - \frac{\pi^2}{12}\left(\frac{k_B T_e}{E_{F0}}\right)^2\right), \quad (1.2.13)$$

where E_{F0} is the Fermi energy at zero temperature, and k_B is the Boltzmann constant. The first two terms and the last term in equation (1.2.11) describe contributions to the dielectric constant due to the intraband and the interband transitions, respectively, which are discussed in the next section and schematically sketched in Figure 1.10.

Figure 1.9 shows the reflectivity change in Au that was calculated in Ref. 4 using equations (1.2.11)-(1.2.13). At low temperature, it vanishes at a photon energy corresponding approximately to optical transitions from the top of the d-band to the s-p-band. This photon energy is also referred to as interband transition threshold. The reflectivity change is negative for photon energies below this threshold, and positive for photon energies above it, becoming negative again, as the photon energy is increased further.

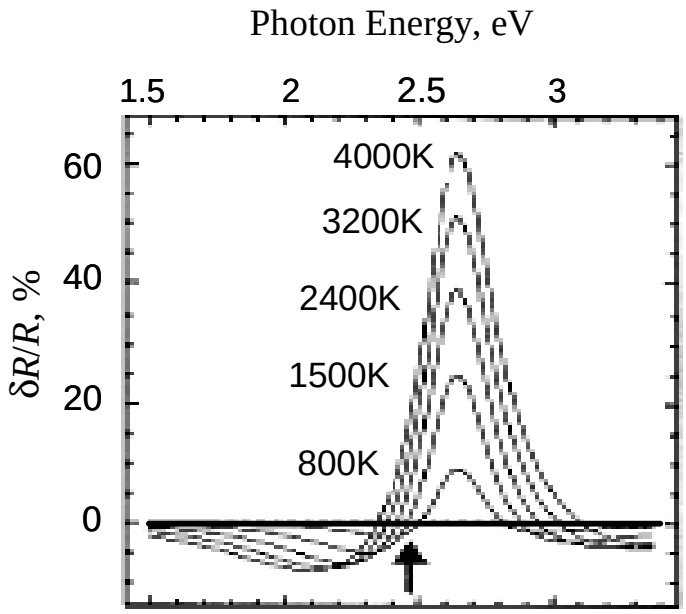

Figure 1.9 The calculated change of Au reflectivity as a function of photon energy is shown for five different temperatures. The reflectivity was normalised to that at room temperature (taken from Ref. 4).

1.2.4 Nonlinear Polarisation. SIFE and SOKE

The interaction between light and matter can be viewed as the creation of a coherent quantum superposition of initial and final electron states that has an associated polarization[3], as shown in Figure 1.10. The coherence between states with different wave vector requires an intermediate virtual state and the presence of a coherent phonon. A transition between the initial and final states may occur when the coherence of the system is broken either due to the finite width of an optical wave packet or by scattering from the environment. The transition results in the absorption of a photon and the creation of a hot electron-hole pair. Otherwise, the photon is re-radiated with a different phase and, perhaps, polarisation.

The time decoherence time T_2^*, which has also been called the dephasing time, is equal to $(1/2T_1+1/T_2)^{-1}$, where T_1 and T_2 are the inelastic (energy) and pure dephasing

(elastic linear or angular momentum) scattering times[3]. Values for T_2^*, T_1 and T_2 have been deduced from TR two-photon photoemission (TR-2PPE), although their physical interpretation is not straightforward[3,73,74]. The induced polarisation may persist for a time T that is greater than T_2^* if the hot electron-hole pair retains some memory of the injected linear and (or) angular momentum after a scattering event.

The pump induced transient polarisation of the medium modifies the polarisation state of a time delayed probe pulse. Phenomenologically, this process can be regarded as a transient pump induced linear or circular birefringence, also called the Specular Optical Kerr Effect (SOKE) and the Specular Inverse Faraday Effect (SIFE)[75]. These are cubic non-linear effects and are predicted to exist from symmetry arguments. Both effects consist of coherent and incoherent parts. For the coherent part, the pump drives the coherent electron-hole pair that affects the probe polarisation. The effect depends upon the probe phase relative to that of the electron-hole pair, and hence, that of the pump. For the incoherent part of the SIFE and the SOKE, the relative pump-probe phase is not important, since the probe pulse polarisation is modified by the pump

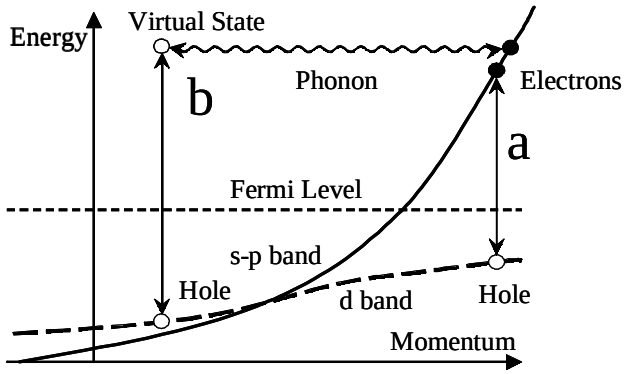

Figure 1.10 Electron-hole coherent state is schematically illustrated for interband (a) and intraband (b) optical transitions.

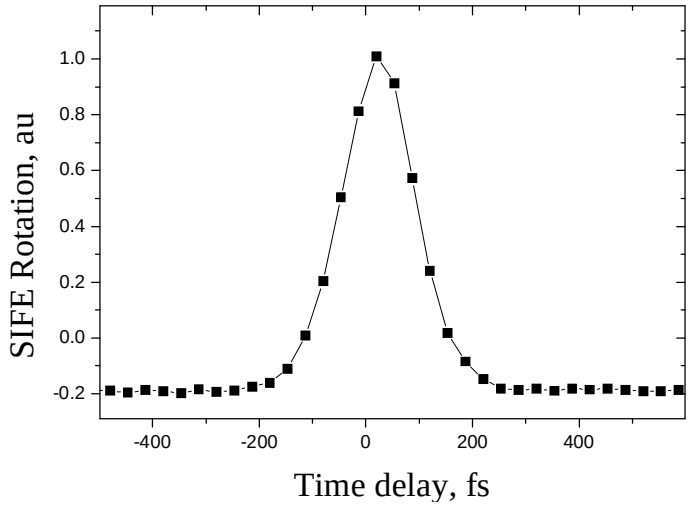

Figure 1.11 The SIFE signal measured from a 63.7 nm thick Pd film sputtered onto a Si substrate is shown for circular pump excitation.

induced sample polarisation that survives after the decoherence of the electron-hole pair. However, it is usually assumed that the time resolved signal, due to either the SIFE or the SOKE, can be described as a pump-probe intensity cross-correlation, since the signal is usually observed to have a sharp peak-like structure, as shown in Figure 1.11.

The magnitudes of the incoherent transient SIFE and SOKE, which are the only effects relevant to the present study, may be related to the cubic components χ_{xxyy} and χ_{xyyx} of the nonlinear susceptibility tensor and the polarisation state of the pump pulse. Let us assume that the pump is initially p-polarised. The pump polarisation can be made elliptical by passing the beam through a quarter wave plate. The pump polarisation depends upon the angle φ between the plane of incidence and the fast axis of the quarter wave plate used to convert the pump pulse to an elliptically polarised state, as shown in Figure 1.12 (c). The pump polarisation can be made linear at some angle to the plane of incidence by passing the beam through a polarizer. Let us denote

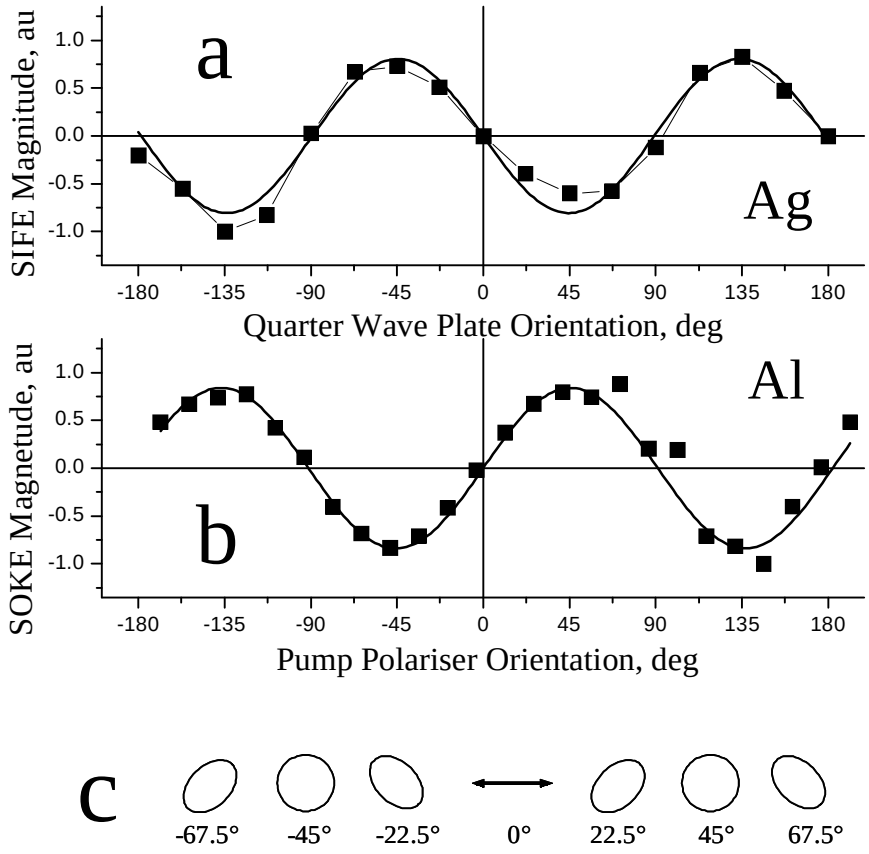

Figure 1.12 (a) The polarisation rotation magnitude due to the SIFE in a 40 nm thick Ag film sputtered onto a Si substrate is shown as a function of the orientation of the pump quarter wave plate, in an experiment with an elliptically polarised pump. (b) The polarisation rotation magnitude due to the SOKE in a 45 nm Al film sputtered onto a Si substrate is shown as function of the orientation of the pump polarizer, in an experiment with a linearly polarised pump. The solid lines are simulations with the sine function of 180 degrees period. (c) The helicity of the pump beam in (a) is schematically presented for different orientations of the pump quarter wave plate.

the angle between the plane of incidence and the transmission axis of the pump polarizer as ψ. Then the magnitude of the signal due to the SIFE and SOKE is given by[76]

$$\begin{pmatrix}\Delta_{\parallel}\\ \Delta_{\perp}\end{pmatrix}=\frac{1}{2}\sin 4\varphi\begin{pmatrix}\mathrm{Re}\\ \mathrm{Im}\end{pmatrix}F_{+}+\sin 2\varphi\begin{pmatrix}-\mathrm{Im}\\ \mathrm{Re}\end{pmatrix}F_{-}, \tag{1.2.14}$$

for an experiment with an elliptically polarised pump, and

$$\begin{pmatrix}\Delta_{\parallel}\\ \Delta_{\perp}\end{pmatrix}=\sin 2\varphi\begin{pmatrix}\mathrm{Re}\\ \mathrm{Im}\end{pmatrix}F_{+}, \tag{1.2.15}$$

for an experiment with a linearly polarised pump. In both formulae, the amplitudes of SIFE (F_{-}) and SOKE (F_{+}) are given by

$$F_{\pm}=-\frac{32\pi^{2}I_{pump}}{c\left|1+\hat{n}\right|^{2}}\left\{\frac{\chi_{xxyy}\pm\chi_{xyyx}}{\hat{n}(1-\hat{n}^{2})}\right\}, \tag{1.2.16}$$

where I_{pump} is the pump beam intensity, $\hat{n}$ is the complex refraction index, and c is the speed of light. These formulae were derived in the continuous wave approximation for normal incidence of the pump and probe beams.

As shown in Figure 1.12 (a), the SIFE has a maximum magnitude for circular pump polarisation (for φ=±45°), and vanishes when the pump is linearly polarised (for φ=0,±90°). The SOKE increases as the ellipticity angle of the pump approaches 0° or 90°, and as the angle between the major axis of the pump beam ellipse and the plane of probe polarisation approaches 45° (for φ=0,±22.5°,±67.5°). This is seen in Figure 1.12 (a) as a weak deviation of the data points from the simulated curve, which has a period that is characteristic of the SIFE. The SOKE vanishes when the pump is either circularly polarised (e.g. for φ=±45°), or linearly polarised with the plane of polarisation either parallel or perpendicular to that of the probe (e.g. for φ=0°). As shown in Figure 1.12 (b), in measurements with linearly polarised pump, the SOKE has a maximum magnitude when the plane of the pump polarisation is at 45° to that of the probe, and vanishes when the pump is either parallel or perpendicular to it (for ψ=0°,±90°±180°).

1.3 Summary

In summary, the general background of my research in Exeter was briefly introduced in this chapter, and will be referred to again in the following original chapters. On this basis, a theoretical model, either analytical or numerical, will be developed to describe each set of my experimental data.

Chapter 2. Technique of Pump-Probe Experiments

In this chapter, the experimental apparatus used in my project will be described. The experimental facilities for time resolved measurements in Exeter had been built up by Dr. R.J. Hicken, Dr. J. Wu[77] and Dr. R. Wilks[76] before I started my PhD project. Dr. A. Barman constructed the time-resolved Kerr microscope. Hence, in this chapter only a brief description of the experimental setup will be given. Instead, a greater emphasis is placed on the development of the measurement technique, understanding of the measured signals, and separating the signal response from measurement artefacts. Some data will be presented for the purpose of illustration. The pump-probe apparatus used in the two colour measurements at the Rutherford Appleton Laboratory was constructed by Dr. P. Matousek and Dr. M. Towrie.

2.1 Single Colour Optical Pumping Apparatus

The apparatus used for optical pumping experiments in Exeter is shown in Figure 2.1 (a). The pulsed light source used to make most of the measurements presented in this thesis, was a 80 MHz mode-locked Ti: sapphire laser (Spectra-Physics Tsunami) pumped by a continuous wave (cw) diode laser (Spectra-Physics Millennia), that produced sub 90 fs pulses at photon energy of $\hbar\omega$=1.575±0.005 eV (787 nm), unless stated otherwise. The apertures (1) were used to reset the beam direction after any drift in the laser alignment.

The beam was passed through a pulse picker (2), which was not used in the measurements reported here. In order to compensate pulse broadening (“chirp”)

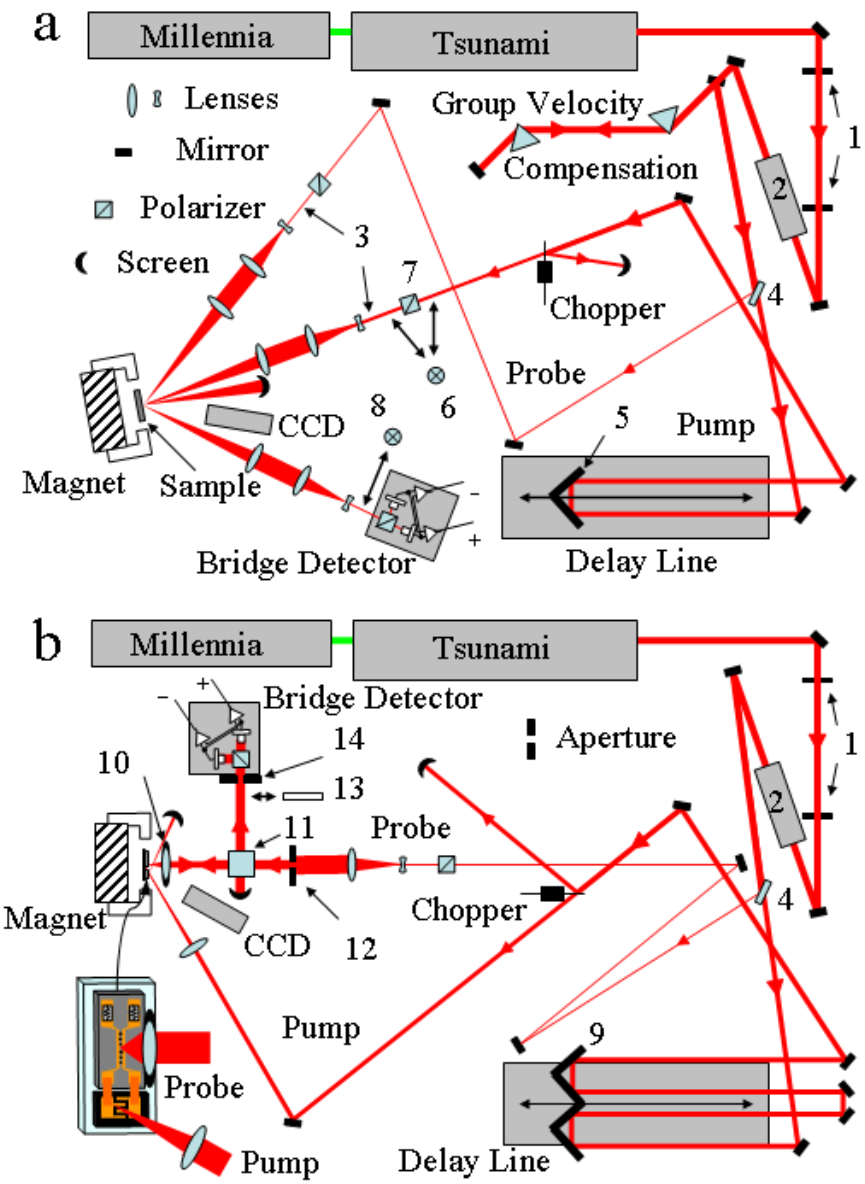

Figure 2.1 The apparatus used in the single colour optical pumping (a) and field pumping (b) experiments is shown in schematic form, as described in the text.

introduced by the pulse picker and pre-compensate that caused by other "bulky" optics (lenses, polarizers etc.), the beam was passed through a group velocity dispersion compensation line, consisting of a pair of Brewster prisms and a mirror[76]. The temporal width of the pump and probe pulses was checked with a fringe-resolved autocorrelator,

built by Dr. R. Wilks, placed at various places in the beam path[76]. The pulse width measured just before the expansion optics (3) was found to be in agreement with that measured just after the laser and with that deduced from bandwidth measurements using a laser spectrum analyzer. Measurements were not made at the sample position, since the beam would first need to be re-collimated. This would require the insertion of additional optics that could introduce additional chirp.

Each pulse was split with a beam splitter (4) into pump and probe parts with energies of E_{pump} and E_{probe} with (E_{pump}>E_{probe}). A variable optical delay line in the pump path allowed the time delay between the two pulses to be varied with a minimum step size of 1.67 fs. The position of a hollow retro-reflecting prism (5) in the delay line was varied through a few wavelengths at high frequency in order to remove any coherence oscillations around the zero delay position. The maximum time delay was 2 ns.

The probe was always polarised in the plane of incidence (p-polarised). The polarisation of the pump could be varied continuously from a p-polarised state either to a circularly polarised state by rotating a quarter wave plate (6) placed after a polarizer (7), or to a state in which the beam was linearly polarized at an angle to the plane of incidence. In the latter case a quarter wave plate (6) was placed in front of the polarizer (7) in order to make the beam circularly polarised and, hence, to maintain constant intensity at the sample surface. Both pump and probe beams were expanded by a factor of ten in order to reduce the beam divergence, and focused down to 15 μm diameter spots at the sample surface, using achromatic doublets with focal length of 16 cm. The spots were carefully overlapped while being viewed with a CCD camera with x600 on-screen magnification.

The pump was modulated at a frequency of 2 kHz by a mechanical chopper. Any transient changes in the intensity and polarisation state of the reflected probe could be

simultaneously sensed by an optical bridge detector[77] with its sum (intensity) and difference (polarisation) outputs connected to two lock-in amplifiers. The phase sensitive detection allowed changes in rotation and ellipticity angles of down to 1 μdeg to be resolved. In experiments in which the transient ellipticity was measured, a quarter wave plate (8) was placed in front of the bridge detector with its fast axis parallel to the plane of incidence. When necessary, an electromagnet capable of producing a magnetic field of up to 3 kOe was used to magnetise the sample.

2.2 Field Pumping Apparatus

The field pumping experimental configuration shown in Figure 2.1 (b) was similar to that used for optical pumping. However, there were also some important differences. First of all, less care was taken over the laser pulse width because the width of the magnetic field pulse was determined mainly by carrier relaxation in the photoconductive switch and dispersion in the structure used for the generation and delivery of the pulsed field to the sample[77]. On the other hand, values of the pump and probe pulse energies were important for obtaining a good signal to noise ratio. Therefore, the group velocity compensation line was not always used, and the light pulses had width of up to about 180 fs.

The magnetisation dynamics were typically observed to occur on time scales of tens of picoseconds. On the other hand, the total length of time scans was important for the acquisition of good quality Fourier spectra. Therefore, in the later measurements an additional hollow retro-reflecting prism (9) was introduced into the delay line that increased both the maximum time delay and the minimum step size by a factor of two. The position of the hollow retro-reflecting prism in the delay line was not modulated.

In experiments on continuous samples, for which the longitudinal MOKE geometry was used, the configuration of the probe focusing optics was the same as in the optical pumping configuration, yielding a 15 μm spot size. Better spatial resolution was required for measurement of micron sized elements. The time resolved scanning Kerr microscope was constructed for this purpose[a] in which a microscope objective with numerical aperture of 0.65 corrected for a 0.17 mm thick cover slip (10) was used to focus the expanded probe beam to a spot of sub-800 nm diameter at normal incidence. One half of the probe beam was reflected away from the sample by the beam splitter

cube (11), while the other half was transmitted towards the sample. After being reflected from the latter, half of the probe was directed towards the bridge detector with the same beam splitter, while the residual beam was transmitted and blocked by the aperture (12). The sample and the structure used to generate the pulsed field were mounted on a computer operated piezoelectric scanning stage. The stage had a travel range of 100 μm and 20 μm in the directions parallel and perpendicular to the sample surface, respectively. While the perpendicular degree of freedom was used for a fine adjustment of the probe focusing, lateral scanning of the sample under the fixed probe spot allowed intensity and Kerr rotation images of the sample to be acquired for a fixed time delay between the pump and the probe. Although the second configuration obviously provided better spatial resolution, the first approach had some advantages since the angle of incidence of the probe was well defined, and so the MOKE response could be more easily related to the instantaneous orientation of the magnetisation vector. The full beam from the microscope objective was used so that there was no net contribution from the longitudinal Kerr effect and only the out of plane component of the magnetisation was sensed by means of the polar Kerr effect.

The pump beam was always focused on the photoconductive switch with a single lens without prior expansion, since a spot of larger size (normally greater than 100 μm) that spanned many fingers of the switch was preferred. This ensured that the magnitude of the field pulse was unchanged when the piezoelectric stage was used to scan the entire sample structure relative to the fixed pump and probe beams.

The CCD camera was used to monitor the position of pump spot on the photoconductive switch and for rough positioning of the probe. The microscope itself was used for assessing the focusing and positioning of the probe on the surface of small sample elements. A screen (13) was inserted in front of the bridge detector for this

[a] The time resolved scanning Kerr microscope was constructed by Dr. A. Barman.

purpose. When the probe beam was defocused, an image of the sample was formed on the screen. As the probe was focused, the image transformed into a featureless circular spot, since the focused probe spot size was smaller than that of the element. An aperture (14) was used to block any stray light scattered towards the bridge detector.

The different structures used for the generation and delivery of the pulsed magnetic field to the sample are shown in schematic form in Figure 2.2. An interdigitated photoconductive switch, formed by deposition of Au onto a semi insulating GaAs substrate, was gated by the pump pulse. Since the laser photon energy exceeded that of interband transition threshold in GaAs, absorption of the pump pulse reduced the resistance of the switch by about two orders of magnitude. The switch was connected by copper contacts to either a coplanar strip transmission line (CPS) as shown in Figure 2.2 (a), (c), (d), or a coplanar waveguide (CPW) as shown in Figure 2.2 (b), which were made of Au or Al deposited onto a Si or glass substrate. The circuit was biased by a dc voltage of about 20 V that caused a current pulse to propagate from the switch and along the structure before being absorbed in the terminating 47 Ω surface mount resistors. The magnetic field associated with the current pulse was used to stimulate the sample.

The width of the transmission line tracks was typically reduced to less than 100 μm so that pulsed fields greater than 1 Oe could be generated. The amplitude of the pulsed field could be calculated from the amplitude of the current pulse which could be estimated by monitoring the voltage drop across one of the terminating resistors with a 500 MHz oscilloscope. The pulsed field profile at the sample position could be determined by an electro-optic sampling measurement[78] in which a 0.5 mm thick $LiNbO_3$ crystal was also overlaid on the CPS or CPW, although this might modify the pulse profile. The rise and decay times of the current were typically about 40 ps and 2 ns, respectively.

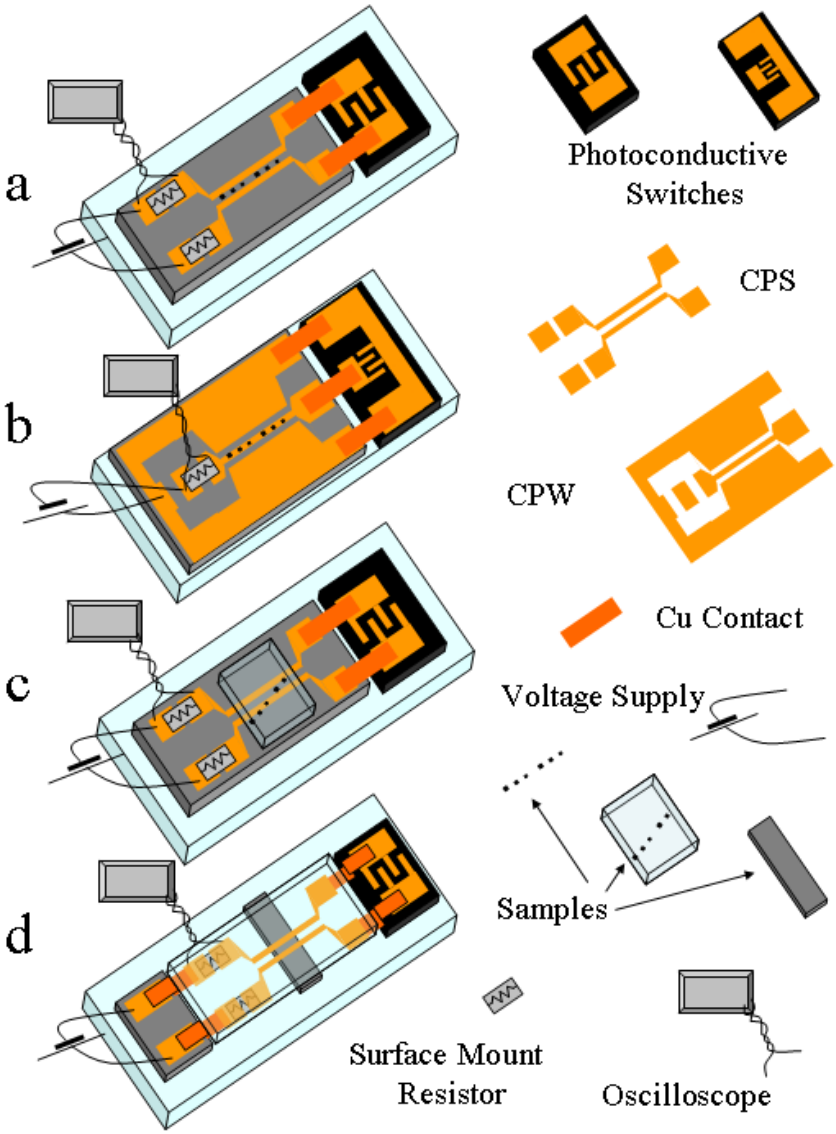

Figure 2.2 The design of the different types of structure used to generate the pulsed magnetic field are presented:

(a) the coplanar transmission line structure with micron sized samples deposited in between the tracks;

(b) the coplanar wave guide structure with micron sized samples deposited on top of the central conductor;

(c) the coplanar transmission line structure with micron sized samples on a glass substrate overlaid onto the structure;

(d) the coplanar transmission line structure on a glass substrate with a continuous film sample on an opaque substrate placed underneath the structure.

From an experimental point of view, the best way of placing the samples is to define them directly on the CPS or CPW structure as shown in Figure 2.2 (a) and (b). This allows direct optical access to the samples and provides a magnetic field pulse of maximum magnitude since there is almost no gap between the sample and the current carrying structure. While the former feature is advantageous for the scanning Kerr microscope investigations, the latter is essential if large amplitude magnetisation dynamics are to be excited. The main drawback of this configuration is the sample fabrication is more complicated. However, since the structural and magnetic properties of thin films can depend strongly upon the substrate, the properties of such samples may generally differ from those of materials used in real devices.

In another configuration, shown in Figure 2.2 (c), the samples grown on transparent substrates were placed face down onto the CPS so as to be subject to the pulsed magnetic field, while being probed through the transparent substrate. While providing good optical access to the samples, the magnitude of the magnetic field pulse depended on the separation between the sample and the CPS, which was difficult to control. As in the previous case, this configuration also requires a special substrate.

In order to make measurements on samples grown on opaque substrate, structures shown in Figure 2.2 (d) were used. These were made by fabricating the transmission line on a transparent substrate so that the measurements could be made by probing through the transmission line substrate. The main difficulty lay in adjusting the separation between the sample and the CPS so as to obtain a significantly large pulsed magnetic field, while preventing the sample from shorting the CPS. Overlayers of transparent insulating material could easily be applied to the transmission line to avoid the latter problem if necessary. The type of structure was chosen to suit the particular experiment.

2.3 Two Colour Optical Pumping Apparatus

The apparatus used for the two-colour pump-probe measurements at the Rutherford Appleton Laboratory is shown in Figure 2.3. The output of a Ti:sapphire regenerative amplifier producing 200 fs pulses at a repetition rate of 1 kHz and wavelength of 800 nm was used. In the reflectivity measurement geometry shown in Figure 2.3 (a), the beam was split to generate pump and probe parts. The 400 nm pump pulse (1), generated by frequency doubling of the fundamental, had energy of 2 μJ. The other part of the fundamental (2) was used to generate a white light continuum in a 1 cm water cell. Both beams were p-polarized and focused onto the sample surface so as to give 200 μm and 400 μm diameter spots, for the probe and pump respectively. The spots were carefully overlapped, while being viewed with a CCD camera. The angles of incidence of the pump and probe beams at the sample were 35° and 30°, respectively. The pump beam was passed through a delay line and reflected from an opto-galvanic mirror placed just before the sample. The mirror was flipped between two positions at a frequency of 2 kHz so that every other pump pulse was deviated from the sample and blocked (3). The white light probe beam was reflected from the sample and dispersed by a grating so that the different spectral components could be detected separately by a linear array detector. A 400 nm filter was placed in front of the detector in order to suppress stray light contributions from the pump beam. An 800 nm filter was placed just behind the water cell in order to suppress contributions from the original probe beam. Signals with pump on and off were subtracted, normalized, and averaged over a time interval of 10 s. The water cell introduced a chirp within the probe pulse so that red light was delayed by about 2 ps with respect to the blue. The signal at different time delays was acquired in a random order so as to remove any slowly varying background.

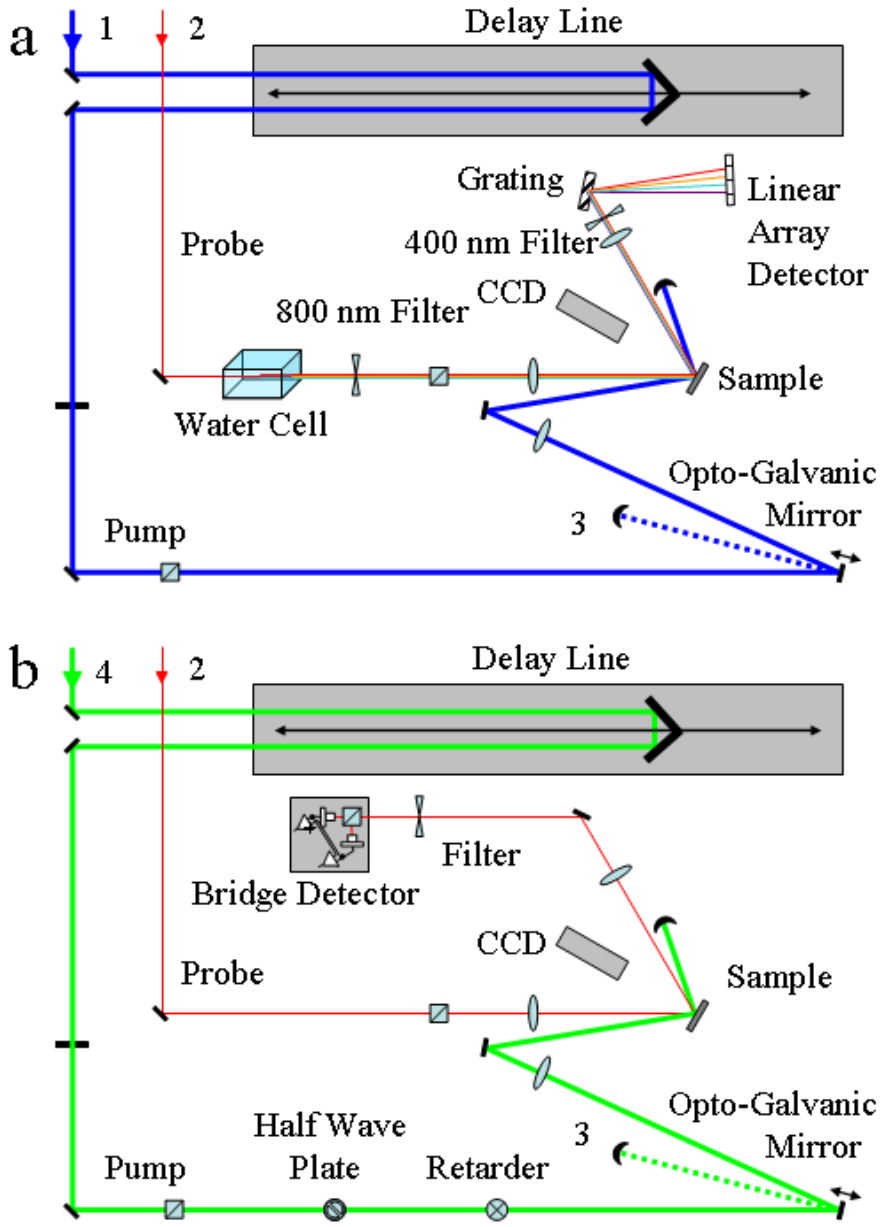

Figure 2.3 The apparatus used in the two colour optical pumping experiments is shown for the measurements of the transient reflectivity (a) and polarisation (b).

This detection scheme provided inadequate signal-to-noise ratio for measurements of the transient polarisation. Hence, the configuration shown in Figure 2.3 (b) was used. The output (4) of an optical parametric amplifier (OPA) at a wavelength close to an interband transition in the metallic sample under investigation was used as the pump.

The fundamental output of the Ti:sapphire regenerative amplifier at 800 nm was used as the probe. The latter was p-polarized while a variable retarder in combination with a half wave plate was inserted into the pump beam path in order to make the pump beam circularly polarized. The polarisation could be switched between right and left helicity by rotating the half wave plate by 45 degrees. The reflected probe beam was directed into an optical bridge detector that produced an output signal proportional to the angle of rotation of the probe polarization. The signal was then fed into a lock-in amplifier, with the drive signal to the opto-galvanic mirror serving as the reference input. The detector was nulled while its output was viewed using an oscilloscope. A filter at the pump wavelength was placed in front of the detector so as to block any scattered pump light.

2.4 Artefacts in Pump-Probe Measurements

2.4.1 Coherent Suppression of Magnetisation Precession

In the field pumping measurements, the temporal profile of the pulsed field is the main source of artefacts. The bandwidth of the oscilloscope used to monitor the pulse field was insufficient to resolve fine features of the pulse shape. The pulse profile was instead determined by the electro-optic sampling technique in which a $LiNbO_3$ crystal of 0.5 mm thickness was placed on top of the CPS structure. The stray electric field from the transmission line induces a transient birefringence that modifies the probe polarisation. Figure 2.4 (a) and Figure 2.4 (b) show the time resolved electro-optic signal[a] obtained when the probe beam was focused through the $LiNbO_3$ crystal, at normal incidence, at points on and between the tracks of a transmission line structure, respectively. One can see that the secondary peaks appear on longer time scales. The peaks are due to reflections of the current pulse from the transmission line interconnects, and lead to the structured Fourier spectra, shown in panels (c) and (d) of Figure 2.4, that were obtained from the signals shown in panels (a) and (d), respectively.

The pulsed magnetic field profile shown in Figure 2.4 suggests that a coherent interaction between the oscillatory signal and the pulsed field[79,80] may appear in the measured sample response. Indeed, upon arrival of a secondary peak of the pulse profile the amplitude of a signal may be either amplified or reduced. Then, if the duration of the signal is small, this may be reminiscent of beating. The Fourier spectrum of the signal may contain a peak at a frequency close to that seen within the spectrum of the pulsed field, e.g. about 2 GHz. The character of such a beating will

[a] The time resolved signals in Figure 2.4 (a) and Figure 2.4 (b) were measured by Dr. A. Barman.

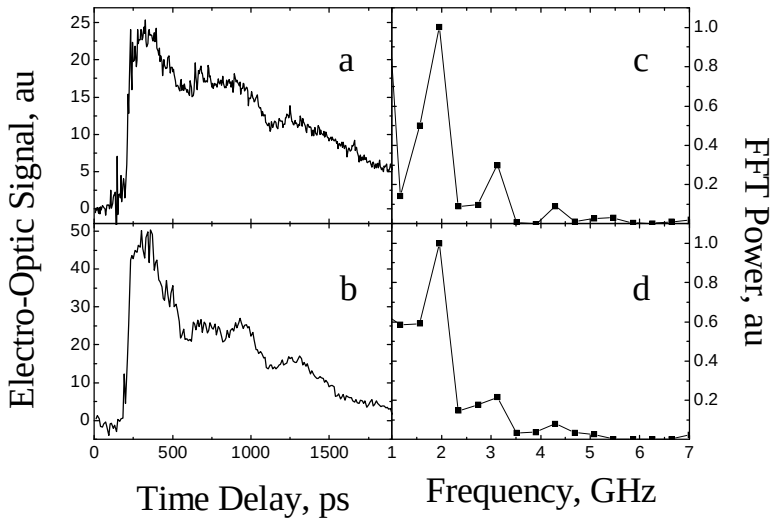

Figure 2.4 The time resolved electro-optic signal obtained from the $LiNbO_3$ crystal is shown for points (a) on and (b) between the tracks of a transmission line structure. The Fourier spectra obtained from the signals shown in panels (a) and (d) are presented in panels (c) and (d), respectively.

depend upon the magnitude of the static bias field, since the effect depends upon the relative phase of the secondary peaks in the field profile and the oscillatory signal. Finally, this effect may also be spatially non-uniform, since the strength and orientation of the pulsed field varies in the direction perpendicular to the tracks of the CPS (CPW). All this makes the analysis of the magnetic Fourier spectra very complicated, especially if multiple modes are expected to be present in the signal.

2.4.2 Reflectivity Breakthrough to Transient Polarisation Signal

In the optical pumping measurements of transient polarisation, care should be taken to properly align the bridge detector and the probe polarisation, since misalignment of either can lead to additional contributions to the measured rotation or ellipticity signal[76]. These contributions, called "reflectivity breakthrough", originate from pump induced changes of the generalised reflection coefficients r_{ss} and r_{pp} and their difference, and are roughly proportional to the transient reflectivity. They may

usually be removed from the transient rotation signal by gradually changing the probe polarisation as illustrated in Figure 2.5. The pump polarisation must be kept linear and parallel to that of the probe so as to remove any residual contributions from the SIFE or SOKE. The bridge detector must be readjusted after the polarisation of the probe is changed so that its static output is zero[76].

In principle, if the experiment is aligned so that there is no reflectivity breakthrough in the rotation signal, then there is no reason to expect it to be present in the ellipticity signal. However, it was sometimes found that a tiny step-like offset occurred in the ellipticity while the rotation remained flat. We believe that this contribution to the ellipticity side originates from an incomplete removal of the reflectivity breakthrough in the rotation, which becomes amplified when the ellipticity is larger than the rotation. It was not possible to tune the probe polarisation in the manner described previously because of the presence of the additional quarter wave

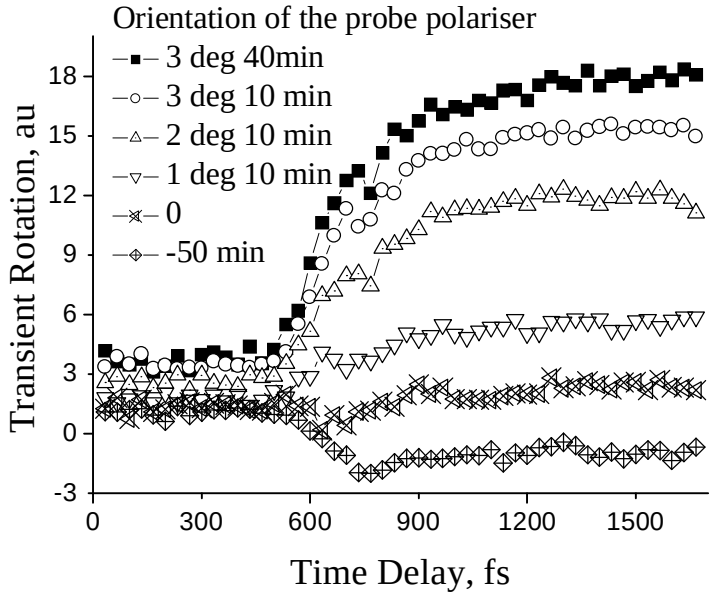

Figure 2.5 The transient rotation signal measured from a 63.7 nm Pd film sputtered onto a Si substrate is shown for different orientations of the probe polarizer. The "zero" orientation corresponds to a correct alignment.

plate in front of the bridge detector during the ellipticity measurements. Therefore, a small reflectivity breakthrough may be seen in some of the transient polarisation signals. However, this decays with a very long relaxation time that is characteristic of the transient reflectivity, and so cannot be confused with the femtosecond timescale response due to the SOKE or the SIFE.

2.4.3 Ni film. Ultrafast Demagnetisation

In the optical pumping measurements, the transient polarisation response of magnetic samples contains an additional contribution due to the ultrafast demagnetisation phenomenon[10,81]. However, this may be removed by magnetising the sample perpendicular to the plane of the probe incidence. This corresponds to the transverse MOKE configuration, and hence the sample demagnetisation contributes to the reflectivity but not to the polarisation response[82].

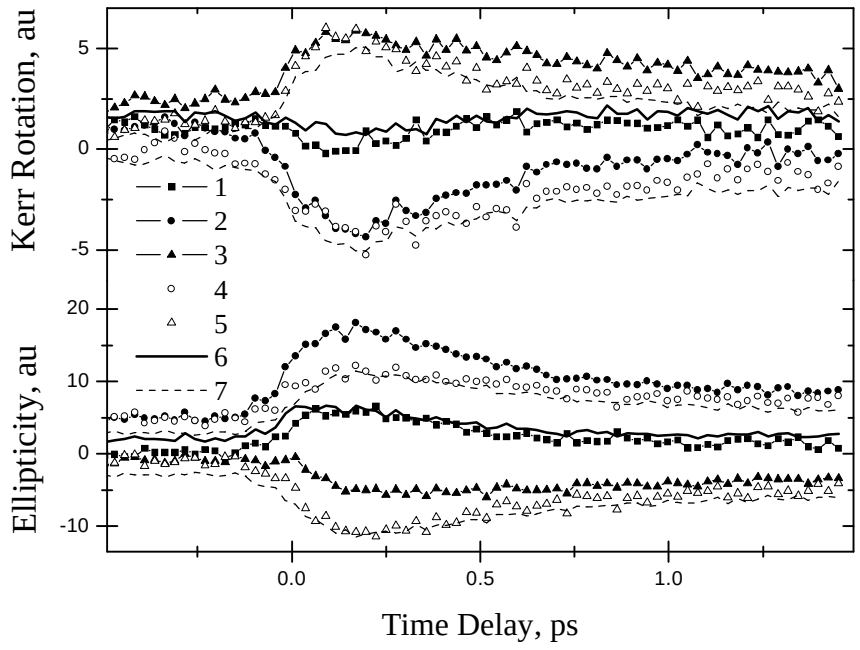

Figure 2.6 The transient polarisation response of a 53.6 nm Ni film sputtered onto a Si substrate is shown for different magnetic states of the sample, as explained in the text.

In Figure 2.6, the transient polarisation response of a 53.6 nm Ni film sputtered onto a Si substrate is shown for different magnetic states of the sample. Curve 1 corresponds to the optimum alignment of the probe polarisation, when the sample magnetisation was saturated perpendicular to the plane of incidence of the probe (the transverse MOKE configuration). Curves 2 and 3 correspond to the same probe polarisation but the sample magnetisation was saturated in opposite directions within the plane of incidence (the longitudinal MOKE configuration). One can see that although curve 1 is almost straight in rotation, it is more curved in ellipticity. This implies that the alignment of the probe polarisation was not perfect in the former case, i.e. just the situation described in the previous subsection. As a consequence of this, the longitudinal curves 2 and 3 in rotation are more symmetric with respect to the flip of the magnetisation direction than those in ellipticity. By subtracting the transverse signal (curve 1) from the longitudinal signal (curves 2 and 3), the demagnetisation signal becomes symmetric both in rotation and ellipticity (curves 4 and 5). It also becomes similar to the difference divided by 2 of the longitudinal signals acquired for opposite directions of the magnetisation (curves 7)[83], while the average of the latter signals (curve 6) has a similar temporal shape to that of the transverse signal (curve 1).

While this is of general interest for the discussion of the relative importance of different magnetic and nonmagnetic contributions to the experimentally observed ultrafast demagnetisation signal[10,68,81-83], in this thesis we will simply exploit the fact that the magnetic contribution to the polarisation signal is suppressed in the transverse MOKE configuration. This then allows us to remove the contribution from the reflectivity breakthrough, as shown in Figure 2.7. One can also see that the contribution has a temporal shape very similar to that of the reflectivity signal.

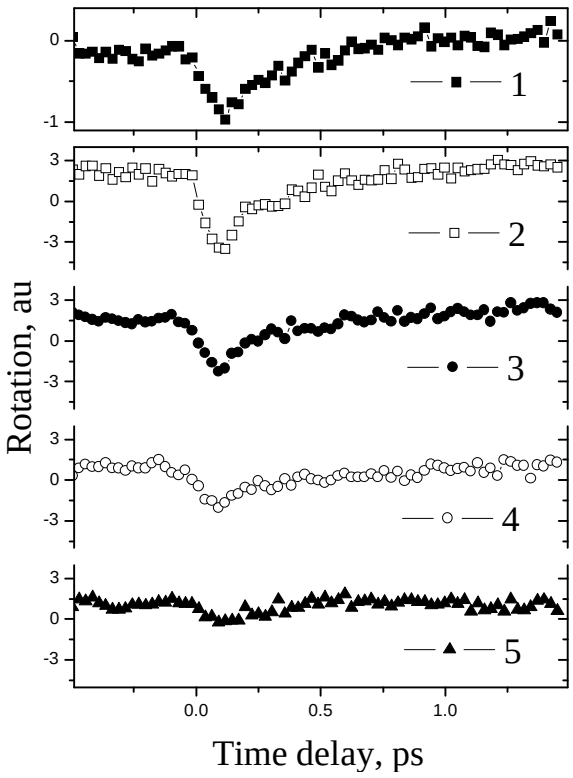

Figure 2.7 The temporal shape of the transient reflectivity signal (1) from a 53.6 nm Ni film sputtered onto a Si substrate is compared to its transient rotation response in the transverse MOKE configuration for different orientations of the probe polarisation relative to the probe plane of incidence: (2) – 1.5 deg, (3) – 1 deg, (4) – 0.5 deg, and (5) – 0 deg.

2.4.4 Effect of Quarter Wave Plate Rotation

In the optical pumping measurements, it was found that the rotation of the pump quarter wave plate affects not only the height of the signal due to the SIFE and SOKE, but also the background of the polarisation signal and the reflectivity signal. Figure 2.8 presents the dependence of the Pd rotation and reflectivity signals and background levels upon the quarter wave plate orientation. The rotation peak magnitude curve has "figure of eight" shape that is characteristic of the SIFE dependence upon the quarter wave plate orientation with a period of 180°, as described by equation (1.2.14). The

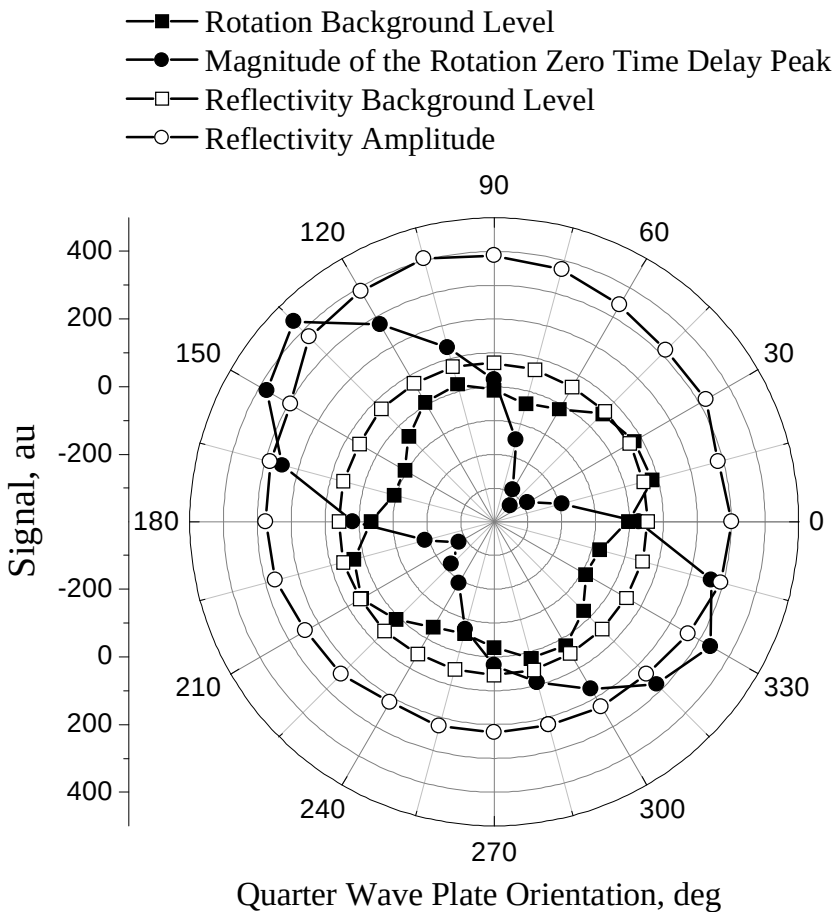

Figure 2.8 The dependence of the rotation and reflectivity signals and background levels at negative time delay upon the quarter wave plate orientation is shown for a 63.7 nm Pd film sputtered onto a Si substrate.

curve is somewhat asymmetric with respect to its long axis (135° - 315°). This is due to the SOKE, which makes a contribution to the signal of smaller magnitude in this case. However, the magnitudes of the signal are also not equal at the opposite poles of the axis. While this asymmetry might be also due to some random noise, one can see that it is correlated with that in the magnitude of the reflectivity. The latter varies by about 20% with a period of 360° with respect to the quarter wave plate rotation. This may be due to a small displacement of the pump spot that changes the overlap of the pump and probe spots.

While the reflectivity background level follows the same dependence as the reflectivity signal, the rotation background has a four fold symmetry that is qualitatively different from the main signal. However, this allows us to identify the origin of the background as the stray pump light scattered from the sample towards the bridge detector. Inside the latter, the beam is split into components that are polarised parallel and perpendicular to the axis of the detector that is rotated at 45° away from the probe plane of polarisation if the detector is properly aligned[77]. The detector difference output is proportional to the difference of the intensities of the two components. The difference signal due to the stray pump vanishes when it is either circularly polarised, or linearly polarised parallel or perpendicular to the probe polarisation, and hence at 45° to the axis of the bridge detector. However, elliptically polarised stray pump light induces a finite difference signal with a magnitude varying with a period of 90° with respect to the orientation of the pump quarter wave plate.

In summary, the measurement of the signal dependence upon the pump quarter wave plate orientation provides a means of separating the signal from artefacts.

2.4.5 Zero Time Delay Position

The optical pumping results reported in chapter 5 rely on an accurate determination of the zero time delay position in the transient polarisation measurements. Since the orientation of the quarter wave plate was found to affect the overlap of the pump and probe, it was also important to determine its influence upon the zero time delay position. Figure 2.9 presents transient reflectivity signals that were recorded simultaneously with the transient polarisation response in two series of measurements. Panel (a) shows reflectivity signals recorded when the transient rotation was measured as function of the pump quarter wave plate orientation. The signals were recorded in random order, but are arranged in the panel in order corresponding to the orientation of

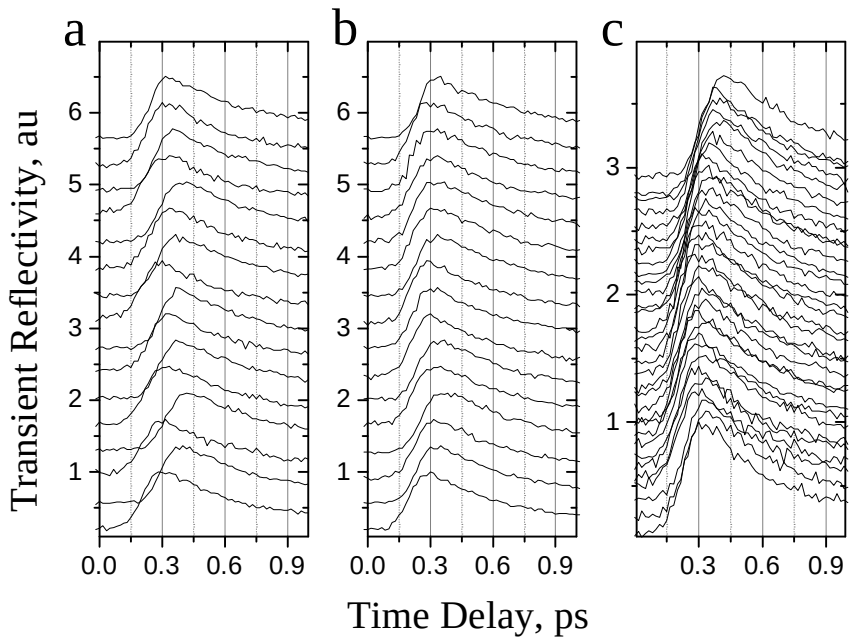

Figure 2.9 Transient reflectivity signals measured from a 32.6 nm Cu film sputtered onto a Si substrate are presented. Panels (a) and (b) show reflectivity signals measured simultaneously with transient rotation and ellipticity, respectively, in order corresponding to the orientation of the quarter wave plate. The latter varies from 78.75° for the bottom trace to -90° for the top trace. Panel (c) shows the signals from panels (a) and (b) in the order that they were actually measured. The peak signal magnitude was normalised to unity in each case.

the quarter wave plate. The bottom and top signals correspond to angles of 78.75° and -90° between the fast axis of the quarter wave plate and the plane of incidence, while the signals in between are equally spaced within this range. One can see that the signal onsets do not show any regular dependence upon the orientation of the quarter wave plate. Panel (b) shows transient reflectivity for the same orientations of the pump quarter wave plate but in a different series of experiments in which the transient ellipticity was measured. The experimental configuration in this case was different to that used for the rotation measurement only in that a quarter wave plate was placed in

front of the bridge detector, and so the optical paths of the pump and probe before the sample were not altered. However, the onsets of the reflectivity signals in the two series of measurements are not correlated. Panel (c) shows the signals from panels (a) and (b) in the order in which they were actually acquired during the measurements, so that about 8 hours time elapsed between the acquisition of the bottom and top signals. One can see that the onset of the signals shifts with time first towards negative and then towards positive time delays. This shows that the orientation of the quarter wave plate does not affect the time delay between the pump and probe pulses significantly. However, various drifts in parts of the apparatus such as the laser or the sample holder may have a significant effect upon it. Also, it seems reasonable to assume that, in order to compare different transient polarisation signals, one may define their temporal position relative to the reflectivity signal that was simultaneously measured.

The experimental configurations for measurements with an elliptically and linearly polarised pump are different in that the positions of the pump quarter wave plate and polarizer are reversed, which may change the overlap of the pump and probe. However, it may easily be shown that the resulting change of the pump-probe time delay, estimated for a grazing incidence as the spot diameter divided by the speed of light, cannot exceed 50 fs. Note that in the latter case the pump and probe would no longer be overlapped, and so this change in the time delay would be accompanied by an almost 100% reduction of the signal. Hence, it is reasonable to assume that a change of the time delay due to this effect must not exceed 10-15 fs. Since the same change must be present both in the reflectivity and rotation, it can be compensated for by defining the time delay relative to the reflectivity.

2.5 Summary

In summary, the different experimental configurations used in the various chapters of this thesis were described within a single framework so as to demonstrate the broad applicability of the pump-probe experimental method, while additional details relevant to particular experiments will be given within the appropriate chapters of the thesis. The experimental artefacts that may influence the measurement are discussed as well as the means of their suppression.

Chapter 3. Theory of Uniform Modes of Magnetisation Dynamics in Rectangular Double Layer Ferromagnetic Elements

3.1 Introduction

Despite several decade of intense study, thin film magnetic materials remain one of the main subjects of investigations within modern solid state physics. The stabilisation of new structural phases and modulation of chemical composition at the nanoscale have led to new magnetic properties of significant technological interest. The dynamical properties of the materials are determined by the gigahertz spectrum of spin wave excitations[54]. The latter have been studied by techniques such as microwave ferromagnetic resonance[84,85] and Brillouin light scattering[86,87]. Analyses of the spin wave frequencies have been used to quantify magnetic properties such as the saturation magnetisation[53], the gyromagnetic ratio[53], the anisotropy[53], and the exchange coupling[88]. However, further technological development requires an even deeper understanding of the picosecond magnetisation dynamics of thin film elements with micron and nanometre dimensions. For example, precessional magnetic switching requires precise control of the relative phase of different frequency components that may also interact due to the inherent nonlinearity of the magnetisation dynamics[89].

Recently, time resolved magneto-optical measurements have emerged as a new means by which to study picosecond magnetisation dynamics in the time domain, providing an alternative to the frequency domain ferromagnetic resonance and Brillouin light scattering techniques. Several variations upon the basic technique have been

demonstrated. The time resolved linear MOKE is sensitive to all three components of the vector magnetisation[66], while the time resolved magnetic second harmonic generation has proved to be effective in studying the evolution of the in-plane magnetisation components[90]. Measurements must also be made with very high spatial resolution. Due to the diffraction limit, an optical probe cannot be focused to a spot diameter smaller than about 500 nm. Due to the shorter wavelengths used, the time resolved X-ray magnetic circular dichroism technique[91] has promised spatial resolution down to 20 nm, but its temporal resolution is limited to about 50 ps. On the other hand, this technique has the important property of element selectivity especially that is useful in studying multilayered materials. Time resolved magnetoresistance[80,92] and pulsed inductive microwave magnetometry[93,94] are also time domain, although not pump-probe, techniques. Their temporal resolution is limited by the bandwidth of the sampling oscilloscope used. However, they may be easier to implement at cryogenic temperatures[95].

Small amplitude precessional oscillations have been studied by the pump-probe technique in order to characterise magnetic anisotropy and damping[96], and also to demonstrate coherent control of magnetisation precession[97,79]. The large amplitude reorientation of the magnetisation has been studied in Ref. 17,90,98. The spatial uniformity of the precession has begun to be explored using the time resolved scanning Kerr microscopy[99,100] leading to a realisation that long wavelength magnetostatic modes play an important role in experiments in which either the pulsed field is inhomogeneous[101] or the lateral dimensions of the sample are small[102]. However, the spatial character of the magnetisations dynamics will be discussed in detail in the next chapter of the thesis.

In recent experiments performed by the Exeter group, magnetisation dynamics in continuous film spin valve structures[29,31] and micron sized square permalloy

elements[6,30-32,34] were studied. Studies of spin valve elements of various shapes are to be expected in future, because spin valve elements are of great technological interest for use in high density recording heads and magnetic sensors[13]. Although excitation of spin waves is likely to take place in patterned elements due to the spatial confinement, the uniform mode of the magnetisation precession is still expected to make a dominant contribution to the sample response. Hence in this chapter, a theory of precessional magnetisation dynamics and relaxation in an exchange coupled magnetic double layer is developed in the macrospin approximation. In order to apply the theory to patterned magnetic elements of rectangular shape, a fourfold "shape anisotropy" term has also been included into the model. The theory is illustrated by application of the results to the optical ferromagnetic resonance data from Ref. 31.

3.2 Macrospin Theory of Magnetisation Precession

3.2.1 Macrospin Model of a Spin Valve Element

The structure of the spin valves studied in Ref. 29 is shown schematically in Figure 3.1. The ferromagnetic $Ni_{81}Fe_{19}$ (permalloy) and Co layers are separated by a nonmagnetic Cu spacer layer with thickness *d* equal to 10, 20, and 30 Å in samples S1, S2, and S3, respectively. The Co layer is pinned in a saturated magnetic state by the exchange bias field from an IrMn antiferromagnetic layer so that only the magnetisation of the permalloy layer may be rotated by an external magnetic field. The structure may be used as a sensor due to the dependence of its current-in-plane resistance upon the relative orientation of the magnetisation in the two ferromagnetic layers.

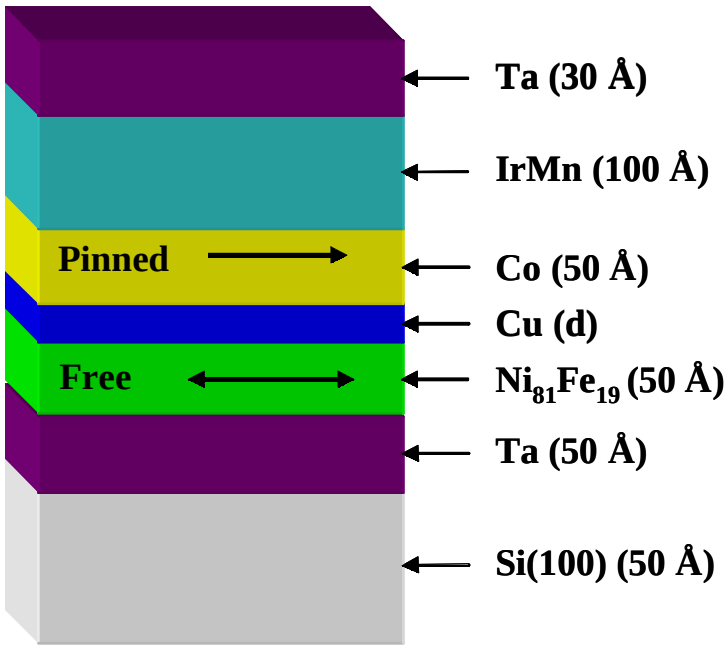

Figure 3.1 The structure of the spin valves studied in Ref. 29 is shown schematically.

In order to describe the magnetisation dynamics in the structure, let us write the Landau-Lifshitz equation with the Gilbert relaxation term in the following form

$$\frac{\partial \mathbf{M}_i}{\partial t} = -\gamma_i \left[\mathbf{M}_i \times \mathbf{H}_{\mathrm{E,i}}\right] + \frac{\alpha_i}{M_i}\left[\mathbf{M}_i \times \frac{\partial \mathbf{M}_i}{\partial t}\right], \qquad (3.2.1)$$

where indices i=1,2 stand for the parameters describing the Co and permalloy layers, respectively. In what follows, we first assume that the lateral dimensions of the element are much greater than its thickness. Also, only the zero wave number excitation will be considered, and so the exchange interaction energy term may be dropped. It is then convenient to consider the areal density of the magnetic moment in the layers $\mathbf{M}_i d_i$, and the areal density of the free energy of the entire system $E=w(d_1+d_2)$, where d_i are the thicknesses of the magnetic layers. These approximations constitute the basis of the so-called macrospin model and are generally not valid for a rigorous description of magnetisation dynamics in magnets with finite lateral dimensions. However, the formulae derived below may still provide a valuable starting point for the analysis and may save some computation time.

Let us therefore define the magnetic free energy density per unit area of the system as

$$E = \sum_{i=1,2} d_{\mathrm{i}} \left\{ \begin{array}{l} -\mathbf{M}_i \cdot \mathbf{H} - \dfrac{\beta_{2,i}}{2}(\mathbf{M}_i \cdot \mathbf{k}_i)^2 \\ -\dfrac{\beta_{4,i}}{4}[(\mathbf{M}_i \cdot \mathbf{p}_{1,i})^4 + (\mathbf{M}_i \cdot \mathbf{p}_{2,i})^4] \\ -(\mathbf{M}_i \cdot \mathbf{b}_i) H_{\mathrm{ex},i} + 2\pi(\mathbf{M}_i \cdot \mathbf{n})^2 - \mathbf{M}_i \cdot \mathbf{h}_i(t) \end{array} \right\} - A_{12}\mathbf{M}_1 \cdot \mathbf{M}_2 , \qquad (3.2.2)$$

where $\beta_{4,i}$ and $H_{\mathrm{ex},i}$ are the four fold anisotropy constants and the exchange bias field of each layer, respectively, and we have introduced the uniaxial anisotropy constants of the layers $\beta_{2,i} = \dfrac{2K_{2,i}}{M_i^2}$ that have form of the demagnetising coefficients. In layer i the unit vectors $\mathbf{k}_i$, $\mathbf{p}_{1,i}$, $\mathbf{p}_{2,i}$, and $\mathbf{b}_i$ lie parallel to the uniaxial anisotropy axis, the two four fold

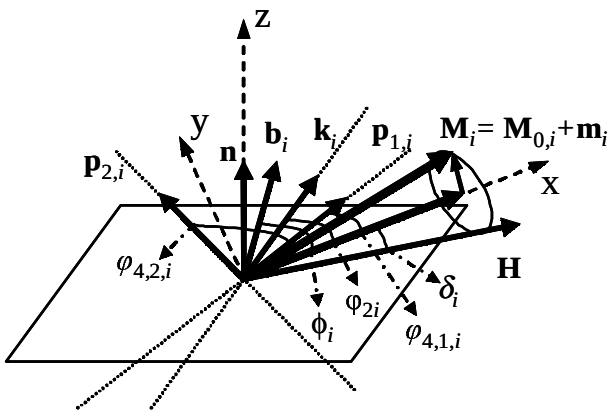

Figure 3.2 The geometry for the calculation is shown. The directions of the vectors in each layer are defined by the angles they make with the x-axis that is parallel to the layer magnetisation.

in-plane easy axes, which may be not mutually perpendicular in general case, and the exchange bias field, respectively. The constant A_{12} determines the strength of the interlayer coupling, $\mathbf{h}_i(t)$ denotes the pulsed magnetic field, and $\mathbf{n}$ is the unit vector normal to the sample plane. The geometry for the calculation is sketched in Figure 3.2.

The total effective magnetic field acting upon layer i is defined as

$$\mathbf{H}_{\text{eff},i} = -\frac{1}{d_i}\nabla_{\mathbf{M}_i} E\,, \tag{3.2.3}$$

where the gradient is taken with respect to the Cartesian components of $\mathbf{M}_i$, and is equal to

$$\mathbf{H}_{\text{eff},i} = \mathbf{H} + \mathbf{b}_i H_{\text{ex},i} + \beta_{4,i}((\mathbf{M}_i \cdot \mathbf{p}_{1,i})^3 \mathbf{p}_{1,i} + (\mathbf{M}_i \cdot \mathbf{p}_{2,i})^3 \mathbf{p}_{2,i}) + \beta_{2,i}(\mathbf{M}_i \cdot \mathbf{k}_i)\mathbf{k}_i - 4\pi(\mathbf{M}_i \cdot \mathbf{n})\mathbf{n} + \frac{A_{12}}{d_i}\mathbf{M}_j + \mathbf{h}_i(t) \tag{3.2.4}$$

3.2.2 Uniform Mode Spectrum and Damping

In the low perturbation limit, the magnetisation in each layer can be represented as $\mathbf{M}_i=\mathbf{M}_{0,i}+\mathbf{m}_i(t)$, $M_{0,i}>>m_i(t)$, $H>>h_i(t)$, where $\mathbf{m}_i(t)$ is the small deviation from the equilibrium magnetisation $\mathbf{M}_{0,i}$. In general, the static magnetisation in each layer is not parallel to the direction of the applied field, but is parallel to the static effective field so that the net torque acting upon the magnetisation is equal to zero (1.1.1). Hence, the following equation must be satisfied

$$\begin{aligned}&\mathbf{H}+\mathbf{b}_i H_{\mathrm{ex},i}+\beta_{4,i}((\mathbf{M}_{0,i}\cdot\mathbf{p}_{1,i})^3\mathbf{p}_{1,i}+(\mathbf{M}_{0,i}\cdot\mathbf{p}_{2,i})^3\mathbf{p}_{2,i})+\\&\beta_{2,i}(\mathbf{M}_{0,i}\cdot\mathbf{k}_i)\mathbf{k}_i-4\pi(\mathbf{M}_{0,i}\cdot\mathbf{n})\mathbf{n}+\frac{A_{12}}{d_i}\mathbf{M}_{0,j}=a_i\mathbf{M}_{0,i}\end{aligned}\quad , \tag{3.2.5}$$

where a_i is some constant. The static magnetisation configuration is first obtained by minimising the free energy (3.2.2) using the steepest descents method. Values of a_i are then easily calculated.

By retaining only terms linear in $m_i(t)$ and $h_i(t)$ in equations (3.2.1) and (3.2.4), and using equation (3.2.5), the linearised equation of motion of the magnetisation becomes

$$\frac{\partial\mathbf{m}_i}{\partial t}=-\gamma_i\left[\mathbf{M}_{0,i}\times\left(\begin{array}{l}3\beta_{4,i}((\mathbf{M}_{0,i}\cdot\mathbf{p}_{1,i})^2(\mathbf{m}_i\cdot\mathbf{p}_{1,i})\mathbf{p}_{1,i}+\\(\mathbf{M}_{0,i}\cdot\mathbf{p}_{2,i})^2(\mathbf{m}_i\cdot\mathbf{p}_{2,i})\mathbf{p}_{2,i})+\\\beta_{2,i}(\mathbf{m}_i\cdot\mathbf{k}_i)\mathbf{k}_i-4\pi(\mathbf{m}_i\cdot\mathbf{n})\mathbf{n}+\\\frac{A_{12}}{d_i}\mathbf{m}_j+\mathbf{h}_i(t)-a_i\mathbf{m}_j\end{array}\right)\right]+\frac{\alpha_i}{M_i}\left[\mathbf{M}_i\times\frac{\partial\mathbf{m}_i}{\partial t}\right]. \tag{3.2.6}$$

As shown in Figure 3.2, the Cartesian coordinate systems in each layer are defined so that their x-axes are parallel to the static magnetisation and both z-axes are parallel to the vector **n**. In the linear regime, the magnitude of the magnetisation in each layer is equal to that in equilibrium. Also, the vectors $\mathbf{m}_i$ are perpendicular to the latter and, hence, have only y and z components in the chosen coordinate systems. It follows then that the two coupled vector equations (3.2.6) represent a system of four coupled scalar

linear inhomogeneous equations. The general solution of this system is given by the sum of its particular integral and the general integral of the complementary system of differential equations obtained from (3.2.6) by dropping the term **h**(t). The latter system is solved by substituting $\mathbf{m}_i=\mathbf{m}_{0,i}\exp(-i\Omega t)$. Then, a system of algebraic equations with respect to the mode amplitudes in the layers is obtained. The system has a non-trivial solution if and only if the determinant of its coefficients, which are complex numbers, is equal to zero. This equation can be solved to obtain the spectrum of uniform excitations of the sample. Since the coefficients are complex, the frequencies $\Omega_{\pm}=\omega_{\pm}+i/\tau_{\pm}$ are also complex and are given by

$$\omega_{\pm}=\sqrt{0.5(\xi_1+\xi_2+C_1B_2+B_1C_2\mp\sqrt{(\xi_1+\xi_2+C_1B_2+B_1C_2)^2-4(F_{01}F_{02}-C_1C_2)(G_{01}G_{02}-B_1B_2)})}\,, \tag{3.2.7}$$

and

$$\frac{1}{\tau_{\pm}}=0.5\frac{-(\eta_1+\eta_2)\omega_{\pm}^2+\eta_1\xi_2+\eta_2\xi_1-(\alpha_1F_{02}+\alpha_2F_{01})B_1B_2-(\alpha_1G_{02}+\alpha_2G_{01})C_1C_2}{-2\omega_{\pm}^2+\xi_1+\xi_2+C_1B_2+B_1C_2}\,, \tag{3.2.8}$$

where

$$G_{0,i}=\gamma_i M_{0,i}(4\pi+a_i)\,, \tag{3.2.9}$$

$$B_i=-\frac{A_{12}}{d_i}\gamma_i M_{0,i}\,, \tag{3.2.10}$$

$$F_{0,i}=\left(a_i-\beta_{2,i}\sin^2\varphi_{2,i}-\frac{3}{4}\beta_{4,i}{M_{0,i}}^2(1-\cos 4\varphi_{4,i})\right)\gamma_i M_{0,i}\,, \tag{3.2.11}$$

$$C_i=B_i\cos\psi\,, \tag{3.2.12}$$

$$a_i=\frac{H}{M_{0,i}}\cos\delta_i+\frac{H_{\mathbf{ex},i}}{M_{0,i}}\cos\phi_i+\beta_{2,i}\cos^2\varphi_i+\beta_{4,i}{M_{0,i}}^2(\sin^4\varphi_{4,i}+\cos^4\varphi_{4,i})+\frac{A_{12}M_{0,j}}{d_iM_{0,i}}\cos\psi\,, \tag{3.2.13}$$

$$\xi_i = F_{0,i} G_{0,i}\,, \tag{3.2.14}$$

$$\eta_i = \alpha_i (F_{0,i} + G_{0,i})\,. \tag{3.2.15}$$

Here δ_i, ϕ_i, $\varphi_{2,i}$, and $\varphi_{4,i}=\varphi_{4,1,i}$ are the angles that **H**, $\mathbf{b}_i$, $\mathbf{k}_i$, and $\mathbf{p}_{1,i}$ describe with M_i, as shown in Figure 3.2, and ψ is the angle between the x-axes of the layers. For the sake of brevity, an additional assumption has been made that the two four-fold axes are mutually perpendicular, and hence $\varphi_{4,2,i}=\varphi_{4,1,i}+\pi/2=\varphi_{4,i}+\pi/2$. Since the damping term in the Landau-Lifshitz equation is defined only to first order on the damping constant, which is usually small, only terms linear in the Gilbert parameter terms have been retained above.

Equations (3.2.7)-(3.2.15) predict that two resonant modes will occur. In the absence of interlayer coupling, these are simply the uniform mode solutions for the individual layers, reducing to

$$\begin{aligned}\omega_i^2 = \xi_i = \gamma_i{}^2 &\left(\begin{array}{l} H\cos\delta_i + H_{ex,i}\cos\phi_i + \\ \beta_{2,i} M_{0,i}\cos 2\varphi_i + \beta_{4,i} M_{0,i}{}^3 \cos 4\varphi_{4,i} \end{array} \right) \\ \times &\left(\begin{array}{l} H\cos\delta_i + H_{\mathbf{ex},i}\cos\phi_i + \\ \beta_{2,i} M_{0,i}\cos^2\varphi_i + \beta_{4,i} M_{0,i}{}^3 \dfrac{3+\cos 4\varphi_{4,i}}{4} + 4\pi M_{0,i} \end{array} \right), \end{aligned} \tag{3.2.16}$$

$$\begin{aligned}\frac{1}{\tau_i} = \frac{1}{2}\eta_i = \\ \alpha_i\gamma_i &\left(\begin{array}{l} H\cos\delta_i + H_{ex,i}\cos\phi_i + \\ \beta_{2,i} M_{0,i} \dfrac{3\cos 2\varphi_i + 1}{4} + \beta_{4,i} M_{0,i}{}^3 \dfrac{5\cos 4\varphi_{4,i} + 3}{8} + 2\pi M_{0,i} \end{array} \right). \end{aligned} \tag{3.2.17}$$

Otherwise, they correspond to the "acoustic" and "optical" modes in which the magnetisations of the two layers precess in and out of phase, respectively. The equations may be used to simulate the dependence of the observed mode frequencies and relaxation rates upon the strength and orientation of the static field, allowing the

values of the magnetisation, gyromagnetic ratio, anisotropy, exchange bias, exchange coupling and damping parameter to be deduced.

3.2.3 Signal Shapes in Time and Frequency Domains

Finding the particular integral of equation (3.2.6) for a realistic shape of the pulsed magnetic field, which may be quite complicated, is a difficult problem that must be solved numerically[99]. On the other hand, it is easy to check that the function $\mathbf{C}_h \exp(-t/\tau_h)$ represents the particular integral for

$$\mathbf{h}_i(t) \propto \exp\left(-\frac{t}{\tau_h}\right) \tag{3.2.18}$$

and a certain choice of constant $\mathbf{C}_\mathrm{h}$ so that the general solution of equation (3.2.6) is given by

$$\mathbf{m}_i(t) = \mathbf{C}_- \exp\left(-\frac{t}{\tau_-} + i\omega_- t\right) + \mathbf{C}_+ \exp\left(-\frac{t}{\tau_+} + i\omega_+ t\right) + \mathbf{C}_\mathrm{h} \exp\left(-\frac{t}{\tau_h}\right), \tag{3.2.19}$$

where $\mathbf{C}_\pm$ are arbitrary constants and τ_h is the field decay time.

In order to account for the finite duration of the signal, we multiply this expression by the Heaviside step function, and in order to account for the finite rise time, we convolve this with a Gaussian kernel. Then the following function is obtained, which is not a rigorous solution of the Landau-Lifshitz equation,

$$\mathbf{m}_i^*(t_\mathrm{d}) = \frac{1}{2}\left\{\begin{array}{l} \mathbf{C}_{-,i}\left(1+erf\left(\frac{t_d}{\sigma\sqrt{2}} - \frac{\sigma}{\tau_-\sqrt{2}}\right)\right)\exp\left(\frac{\sigma^2}{2\tau_-^2} - \frac{t_d}{\tau_-} + \mathrm{i}\omega_- t_d\right) + \\ + \mathbf{C}_{+,i}\left(1+erf\left(\frac{t_d}{\sigma\sqrt{2}} - \frac{\sigma}{\tau_+\sqrt{2}}\right)\right)\exp\left(\frac{\sigma^2}{2\tau_+^2} - \frac{t_d}{\tau_+} + \mathrm{i}\omega_+ t_d\right) + \\ + \mathbf{C}_{\mathrm{h},i}\left(1+erf\left(\frac{t_d}{\sigma\sqrt{2}} - \frac{\sigma}{\tau_h\sqrt{2}}\right)\right)\exp\left(\frac{\sigma^2}{2\tau_h^2} - \frac{t_d}{\tau_h}\right) \end{array}\right\}, \tag{3.2.20}$$

where the parameter σ can be adjusted in order to set an appropriate rise time for the signal. At time delays t_d that are comparable to the pulsed field rise time, the function

may deviate from a rigorous solution for the pulsed field given by the third term in the right hand side of (3.2.18). However, it approaches asymptotically the rigorous solution at longer time delays if constants $\mathbf{C}_{\pm,i}$ and $\mathbf{C}_{\mathrm{h},i}$ are chosen so as to correctly describe the result of the interaction between the rising field and the magnetisation.

The linear MOKE response of a single film must by calculated by substituting expression (3.2.20) into equations (1.2.3)-(1.2.8). The calculation is considerably more complicated in the case of a multilayer where multiple reflections of the optical fields at all interfaces should be taken into account[103]. However, for small amplitude motion of the magnetisation it can be expected that the real and imaginary parts of expression (3.2.20), with indices *i* dropped and scalar constants $C_{\pm}$ and C_{h} treated as adjustable parameters, will describe the response to a reasonable accuracy.

It is also useful to have analytical expressions for the line profile of the Fourier spectra of the signals. From (3.2.20), without indices *i*, these are easily shown to be

$$s_{\omega} = s_{-} + s_{+} + s_{h}, \tag{3.2.21}$$

where

$$s_{\pm} = \frac{\mathrm{C}_{\pm} \exp\left(-\frac{\sigma^2(\omega-\omega_{\pm})^2}{2}\right)}{1/\tau_{\pm} + i(\omega-\omega_{\pm})}, \tag{3.2.22}$$

$$s_{\mathrm{h}} = \frac{\mathrm{C}_{\mathrm{h}} \exp\left(-\frac{\sigma^2\omega^2}{2}\right)}{1/\tau_{\mathrm{h}} + i\omega}. \tag{3.2.23}$$

It is important to note that according to equation (3.2.20) the response of each layer contains contributions from both the acoustical and optical modes, and hence the spectrum of the signal (3.2.21)-(3.2.23) will contain two frequencies even if only one layer of the double layer system is actually probed.

3.3 Comparison with Experiment

Examples of the application of the derived formulae to the description of experimental data are presented in Figure 3.3. The symbols in Figure 3.3 (a) correspond to the measurements of the uniform mode frequency at different values of the bias field strength for a magnetron sputtered Co film sample with composition Si(100)/Co(100Å)/Al_2O_3(100Å)[31]. Since the sample had an opaque substrate, the measurements were carried out using a transmission line structure deposited on glass, as shown in Figure 2.2 (d). Branches A and B show the frequency when the bias field was applied parallel to the easy and hard axes, respectively. The solid lines represent simulations with equations (3.2.16),(3.2.9)-(3.2.14). The fourfold anisotropy term was neglected in this case, and equation (3.2.13) was solved numerically using the steepest descent method[31].

Assuming the bulk value of 1480 emu/cm^3 for the magnetisation, the best agreement between simulation and data was obtained for a g-factor of 2.15, a uniaxial anisotropy constant K_2 of 4 x 10^4 erg/cm^3, and with the uniaxial easy axis set 20° from the direction of the static field in measurement configuration A. The agreement between measurement and simulation is very good except for the lowest field values in configuration B where the static field is applied close to the in-plane hard axis. A possible reason for this may be that the static and, hence, the dynamic magnetisations are nonuniform in this field regime.

The two branches in Figure 3.3 (b) correspond to the two modes (acoustical and optical) of precession in a spin valve structure with composition as shown in Figure 3.1, with the spacer layer thickness d equal to 20 Å[29,31]. Each pair of frequencies was extracted from the same signal. The measurements were made in the same manner as

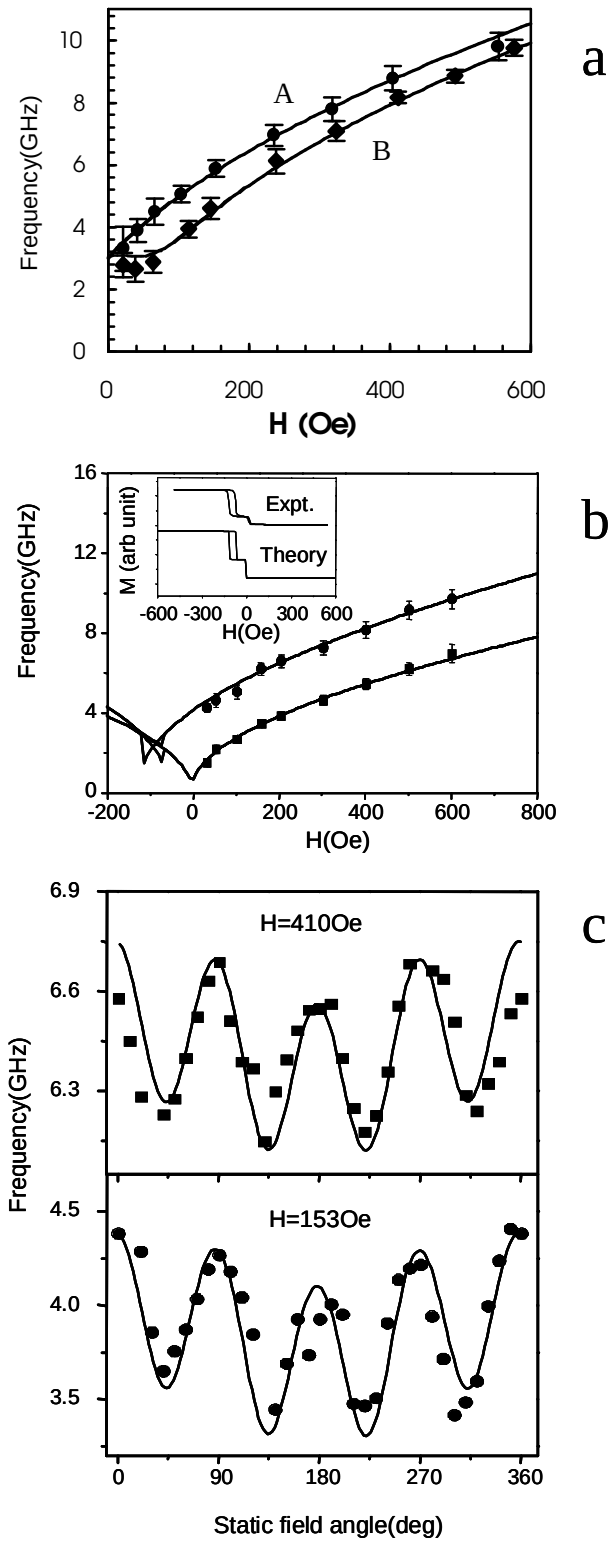

Figure 3.3 The dependence of the uniform mode frequencies upon the strength and direction of the in-plane static magnetic field is presented for different samples, as explained in the text. The symbols denote data points while the lines are simulations. The inset in (b) shows the measured and simulated MOKE hysteresis loops. The figures are taken from Ref. 31.

for the Co film with a static field applied parallel to the easy axis. The solid curves represent simulations with equations (3.2.7),(3.2.9)-(3.2.14), again neglecting the fourfold anisotropy term, and using the steepest descent method for the calculation of the static magnetic configuration. In the inset the simulated easy axis hysteresis loop is compared to the measured MOKE hysteresis loop.

In the simulations, the easy axis directions were found to lie parallel to the direction of the growth field. Values of 2.1 and 2.0 were assumed for the g-factors of the Co and $Ni_{81}Fe_{19}$, while values of 1150 and 780 emu were obtained for the effective magnetisation, which compare with bulk values of 1420 and 860 emu. The Co anisotropy constant was found to be equal to 3×10^4 erg/cm^3, which is similar to the single Co film previously described, while that for $Ni_{81}Fe_{19}$ was determined to be about 10^3 erg/cm^3. The extracted values of the exchange bias field and interlayer coupling parameter were 95 Oe and 1.7×10^{-9} cm, respectively.

As one can see from Figure 3.3 (c), the model is also capable of describing the angular variation of the mode frequency in an element of square shape. The element was a 10 μm permalloy square of 150 nm thickness. The frequency is plotted against the orientation of the static in-plane field, the strength of which is shown in the Figure. The frequency varies with a period of 90°, suggesting that the anisotropy in the element is predominantly fourfold. There is also a contribution with period of 360° that is associated with the pulsed field that was applied in the sample plane in this particular case. The exchange bias term in the model, with a field magnitude of 12 Oe, could be used to reproduce this effect. The curves also assume values of 2.1 for the g-factor, 860 emu for the magnetisation, 0.9×10^3 erg/cm^3 and 5×10^{-8} cm^3/erg for the uniaxial and fourfold anisotropy constants, respectively

Because of the complicated pulsed field profile and the short duration of the measured signal, the use of the derived expressions for analysis of the signal temporal

shape did not bring any more information in comparison with the conventional fast Fourier transform analysis.

3.4 Summary

In this chapter, a theory of precessional magnetisation dynamics and relaxation in an exchange coupled magnetic double layer element of rectangular shape was developed in the macrospin approximation, and successfully used to describe the results of optical ferromagnetic resonance experiments.

Chapter 4. Time Resolved Scanning Kerr Microscopy Investigation of Spin Wave Excitations in Ultrasmall Magnetic Elements and Arrays

4.1 Introduction

Hopes for increasing magnetic recording densities to 1 Terabit per square inch and beyond lie with the use of patterned recording media[104]. In such media, a bit of information is represented by the orientation of the magnetic moment of a single element. A simple calculation shows that in order to achieve a density of 1 Terabit per square inch, the element size must be equal to 25 nm, neglecting the inter-element separation, and even smaller, if elements are to be reasonably separated. In the presence of such strong spatial confinement, the spectrum of magnetic excitations is dominated by finite wavelength modes[33,59,87,101,102,105], as opposed to continuous thin films where the uniform mode is dominant[31].

Larger amounts of stored information also require faster recording schemes. The most promising of these relies upon ultrafast precessional switching[16,17] of small magnetic elements. The basic idea is that the magnetisation of a recorded element is driven to a large amplitude precessional motion by a perpendicular magnetic field pulse. The pulsed field is then switched off after exactly a half period of precession. If the new orientation of the magnetisation corresponds to or is sufficiently close to an equilibrium state, then the element will remain in this state. This is because the Landau-Lifshitz differential equation (1.1.13) is of first order with respect to time, and so the magnetic motion has no inertia. In other words, the duration of the magnetic field pulse

must match a half-period of precession, which is impossible if the precession is characterised by the presence of several eigenmodes of different frequency, such as in the case of a small magnetic element. Since the different eigenmodes have different wavelengths, the switching in the latter case will be spatially incoherent. While some regions of the element will have switched, others will continue to precess and may contribute to noise within the recording system. Hence, it is essential to study and control magnetisation dynamics simultaneously within both the time and space domains.

The excitation of spin wave eigenmodes in thin magnetic films and elements has been studied experimentally by Brillouin light scattering[106], time resolved scanning Kerr microscopy[6,30-33,102,105], ferromagnetic resonance[107-110], and pulsed inductive microwave magnetometry[94,111]. The development of theoretical understanding of the frequency and spatial profile of these modes is still in progress[59-61,112-114]. Due to the demand for greater recording densities, the elements in the patterned recording medium must be closely packed, promoting interactions between elements via stray magnetic fields. Therefore the dynamical response of an individual element is in general determined by the spectrum of collective excitations of the entire array. Moreover, current experimental methods do not yet provide sufficient spatial resolution for the dynamical properties of a single nanoscale element to be studied directly. Consequently the magnetic properties of the element must be deduced from measurements made on the entire array[106,108-111].

In this chapter, investigations of the precessional dynamics in NiFe (27Å) / CoFe (10Å) single microelement and nanoelement arrays are presented. Using the time resolved scanning Kerr microscope as a submicron probe of the magnetisation dynamics at the centre of a sample, we record its time dependent response to a pulsed magnetic field. The frequencies of the precessional modes of the

samples are determined from fast Fourier transform power spectra calculated from the time resolved signals. Micromagnetic simulations of the sample response to both pulsed and harmonic magnetic fields are then used to identify the origin of the observed modes.

4.2 Samples and Experimental Details

The measurements were performed upon a square element of 6000 nm size and upon 64, 120, 220, 425, and 630 nm elements that formed square arrays of about 4000 nm total size. The samples were patterned using electron beam lithography. The dimensions of the elements and the element arrays are summarised in Table 4.1. The scanning electron microscope images of some of the arrays are shown in Figure 4.1. In particular, one can see that the 120 nm elements came out slightly rounded due to windage. The 64 nm elements are much more rounded for the same reason.

The composition of the elements was Ta (50 Å) / $Co_{80}Fe_{20}$ (10 Å) / $Ni_{88}Fe_{22}$ (27 Å - x) / NiFeTa(x) / Ta (100 Å), where x denotes the thickness of permalloy lost due to the interdiffusion with Ta. The values of the thicknesses were traceable to calibration measurements performed by X-ray diffraction. The

Element Size, nm	Element Aspect Ratio	Array Size, μm	Number of Elements in Array	Inter-element Separation, nm	Array Filling Factor, %
6000	2410	N/A	1	N/A	100
630	253	3.3	5 X 5	37.5	91
425	171	4	9 X 9	21.9	91
220	88	4	13 X 13	95	51
120	48	3.9	25 X 25	37.5	59
64	26	3.66	33 X 33	48.4	33

Table 4.1 The dimensions of the elements and the element arrays studied in this chapter are summarised.

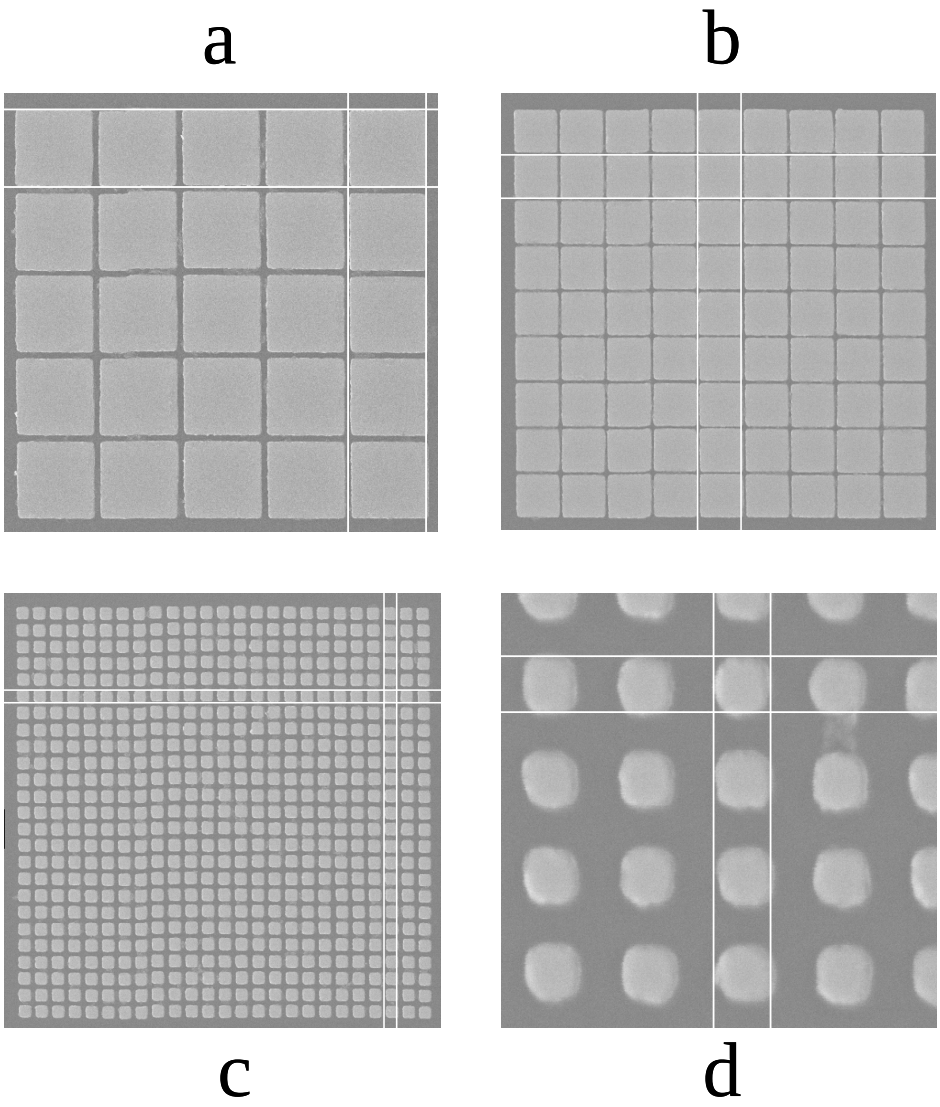

Figure 4.1 Scanning electron microscope images of the arrays studied are shown for elements of (a) 630 nm, (b) 425 nm, (c) 120 nm, and (d) 64 nm size. The cursor size in (a), (b), and (c) is equal to the corresponding element size, while in (d) it is equal to 65 nm. The images are courtesy of Dr. J.R. Childress and Dr. J.A. Katine.

compositions of the NiFe and CoFe alloys were chosen so that the magnetostriction of these two layers would compensate each other, and the bilayer as a whole would have vanishing magnetostriction. The CoFe alloy composition also gave a stable fcc structure. The direction of the easy axis was set in the samples by the field annealing.

A comparison of results of static magnetometry measurements made upon sheet samples of different thickness co-deposited with the elements showed that 12.1 Å of NiFe was lost due to interdiffusion with Ta. The magnetisations of the CoFe and NiFe were deduced to be equal to 1445 emu/cm^3 and 585 emu/cm^3, respectively. Since the two layers were strongly coupled by the interlayer exchange interaction, we can treat them as a single layer with thickness equal to the sum of their thicknesses (24.9 Å) and with magnetisation given by an arithmetical average of their saturation magnetisations (930 emu/cm^3). The uniaxial and average surface anisotropy constants K_2 and K_s were found to be equal to 5120 erg/cm^3 and 0.11 erg/cm^2, respectively.

In order to make pump-probe measurements, the elements were formed in between the tracks of a transmission line structure with a 30 μm track width and separation, as shown in Figure 2.2 (a), so as to experience an out-of-plane pulsed magnetic field. The measurements were performed in the time resolved scanning Kerr microscopy configuration described in detail in section 2.2 of the experimental chapter. In this configuration, the measured signal was proportional to the polar Kerr rotation, and hence, to the out-of-plane component of the magnetisation. In measurements made upon the element arrays, several elements were typically in the area probed by the microscope. Hence, the measurement was sensitive only to the average response of the elements, falling under the probe spot. The maximum pump-probe time delay was 4 ns. A static field **H** was applied in the plane of the sample and its strength and orientation were varied during the experiment. Each value of the static field was approached from a much greater value, typically about 1-2 kOe, that was sufficient to cause saturation. The orientation of the bias field will be denoted by the angle Θ made with an axis perpendicular to the tracks so that Θ=90°, 270° and Θ=0°, 180° when field is parallel and perpendicular to the tracks, respectively.

4.3 Experimental Results

4.3.1 6 µm Square

First, the measurements made upon the 6 µm element are described. Two types of dynamic Kerr measurement were performed with the probe spot focused at the centre of the element. Firstly, the static field strength H was varied with the field vector **H** parallel to the expected directions of the easy (EA) and hard (HA) anisotropy axes of the element, which were parallel and perpendicular to the tracks of the transmission line structure, respectively. Figure 4.2 (a) and (b) show typical measurements of the time

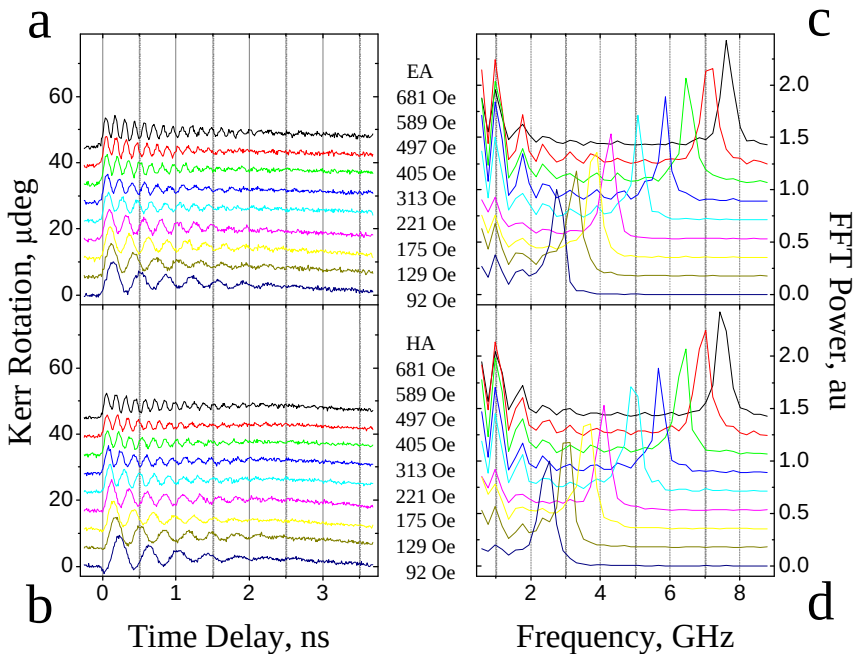

Figure 4.2 Typical time resolved Kerr rotation signals measured from the 6000 nm element are presented in panels (a) and (b) for different values of the bias field applied parallel to the expected easy (EA) and hard (HA) anisotropy axes, respectively. The Fourier spectra of the corresponding signals in panels (a) and (b) are presented in panels (c) and (d), respectively.

dependent Kerr rotation. A linear background has been subtracted from the signals. The signals reveal a damped precession. The fast Fourier transform spectra of the signals in panels (a) and (b) are shown in Figure 4.2 (c) and (d), respectively. Since the oscillations decayed well within the duration of the scan, the Fourier transforms were performed using a rectangular window function. As well as the field dependent peaks at higher frequencies, one can also see lower frequency peaks, the positions of which do not depend upon the bias field strength. The latter peaks originate from the pulsed field

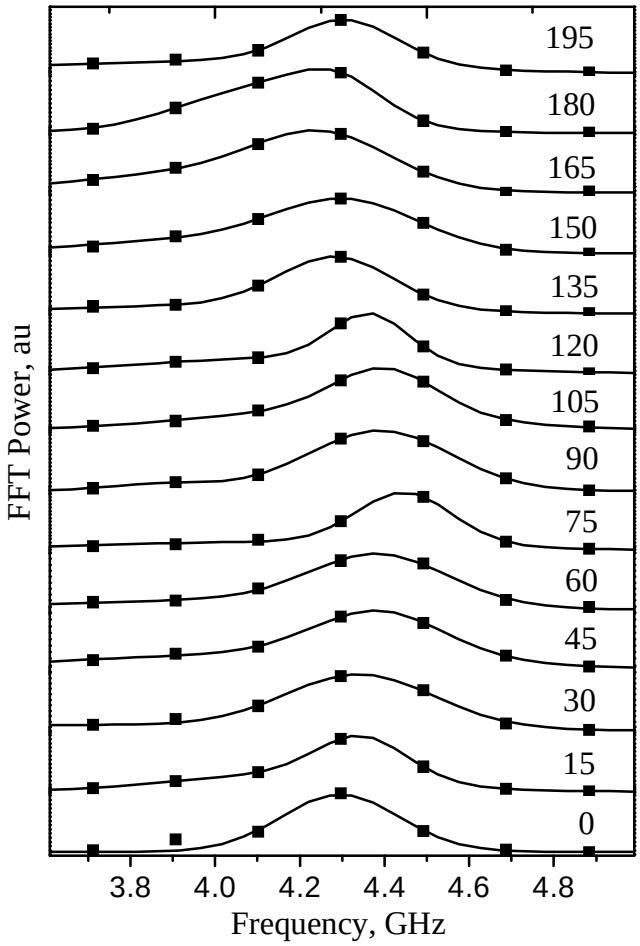

Figure 4.3 The Fourier spectra of time resolved signals acquired from the 6000 nm element as a bias field of the 240 Oe was applied in different directions in the sample plane are shown. The symbols represent data points, and the lines are Gaussian peak fits.

profile and can be clearly distinguished from the sample response. However, an accurate determination of frequency seems infeasible for frequencies less than approximately 2 GHz. Kerr images of the dynamic magnetisation distribution acquired at different time delays between the pump and the probe (not shown) did not reveal any spatial nonuniformity. Hence, the only observed mode of magnetisation precession was identified as the uniform mode, as might be expected for such a large element.

In a second type of measurement, the direction of the bias field was varied, while its magnitude was kept constant. In Figure 4.3, the fast Fourier transform spectra are presented for different directions of a bias field with magnitude of 240 Oe. The uniform precession frequency was determined from the fast Fourier transform spectra by fitting

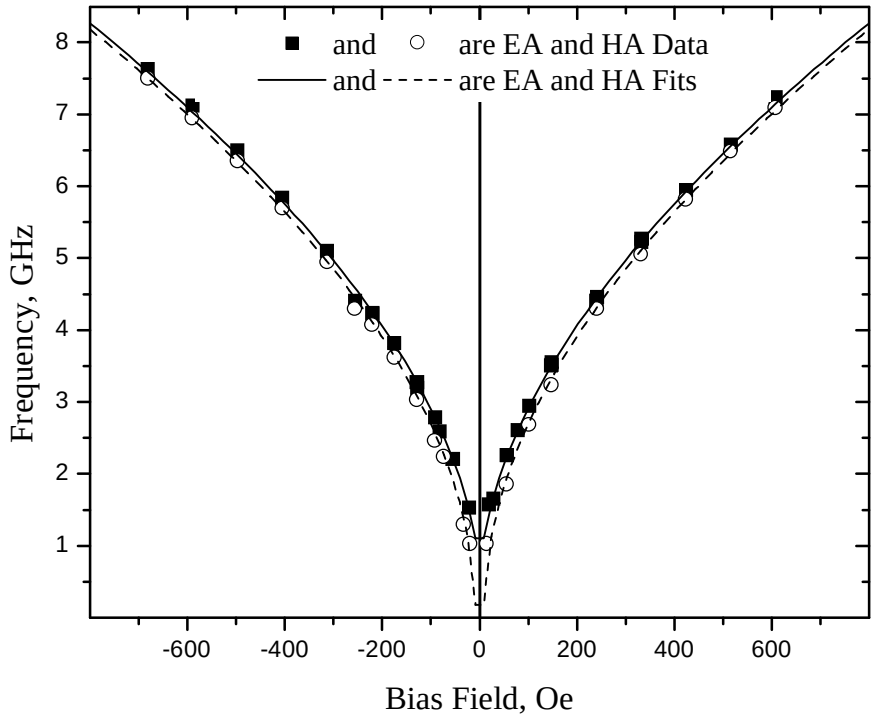

Figure 4.4 The dependence of the uniform mode frequency upon the bias field magnitude is presented for the 6000 nm element. The symbols are data points and the lines are least square fits to the macrospin model equations, as described in the text.

the peaks to a Gaussian function. In some cases, an additional Gaussian peak was used in order to represent a background due to the pulsed field profile. The extracted frequencies are plotted in Figure 4.4 as a function of the bias field magnitude, and in Figure 4.5 as a function of the bias field direction.

The experimental points were fitted to equations (3.2.16),(3.2.9)-(3.2.14) of the macrospin model described in detail in the previous chapter. In the fitting, a quasialignment condition was assumed, i.e. the magnetisation was assumed to be parallel to the bias magnetic field. The Landé g-factor and the saturation magnetisation were fixed at values of 2.1 and 930 emu, respectively. From the fitting, it was determined that the uniaxial and surface anisotropy parameters had values of 4140±330 erg/cm^3 and 0.1561±0.022 erg/cm^2, which are 19 % lower and 29 % higher

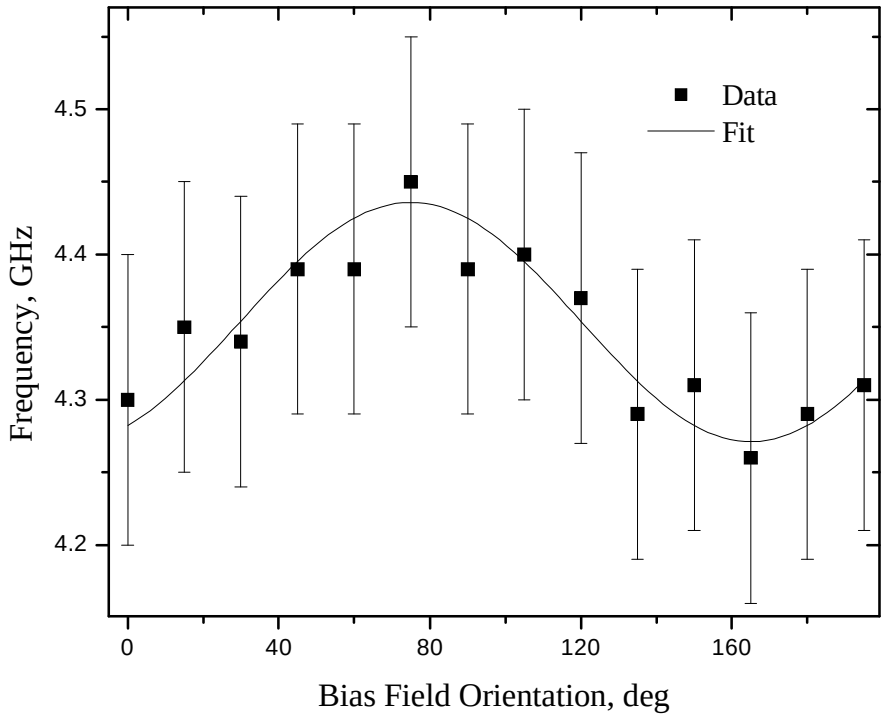

Figure 4.5 The dependence of the uniform mode frequency upon the bias field orientation is presented for the 6000 nm element. The symbols represent data points and the lines are least square fits to the macrospin model equations, as described in the text.

respectively than the values obtained from the static magnetometry measurements. The sample easy axis was canted by about 10° from the expected direction parallel to the tracks of the transmission line structure. No sign of a fourfold anisotropy was found. In fitting the angular dependence of the mode frequency, the assumed value of the static magnetic field was decreased by 2 Oe, that is, by less than 1%, which is well within the field calibration error.

4.3.2 Element Arrays

The measured Kerr rotation signals and their Fourier spectra are presented in Figure 4.6, Figure 4.7, Figure 4.8, Figure 4.9, and Figure 4.10 for arrays with 630, 425,

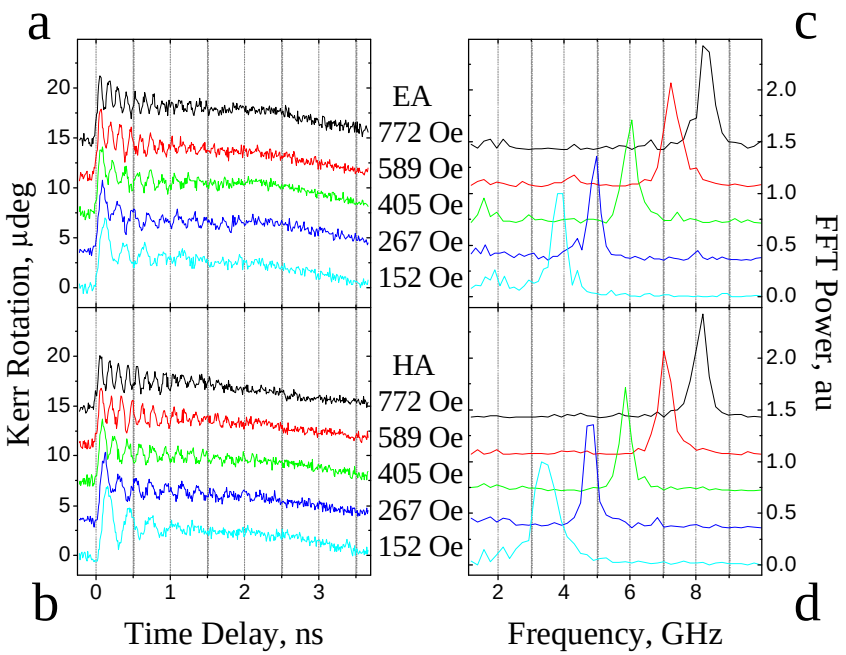

Figure 4.6 Typical time resolved Kerr rotation signals obtained from the 630 nm element array are presented in panels (a) and (b) for different values of the bias field applied parallel to the expected easy (EA) and hard (HA) anisotropy axes, respectively. The Fourier spectra of the corresponding signals in panels (a) and (b) are presented in panels (c) and (d), respectively.

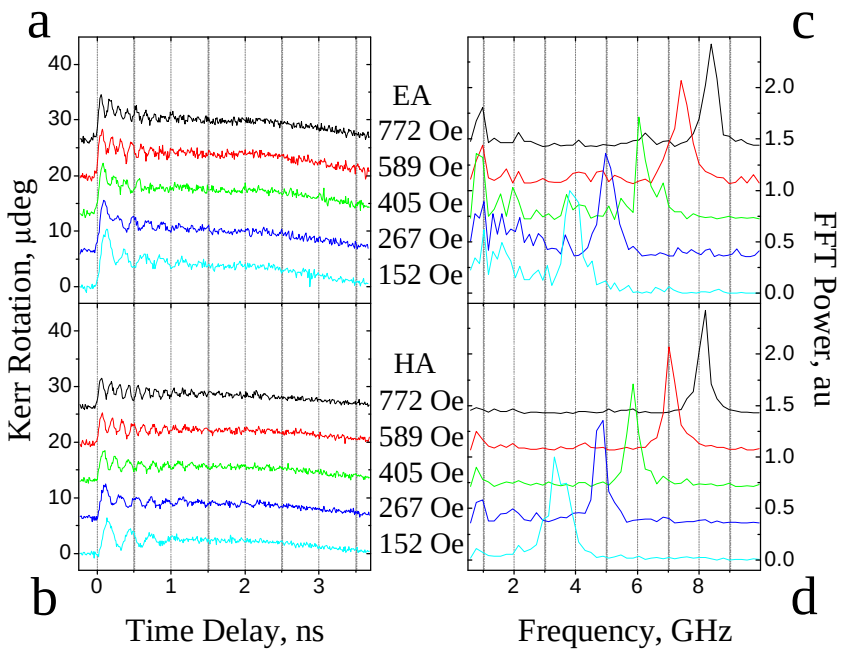

Figure 4.7 The same quantities are plotted as in Figure 4.6, but for the 425 nm element array.

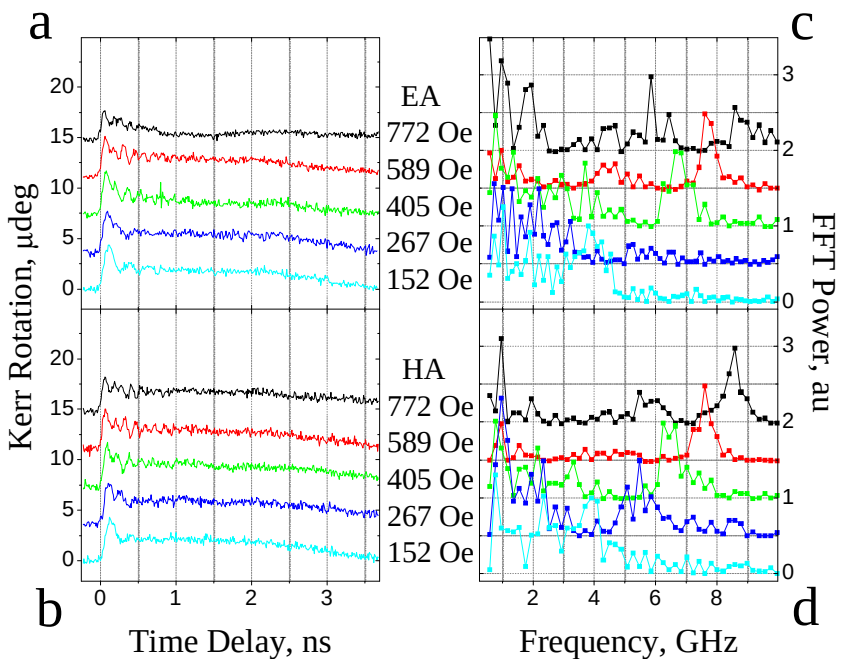

Figure 4.8 The same quantities are plotted as in Figure 4.6, but for the 220 nm element array.

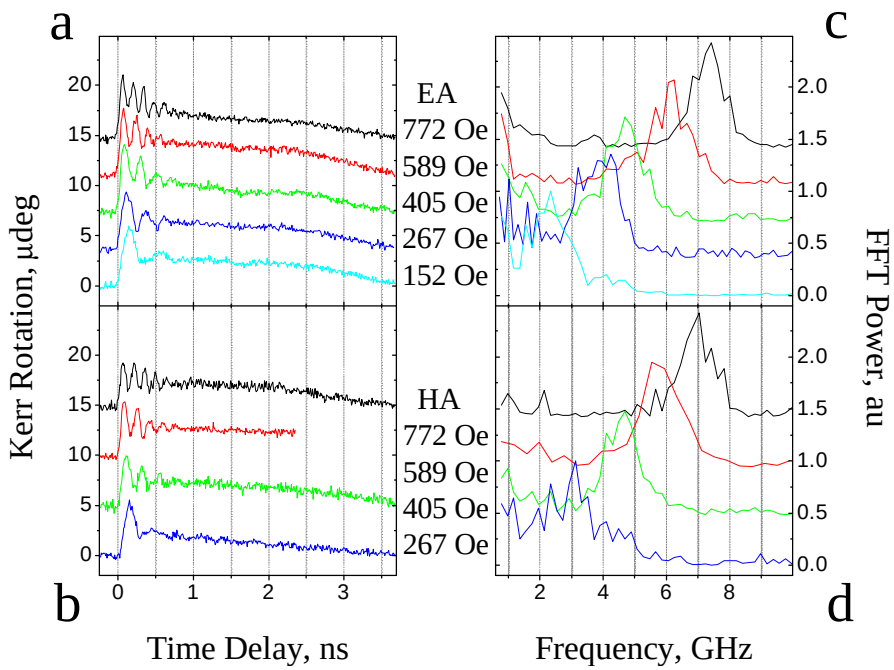

Figure 4.9 The same quantities are plotted as in Figure 4.6, but for the 120 nm element array.

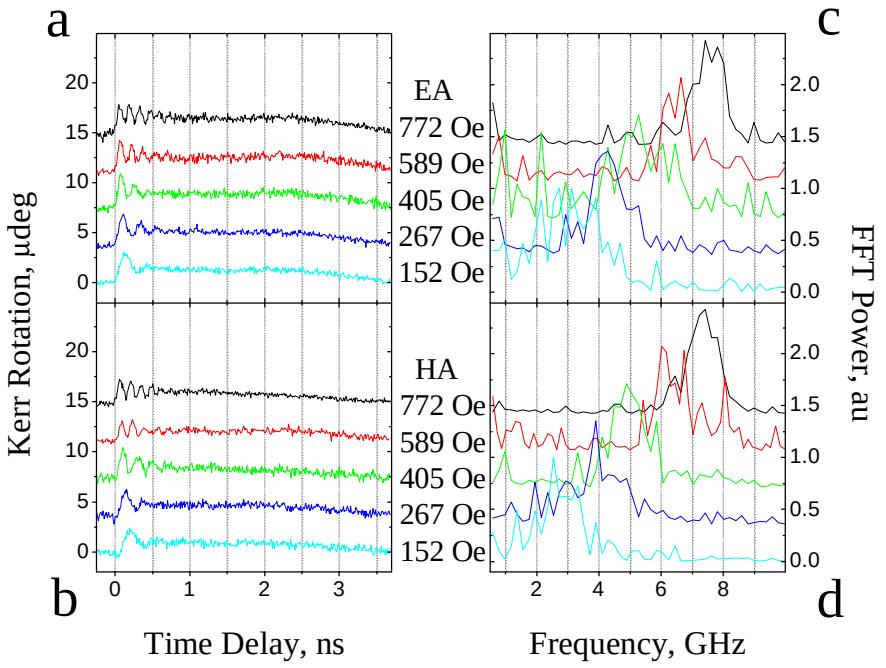

Figure 4.10 The same quantities are plotted as in Figure 4.6, but for the 64 nm element array.

220, 120, and 64 nm size elements, respectively. The samples showed a smaller response so that much longer time was required to acquire a signal of reasonable quality. Hence, only measurements for two directions and five different magnitudes of the bias field were performed.

The 630 and 425 nm element arrays showed a single mode. The time resolved signals from the array of 220 nm elements exhibit beating, and so their Fourier spectra contained an additional mode of a low frequency. The mode is best seen in the signals for bias fields of 772 and 589 Oe, while it is obscured by the peaks due to the field profile at smaller magnitudes of the bias field. The 120 and 64 nm element arrays again showed a single mode at a frequency that was lower than that of the 630 and 425 nm

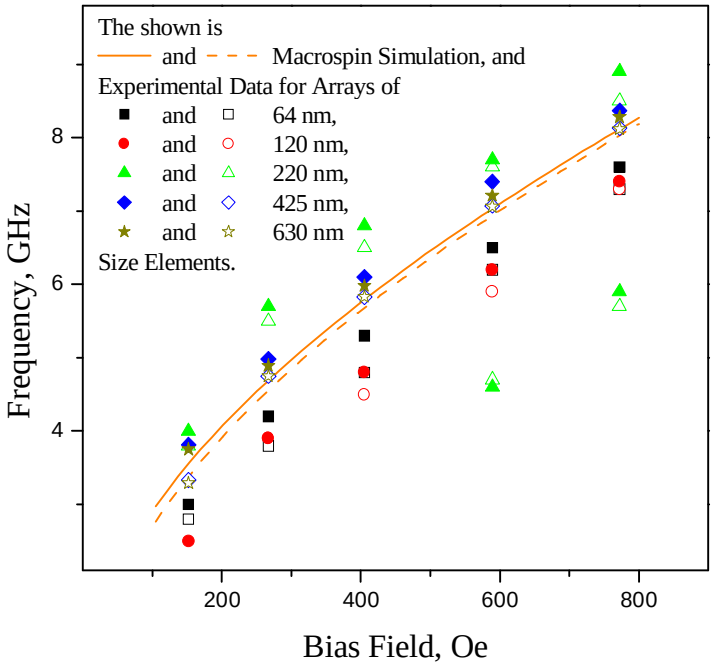

Figure 4.11 The mode frequencies extracted from the Fourier spectra shown in Figures 4.6-4.10 are plotted as a function of the bias field magnitude. The lines are the macrospin model fits of the 6 µm element frequencies from Figure 4.4. The solid symbols and solid line correspond to the bias field parallel to the EA direction. The open symbols and the dashed line correspond to the bias field parallel to the HA direction.

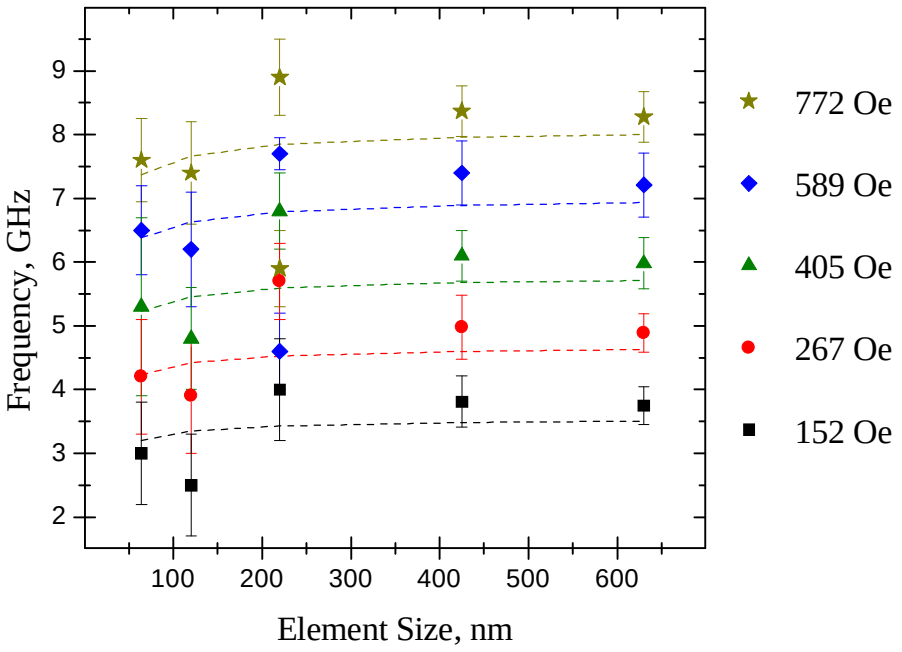

Figure 4.12 The mode frequencies extracted from the Fourier spectra shown in Figures 4.6-4.10 are plotted as a function of the element size for different values of the bias field. The field is parallel to the EA direction. The symbols represent data points. The dashed lines represent simulated frequencies that were obtained with OOMMF under assumption that the elements were uniformly magnetised.

element arrays, and in between the frequencies of the two modes observed in the 220 nm element array. Figure 4.11 presents the frequencies of the observed modes together with curves obtained by fitting the frequencies of the 6 μm element to the macrospin model equations. One can see that the deviation from the latter curves is relatively small for the 425 and 630 nm element arrays and much greater for the 220, 110, and 64 nm element arrays.

The dependence of the mode frequencies upon the element size is presented in Figure 4.12 for the field applied parallel to the EA direction. One can see that the dependence is complicated and non-monotonic. For the 630 and 425 nm element arrays, the frequency increases as the element size decreases. In the 120 and 64 nm

element arrays, the same trend is observed, but the frequencies are reduced in comparison with those in the 630 and 425 nm element arrays. In the 220 nm element array, the frequencies for field values of 152, 267, and 405 Oe and the higher frequencies for field values of 589 and 772 Oe follow the trend of the 630 and 425 nm element arrays, while the lower modes for the latter field values follow the trend of the 120 and 64 nm element arrays. Hence, two branches in the frequency dependence upon the element size, with a crossover from one to the other at the element size of 220 nm, are observed in the experiment. In the following, we will refer to them as to the "lower" and "higher" branch. For comparison, Figure 4.12 shows also the precession frequency that was calculated with OOMMF for uniformly magnetised elements, using formulae from Ref. 115, as described in the next section. One can see that, although the experimental data follow the calculated frequencies "on average", the detailed dependence on the element size is not properly described. Hence, the origin of the observed behaviour lies in the inherent nonuniformity of the magnetisation distribution in the elements, which have non-ellipsoidal shape, and so no attempts were made to analyse the frequencies with the macrospin model formulae derived in the previous chapter.

However, for the separation of the elements in the present arrays, the field of interaction between nearest neighbour elements was of the order of tens of oersteds. Hence, another possibility could be that we observed the collective behaviour of the elements in the arrays. This idea was also supported by the fact that the line width of the Fourier peaks was noticeably greater in the 120 and 64 nm arrays in comparison with the 630 and 425 nm element arrays, although this could also be due to the greater imperfection of the smaller elements. .

In order to identify which of the above effects was responsible for the observation, we undertook numerical micromagnetic simulations of the magnetisation

dynamics within the single elements from which the arrays were composed. The simulation of magnetisation dynamics in the element arrays was not performed because of the restrictions imposed by the computation time, which was at the limit of the capabilities of the available facilities even for the single element simulations.

4.4 Micromagnetic Simulations

4.4.1 Details of Simulations

Using the Object Oriented Micromagnetic Framework (OOMMF)[62], we performed simulations of magnetisation dynamics in single square elements with dimensions equal to those in the measured element arrays. The values of the magnetic parameters and the direction of the easy uniaxial anisotropy axis were assumed to be the same as those obtained from fitting the frequencies measured for the 6 μm element. We assumed a value of 13 x 10^{-12} erg/cm for the exchange stiffness constant, corresponding to bulk permalloy. The surface anisotropy was included as a uniaxial volume anisotropy with the easy axis perpendicular to the element plane. The static field was always parallel to an edge of the element, as shown in Figure 4.13, and had values of 152, 267, 405, 589, and 772 Oe that were equal to those used in the measurements.

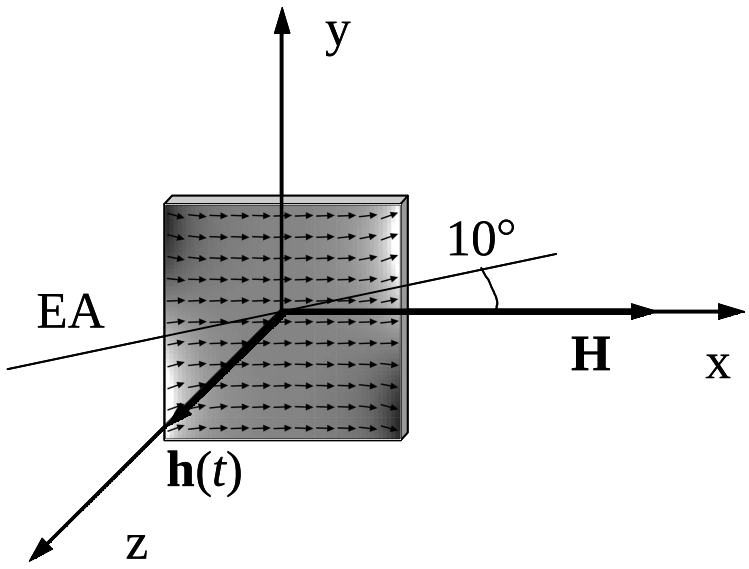

Figure 4.13 The geometry for the simulations is shown.

Each element was divided into cubic cells with height equal to the element thickness, while the lateral cell size was varied to achieve the best compromise between computational time and consistency of the results. In the simulations presented in this chapter, a cell size of 5, 4, 3, and 2 nm was used for 630 and 425, 220, 120, and 64 nm elements, respectively. With these cell sizes, the simulation of an 8 ns signal required up to 20 hours of computation time on a Pentium 4 computer with a 2.8 GHz processor and 1 GByte of memory. This chapter contains the results of more than 100 dynamic simulations.

First, the static state was prepared for each element and for each value of the static field. The sample magnetisation was allowed to relax in real time from a state with uniform magnetisation parallel to the x-axis to equilibrium at a static field of 3 kOe, and then to an equilibrium at the required value of the bias field. This procedure is in fact similar to that used in the experiment. In this stage, the first (precessional) term in the right hand side of the Landau-Lifshitz equation was dropped, which corresponds to the steepest descent method of energy minimisation[62]. The static configurations of the magnetisation that were obtained are shown in Figure 4.14. At static field values of 772, 589, and 405 Oe, the elements were found to be in the so-called "flower" state[116]. At a field value of 267 Oe, the 120, 220, and 425 nm elements switched to the so-called "S" state[116], while the 64 and 630 nm elements remained in the "flower" state. At a field value of 152 Oe, all elements were in the "S" state.

The same static state was then used as the initial configuration in two sets of dynamical simulations. In the first set, as in the experiment, an out-of-plane pulsed field with 40 ps rise time, 2 ns decay time, and magnitude of 15 Oe was applied to the sample. The spatial distribution of the magnetisation in the element and its value averaged over the element volume were then recorded every 5 ps during the first 8 ns

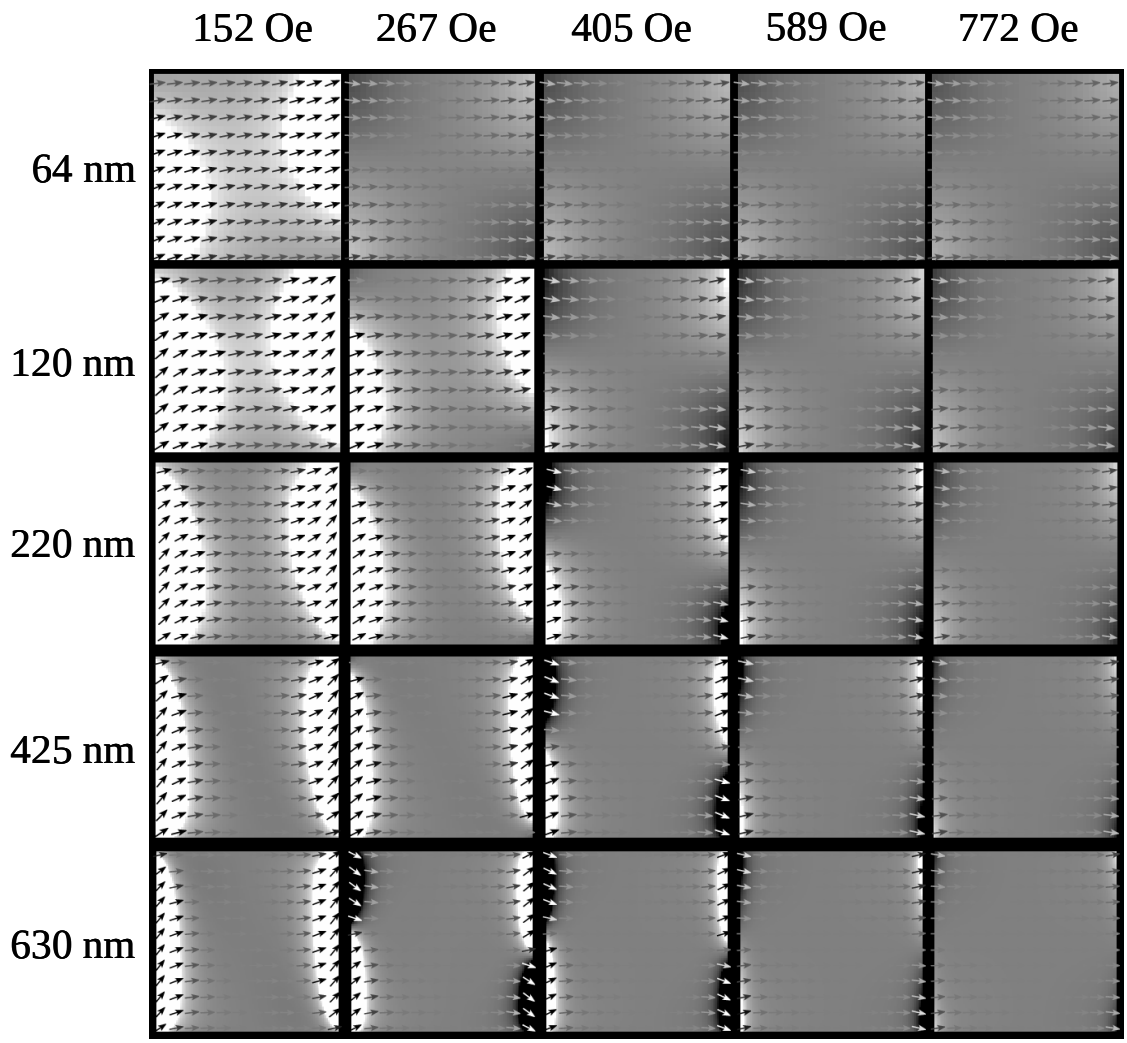

Figure 4.14 The static magnetisation distribution is shown on the same colour scale for different elements and different values of the static field. The colour scale represents the y-component of the magnetisation so that white and black colourings correspond to the magnetisation canting upwards and downwards in the plane of the Figure, respectively.

after the excitation. Figure 4.15 shows a typical simulated time resolved average magnetisation signal. The beating is a sign of several modes present in the signal. The x-component also contains a small time dependent contribution due to a small canting of the element magnetisation towards the easy axis direction. Figure 4.16 shows typical simulated images of the spatial distribution of the out-of-plane component of the

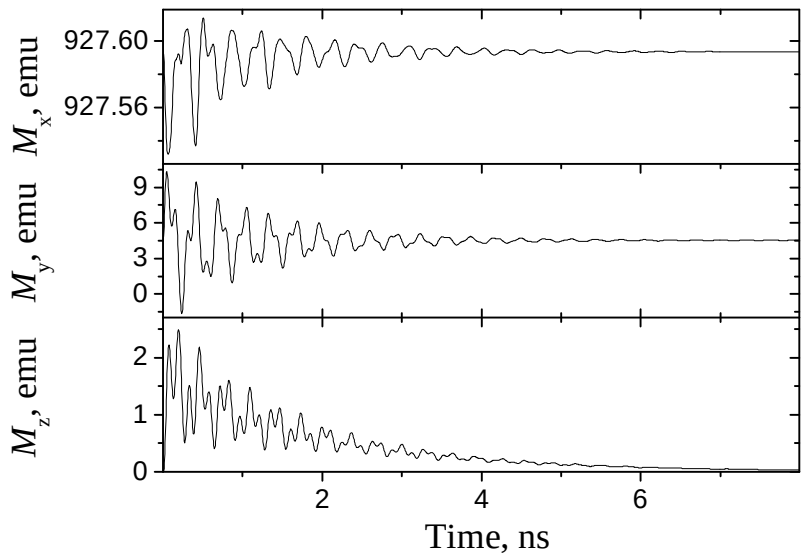

Figure 4.15 The three components of the average magnetisation of the 220 nm element are shown as functions of time after excitation by a pulsed magnetic field, while a static field of 405 Oe was applied along the x-axis.

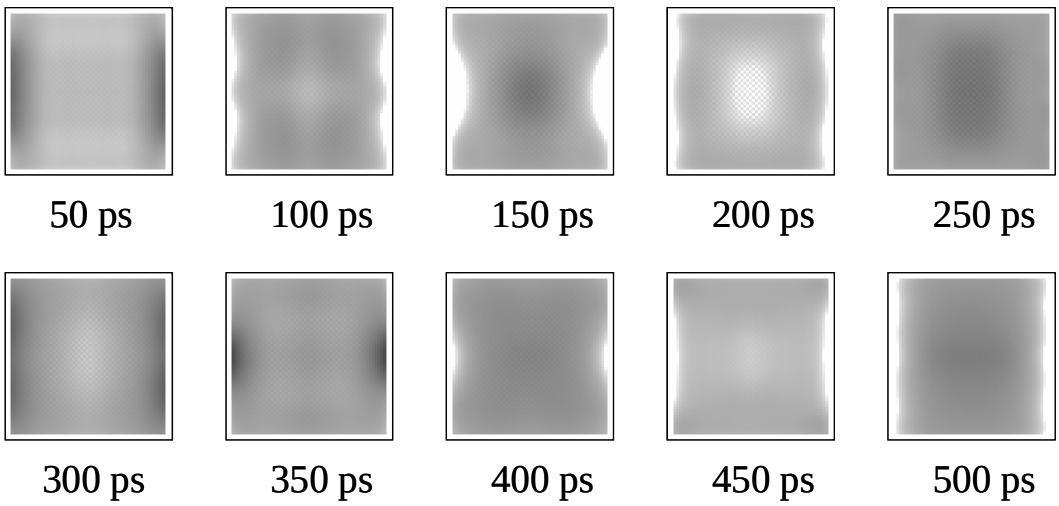

Figure 4.16 The simulated spatial distribution of the out-of-plane component of the 220 nm element magnetisation is shown for different time delays after excitation with the pulsed field. The white colouring corresponds to positive values.

element magnetisation at different time delays after excitation. The distribution is nonuniform. In particular, one can see that the central and edge regions of the element precess out of phase.

In order to study separately the spatial character of the different modes present in the signal, a second set of dynamical simulations was performed in which the magnetisation was stimulated by a harmonic field[117] with frequency equal to that of one of the modes observed in the first set of simulations. The harmonic field was applied perpendicular to the sample plane and had the same value of 15 Oe. The spatial distribution of the magnetisation in the element and its value averaged over the element volume were then recorded every 5 ps during the first 8 ns after the onset of the harmonic excitation. Figure 4.17 shows the typical simulated time resolved average magnetisation response to the harmonic field. The signal amplitude grows within the

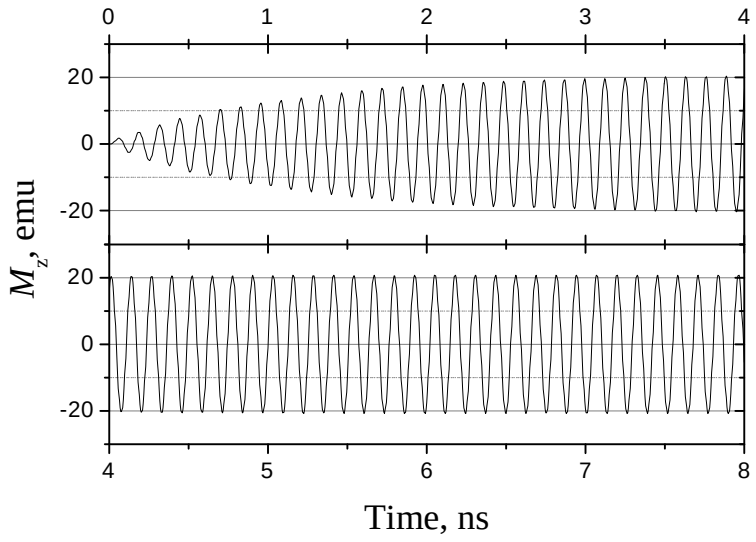

Figure 4.17 The z-component of the average magnetisation of the 220 nm element is shown as a function of time after the onset of a harmonic magnetic field with a frequency of 7.851 GHz, while a static field of 405 Oe was applied parallel to the x-axis. The top panel shows the first 4 ns of the signal, and the bottom panel shows the next 4 ns of the signal.

first 3-4 ns, and afterwards is constant. The images of the magnetisation distribution presented in the next section correspond to the last cycle of precession where nonuniformity due to modes with frequencies different from that of the stimulating harmonic field no longer contribute significantly to the image contrast.

4.4.2 Results

The Fourier spectra of the simulated response of the different elements to the pulsed magnetic field are compared in Figure 4.18. The Figure shows only spectra for the z-component of the magnetisation averaged over the element volume, which

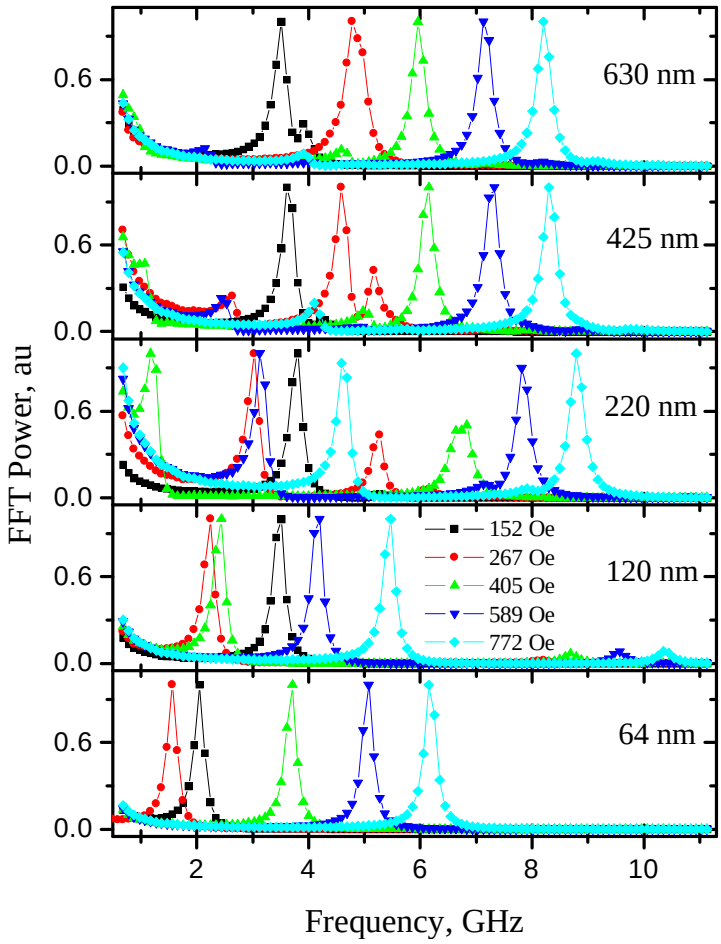

Figure 4.18 The Fourier spectra of the z-component of the dynamic average magnetisation of the different elements are shown for different values of the static field.

corresponds to what was measured in the experiment. The peak value in each spectrum was normalised to unity.

One can see that the dependence of the simulated spectra upon the element size is in good qualitative agreement with the measurements. In particular, the crossover from the higher to the lower frequency branch is seen to occur at an element size of 220 nm. Although several modes are generally present in the spectra, their relative amplitudes are different. However, in the 220 nm element, the higher and lower branch modes have similar amplitudes. In contrast, a mode from either the higher or lower branch is dominant in the spectra obtained from the larger and smaller elements, respectively. The 64 nm element showed virtually single mode response, with the other modes having more than then three orders of magnitude smaller peak amplitude. It was found that the modes with maximum amplitude were not always those with frequency closest to the mode observed in the experiment. Therefore, in order to correlate a particular peak in the simulation with an experimentally observed mode, some additional consideration was required. Simulations of the spatial distribution of the dynamic magnetisation in response to a harmonic field were performed at frequencies corresponding to the peaks in the Fourier spectra shown in Figure 4.18.

The simulated spatial character of the different modes is shown in Figure 4.19 for different values of the static field. The grey scale contrast in the Figure represents the spatial distribution of the z-component of the dynamic magnetisation. Each image was scaled so that points with a signal magnitude greater than 75% of the maximum are shown as white and black for positive and negative values, respectively. Each image corresponds to a time delay at which the average magnetisation of the element was at a maximum during the last cycle of precession within an 8 ns time scan such as that shown in Figure 4.17. For each static field value, two modes corresponding to the higher and lower frequency branches for each element are presented in the top and

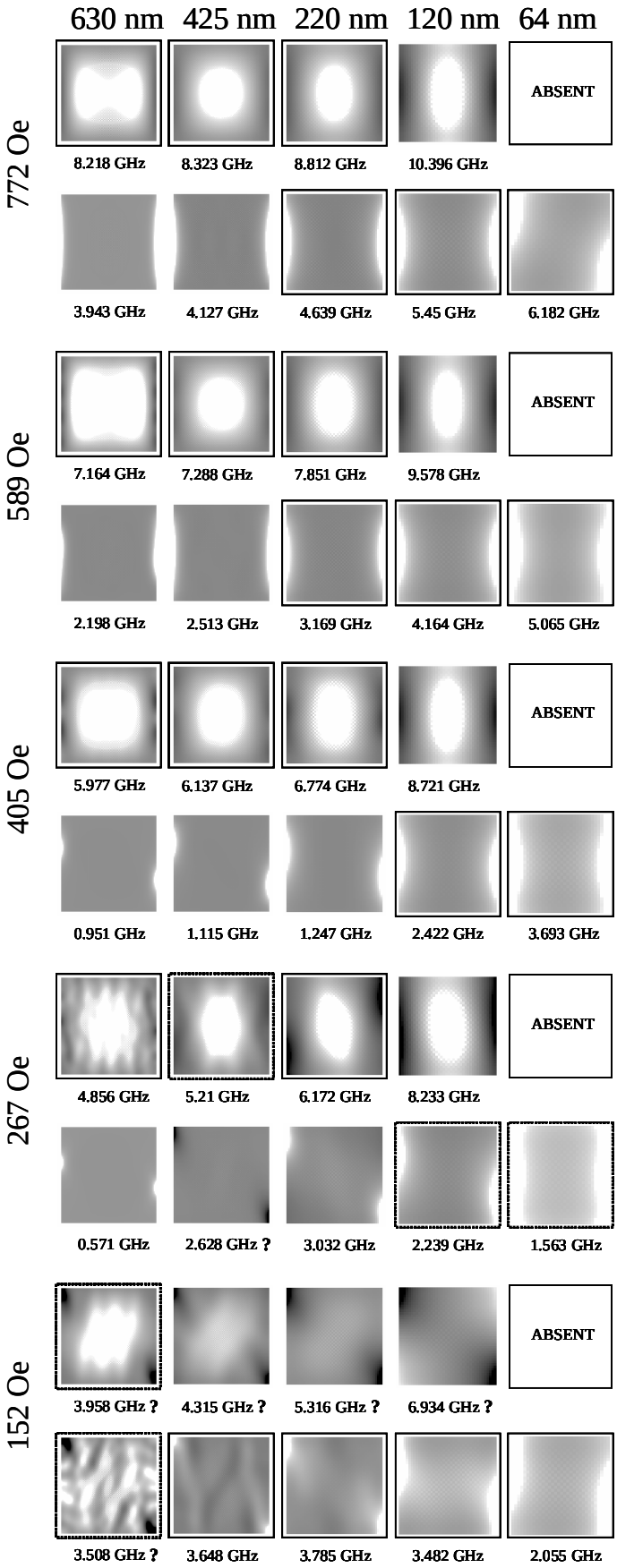

Figure 4.19 The simulated spatial distribution of the z-component of the dynamic magnetisation is presented, as explained in the text.

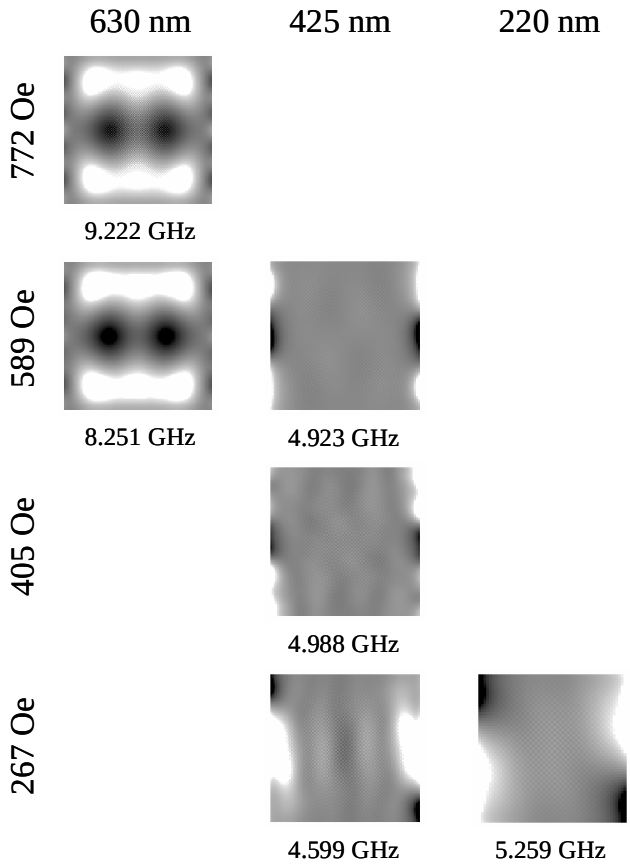

Figure 4.20 The simulated spatial distribution of the z-component of the dynamic magnetisation is presented for the modes that were not observed in the experiment.

bottom row, respectively. The images corresponding to the modes observed in the experiment have been placed within frames. Figure 4.20 shows the simulated spatial character of additional modes seen in Figure 4.18 that were not observed in the experiment.

For the four larger element sizes, we also performed simulations of the response to a pulsed field, using half the cell size for a time scan of shorter duration. It was found that the frequencies in the two sets of simulations with different cell sizes agreed to better than 1 %. The results for the 64 nm element showed the strongest dependence upon the dimensions of the cell, with changes occurring down to a size of 2 nm, as

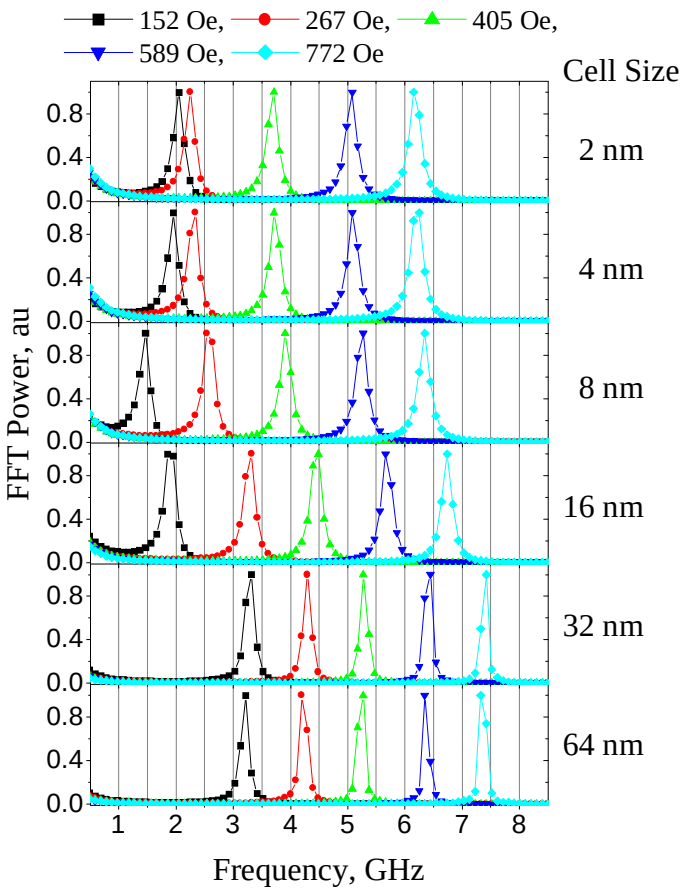

Figure 4.21 The Fourier spectra of the z-component of the simulated dynamic average magnetisation of the 64 nm element are shown for different values of the static field and different cell sizes.

shown in Figure 4.21. For this element, simulations with a cell size of 1 nm were unacceptably slow. Hence, it was decided to use the smallest affordable cell size of 2 nm, since the difference between the frequencies simulated with 2 and 4 nm cells was already small (less than 5 %), although still significant. Overall, the results of the simulations did not seem to be significantly affected by the finite cell size.

The frequencies obtained by setting the cell size equal to the size of the element, such as shown in the bottom panel of Figure 4.21, correspond to a uniform distribution of the magnetisation in the element. The OOMMF implements analytical formulae derived in Ref. 115 for the average demagnetising tensor components of a uniformly

magnetised prism. Hence, the calculated frequencies correspond to the eigenmodes of the macrospin model corrected to account for the demagnetising field. We performed the calculations for each element. The results were also plotted as dashed lines in Figure 4.12.

4.5 Discussion

Figure 4.22 summarises the results of the experiment and the simulations in the frequency domain. While a good qualitative agreement between the experiment and simulations was achieved, the quantitative agreement is less good. The frequencies calculated for the higher branch agree well with the measurements for the four higher field values. The modes observed in the 220, 425, and 630 nm elements for the field value of 152 Oe should be attributed to the lower branch mode which, for this field value, has the greater amplitude and also a frequency that is closer to that observed in the experiment. The lower branch modes observed in the 220 nm element at field

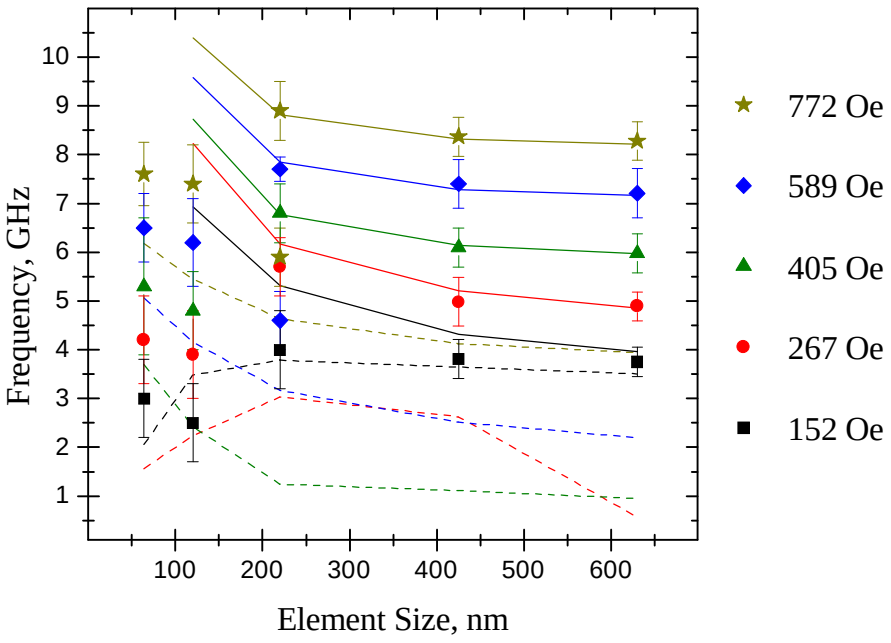

Figure 4.22 The mode frequencies observed in the experiment and simulated with OOMMF are plotted as a function of the element size for different values of the bias field. The static field was parallel to the EA direction. The symbols represent data points, while the solid and dashed lines are the simulated frequencies of the higher and lower modes from the Fourier spectra shown in Figure 4.18, respectively.

values of 589 and 772 Oe have frequencies that lie much higher than the simulated frequencies, as do the frequencies observed in the 64 and 120 nm elements. In the latter elements, a seemingly better agreement for the field of 152 Oe may be misleading, since the simulated frequency for the 64 nm element is lower than that for the 120 nm element, and is opposite to what was observed in the experiment.

The spatial character of the modes can be identified from the results of the dynamic simulations with a harmonic field excitation. Figure 4.19 clearly shows that

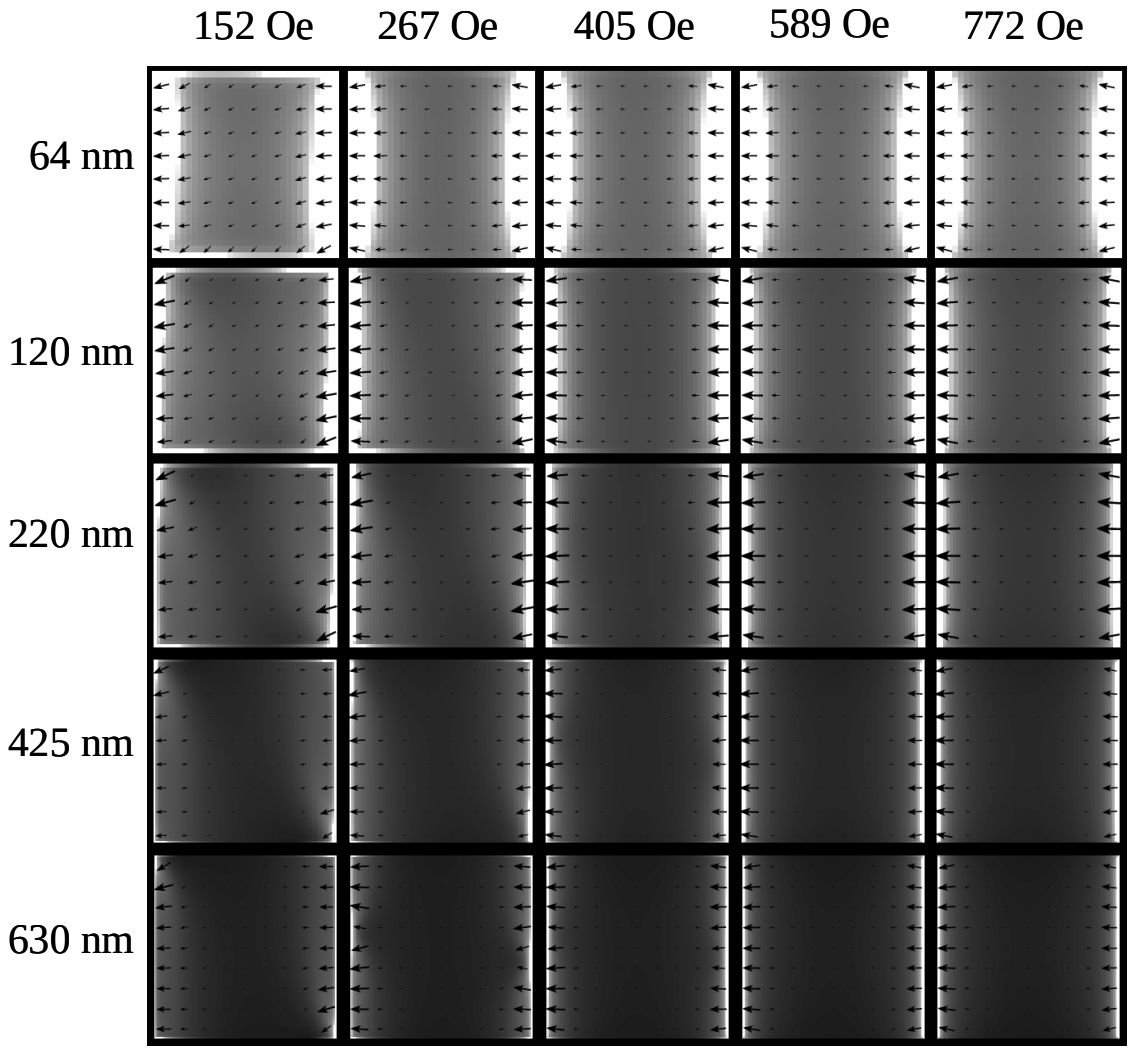

Figure 4.23 The spatial distribution of the demagnetising field in different elements is shown at the same colour scale for different values of the static field. The colour scale represents the magnitude of the demagnetising field.

the magnetisation dynamics occur at the centre and near the edges perpendicular to the static field, for the higher and lower branch modes, respectively. This is explained by the distribution of the static demagnetising field within the elements, that is shown in Figure 4.23. The demagnetising field is enhanced near the edges of the elements. Hence, the total effective field, which is approximately equal to the difference of the applied and demagnetising fields, is lower in the demagnetised regions than in the centre, and so the magnetisation precesses at different frequencies in these two regions, giving rise to the two observed modes. From hereon we refer to the higher and lower frequency modes as "centre" and "edge" modes, respectively.

The observed crossover from the centre to the edge branch can also be explained by the effect of the demagnetisation. From Figure 4.23, one can see that the relative area of the demagnetised region, and hence the relative contribution of the edge mode, increases with reduction of the element size. The trend is opposite for the centre mode. The reduction of the total effective field in the demagnetised regions also favours the observation of the edge modes, since the magnetisation precession has generally greater amplitude for a lower field.

The localised nature of the magnetisation dynamics for the edge mode suggests also that the discrepancy observed between the simulated and measured frequency values is due to the exchange interaction. This idea is supported by the better agreement obtained for the larger elements and the centre modes. Indeed, in the simulations, we assumed a value for the exchange stiffness corresponding to bulk permalloy. Cobalt-iron alloys are known to have a larger exchange parameter[118]. Hence, we performed a few simulations of the response of the 220 nm element to a pulsed field, in which the exchange stiffness was increased by 50% (not shown). It was found that the frequencies of the centre and edge modes increased by about 4% and 21%, respectively. While this confirms our suggestion that the exchange is important, a systematic tuning of the

exchange parameter, and probably other magnetic parameters, was not possible because of the required computation time.

The experimentally observed frequencies have an upward curvature as a function of the element size and monotonically decrease with decreasing static field. These features are reproduced by the simulations for the field values of 772, 589, and 405 Oe. However, the simulated frequencies for the static field values of 267 and 152 Oe have a downward curvature. This is correlated with a change of the static magnetic configuration from the "flower" to "S" type at the field value of 152 Oe for the 64 and 630 nm elements, and 267 Oe for the 120, 220, and 425 nm elements. As shown in Figure 4.23, this transition changes the configuration of the demagnetising field and makes it asymmetric. A larger area demagnetised region is created near the top left and bottom right corners. The spatial character of the magnetisation dynamics is transformed in the same manner, so that the dynamic magnetisation becomes localised closer to, or virtually within the corners of the elements, as seen in Figure 4.19. The exchange interaction pushes the frequency up, as the localisation is increased. One can see from Figure 4.22 that this increase may even overcome the frequency decrease due to the decrease of the static field. In the experiment, the upward curvature suggests that the magnetisation in the 64 and 120 nm elements did not switch to the "S" type static configuration. However, the agreement of the simulations with experiment at a static field of 152 Oe for the 220 nm, 425 Oe, and 630 nm elements leads us to think that the switching between the two configurations occurred at this field value. This might be explained by a larger coercive force in the smaller sized elements[35,52].

While it was assumed in the simulations that the elements had a square shape, Figure 4.1 shows that the 120 and 64 nm elements are rounded, especially in the case of the latter element. This may provide a simpler explanation of the observed discrepancy between the experimental and simulated frequencies for these elements. The magnetic

properties of smaller elements are more affected by the presence of different sorts of imperfections. For example, defects may act as pinning centres and change the area of the region in which the observed modes are localised. Their frequency will hence be strongly modified by the exchange interaction. The defects may also significantly affect the field at which switching occurs between the two configurations. As we have seen, the latter are characterised by very different frequencies. The random nature of defects will cause different elements in an array to precess at different frequencies, and so the observed frequency peak will be broadened, as was indeed observed in the 64 and 120 nm element arrays.

Finally, we want to emphasise the importance of the nonuniform magnetisation dynamics observed in the 64 nm element. Since readout sensors in modern computer hard disk drives are of similar size, the nonuniformity may significantly contribute to the readout process.

4.6 Summary

In this chapter, the magnetisation dynamics of small magnetic elements and element arrays were investigated by means of time resolved optical measurements and micromagnetic simulations. While the mode frequencies observed for the 6 μm element could be described by a macrospin model, the frequencies of the modes observed for arrays of smaller elements showed a more complicated behaviour. Most of the observed modes could be identified as falling on two branches characterised by different frequencies. The micromagnetic simulations showed that the magnetisation dynamics are nonuniform, and so the frequencies and relative amplitudes of the modes from the two branches are determined by the interplay between the exchange and demagnetising fields. In particular, it was found that the dynamics are nonuniform even in the 64 nm element, where the dominant mode is confined by the demagnetising field within the edge regions of the element.

Chapter 5. Measurement of Hot Electron Momentum Relaxation Times and Third Order Nonlinear Susceptibility Tensor Components in Metals by Femtosecond Ellipsometry

5.1 Introduction

Optical pump-probe measurements provide valuable information about a variety of technologically important phenomena such as electron thermalisation[72], angular and linear momentum relaxation, exchange of energy between electron and phonon subsystems[7], optical generation of magnons[25,26] and phonons[9,11], and ultrafast demagnetization[10]. The timescales for the linear and angular momentum dynamics of electrons and holes are of particular importance for transport phenomena, where the carrier energy, direction of motion and spin polarization play a significant role[119]. The corresponding spin, momentum and energy scattering times are determined by the interactions between electrons, holes and phonons, and by scattering from defects, and are expected to be of the order of a few femtoseconds[120]. Hence, there is a need for time resolved optical experiments that have sufficient time resolution to resolve these processes.

The construction of ultrafast optically controlled switches, modulators and regenerators, based upon non-linear optical materials, is of great interest for optical communication systems. Although metal-dielectric[121,122] and organic-dielectric[123] nanocomposite, semiconductor[124] and organic[125] non-linear materials may possess larger third-order optical nonlinearities, the non-linear response of pure metals is faster, while still being of significant magnitude[8,126-130]. Although a phenomenological theory of the nonlinearity already exists in the continuous wave (cw) approximation[75],

relatively little has been done towards developing a microscopic understanding of the time scales of the underlying microscopic processes. This is partly due to a shortage of experimental studies of adequate (femtosecond) temporal resolution. The optical pump-probe technique can fill this gap and is able to distinguish between the real (refractive) and imaginary (absorptive) parts of the third order nonlinear tensor $\chi^{(3)}$, which is important for the implementation of all-optical devices[75].

In this chapter, a first comparative study of the femtosecond non-linear optical response of a series of noble and transition metal thin films performed under the same experimental conditions is described. An elliptically polarized pump beam was used so that the SIFE and the SOKE were present simultaneously in the time resolved signal. This allowed a small yet significant time delay between these effects to be observed within signals of bipolar shape. The zero time delay position of the polarisation signal was defined with respect to the onset of the transient reflectivity signal which was simultaneously measured. Since the latter is expected to be independent of the pump polarisation, this also allowed the relative timing of the transient rotation and ellipticity signals to be compared for a particular effect (the SIFE or the SOKE). In some cases, the individual SIFE and SOKE curves had bipolar shapes.

The SIFE and SOKE contributions were separated using the technique developed in Ref. 76, and their maximum values were used to extract the non-vanishing components of the third-order optical susceptibility tensor $\chi^{(3)}$. Both the signal maximum values and the values of the $\chi^{(3)}$ components were found to depend systematically upon the position of the metal within the periodic table. The SIFE-SOKE and transient rotation-ellipticity time shifts, and the shapes of individual signals were successfully reproduced by fitting the SIFE and SOKE components to a simple theory developed in the relaxation time approximation. This allowed relaxation times to

be extracted for the non-linear polarisation, which were then interpreted in terms of scattering of the linear and angular momentum of hot electrons.

Finally, the reliability of the technique was tested. For this purpose, the measurements of the pure SOKE were carried out using a linearly polarised pump. Then, the reliability of the SIFE-SOKE separation technique was examined firstly by comparing the SIFE signal extracted from the elliptical pump measurements with the pure SIFE signal measured in experiments with a circularly polarised pump, and secondly by comparing the SOKE component extracted from the elliptical pump measurements with the pure SOKE signal measured in the experiment with a linearly polarised pump. The reliability of the fit is also discussed.

5.2 Experiment

5.2.1 Experimental Details

All measurements presented in this chapter were made using the single colour pump-probe apparatus, which was described in detail in chapter 2 and shown in Figure 2.1, with 90 fs transform limited pulses at a centre photon energy $\hbar\omega$=1.575±0.010 eV. The pump and probe pulses, with energies of 2 nJ and 0.04 nJ respectively, were directed onto the sample at angles of incidence of 7° and 27° respectively, focused to spots of 15 µm diameter, and then carefully overlapped. The probe was always p-polarized. The polarization of the pump was varied continuously from a p-polarized state either to a circularly polarized state, by rotating a quarter wave plate placed after a polarizer (geometry 1), or to a state in which the beam was linearly polarized at an angle to the plane of incidence, by rotating a polarizer situated after a quarter wave plate (geometry 2). Except for the Cu sample, the spot positions were not adjusted during measurements in either geometry, and measurements were completed within 1 or 2 days for each sample. The transient changes in the probe intensity and polarization state were recorded simultaneously. A quarter wave plate was placed in front of the bridge detector when the ellipticity η rather than the rotation θ was measured.

5.2.2 Samples

Measurements were performed upon noble and transition metal thin films, deposited by magnetron sputtering onto Si substrates. Since the $\chi^{(3)}$ tensor was expected to depend upon the detailed structure of the sample, X-ray reflectivity measurements were performed to determine the thickness, roughness and composition of the samples. The results of the X-ray measurements are summarized in Table 5.1.

	Film Thickness, nm	Film Roughness, nm	Oxide Layer Thickness, nm	Oxide Layer Roughness, nm
Cu	32.60±0.05	0.87±0.05	3.50±0.06	0.94±0.04
Ag	24.2±0.3	2.5±0.3	8.3±0.6	3.6±0.3
Au	28.10±0.03	1.30±0.01	n/a	n/a
Ni	53.6±0.4	0.90±0.15	1.2±0.4	0.46±0.03
Pd	61.8±0.7	2.50±0.26	1.0±0.7	0.500±0.010
Ti	25.6±0.4	0.26±0.05	1.14±0.20	0.320±0.010
Zr	42.50±0.07	0.47±0.06	2.50±0.07	0.446±0.010
Hf	76.60±0.14	1.04±0.08	4.80±0.08	0.872±0.020

Table 5.1 A summary of the structural parameters of the samples investigated in this chapter is given.

5.2.3 Measurements with Elliptical Pump

For each sample two sets of measurements were performed. In the first set, geometry 1 was used and time resolved rotation (or ellipticity) and reflectivity signals were simultaneously recorded for different orientations of the pump quarter wave plate. In this chapter, only the polarization response on time scales of a few hundreds of femtoseconds is discussed. The rise of a transient reflectivity response with much longer relaxation time was used here only to verify the zero time delay position. The reflectivity response of these and other samples is discussed in more detail in the following chapter.

The time resolved rotation and ellipticity signals acquired for different orientations of the pump quarter wave plate are shown in Figure 5.1 and Figure 5.2,

respectively, for different metals. As expected from equation (1.2.14), the signals consist of two components varying with periods of 90° and 180° with respect to the angle φ between the fast axis of the pump quarter wave plate and the plane of incidence. The SOKE contribution has period of 90° and becomes more pronounced as the pump polarisation ellipse axis becomes more asymmetric and is canted at a larger angle to the plane of the probe polarisation (e.g. for φ=±22.5°,±67.5°). The SOKE vanishes when the pump is either circularly polarised (e.g. for φ=±45°) or linearly polarised parallel to the probe polarisation (e.g. for φ=0°). The SIFE contribution has period of 180° and is most pronounced for circular pump polarisation (e.g. for φ=±45°), while vanishing for

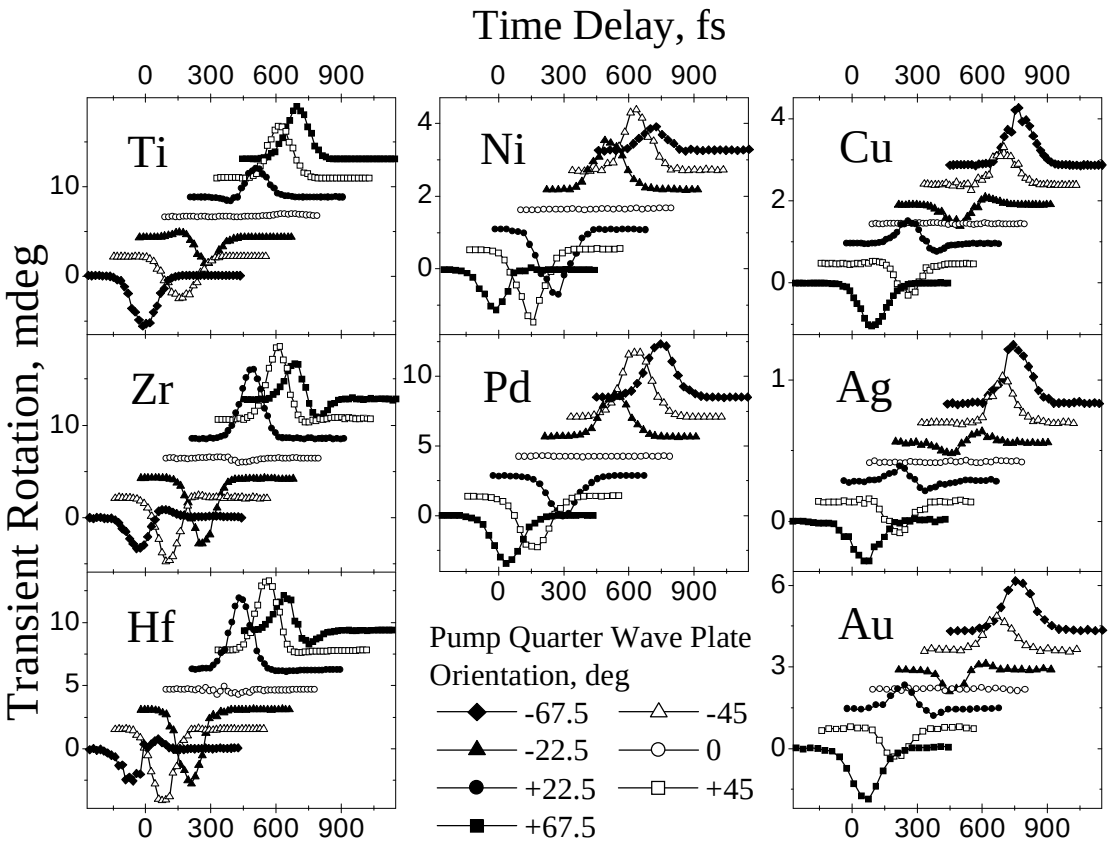

Figure 5.1 The transient rotation signals obtained in geometry 1 are presented. The signals obtained from different samples are arranged according to their position in the periodic table of elements.

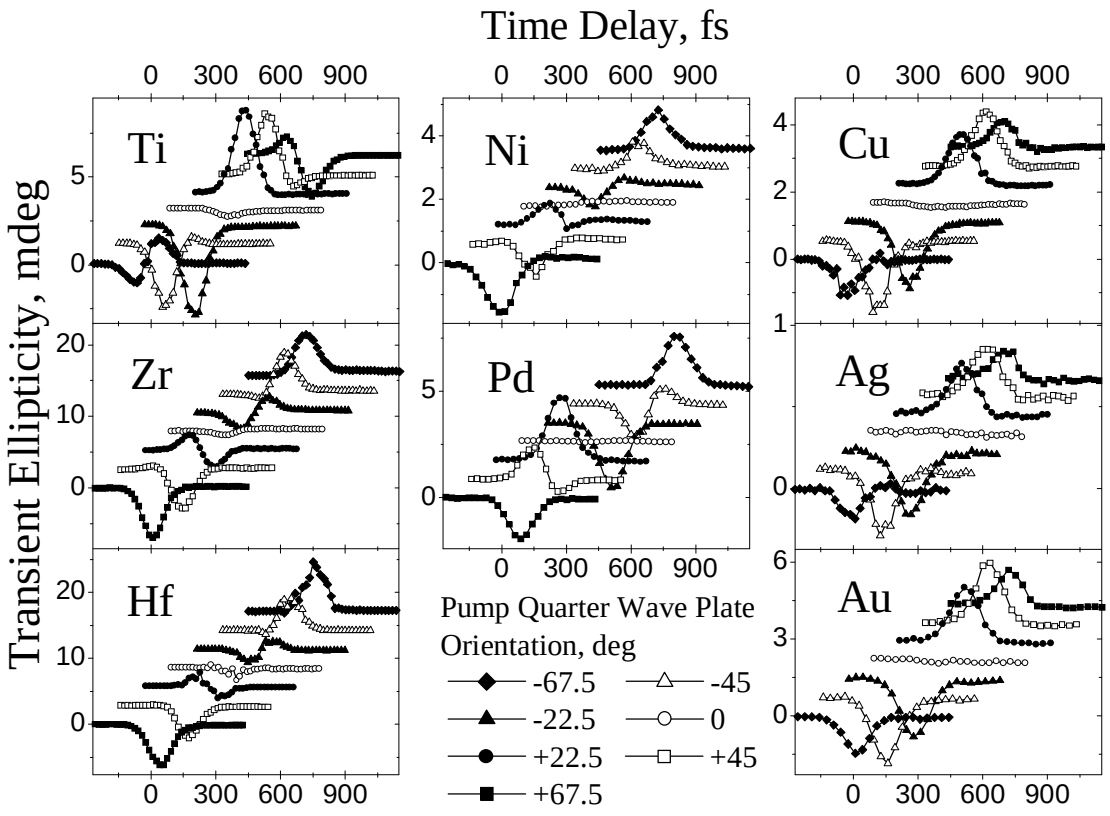

Figure 5.2 The transient ellipticity signals obtained in geometry 1 are presented. The signals obtained from different samples are arranged according to their position in the periodic table of elements.

linearly polarised pump (e.g. for φ=0°).

Equation (1.2.14) does not describe the temporal form of the signals. Let us make the common assumption that both SIFE and SOKE give rise to peaks with centre at the zero time delay position and with shape identical to the cross-correlation of the pump and probe intensity envelopes[127]. Then if both effects have finite amplitude, one would expect to see a signal with shape identical to that of the cross correlation curve for all values of φ, but with varying amplitude as the SIFE and SOKE either add or cancel. Instead, we observe that for some values of φ the signal has a bipolar temporal shape. This suggests that a small time delay exists between the centres of the SIFE and SOKE

peaks. In addition, the signals acquired with circular pump are themselves slightly bipolar. This may indicate the presence of two components shifted in time within the pure SIFE signals.

The transient rotation and ellipticity signals are similar in shape inside the group of noble metals. The Ni and Pd samples have transient rotation signals of similar shape, while their transient ellipticity signals are different. In the group of hcp metals, the Zr and Hf signal shapes are similar both in rotation and ellipticity, while the Ti time resolved signal is somewhat different.

5.2.4 Measurements with Linear Pump

In the second set of measurements, geometry 2 was used and time resolved rotation (ellipticity) and reflectivity signals were recorded for different orientations of the pump polarizer. The signal-to-noise ratio in this set of measurements was somewhat worse than that in the measurements performed with an elliptically polarised pump, because the pump intensity in this geometry was only half of that in geometry 1. In particular, it was not possible to acquire a signal of acceptable quality from the Ag film. The measured rotation and ellipticity signals are shown in Figure 5.3 and Figure 5.4, respectively, for the different metals.

As expected from equation (1.2.15), the signals consist of only a pure SOKE component with magnitude varying with period of 180° with respect to the angle ψ between the transmission axis of the pump polarizer and the plane of incidence. The maximum peak heights were observed when the pump polarisation was oriented at $\psi=\pm 45°$ to that of the probe polarisation. The transient rotation and ellipticity signals are similar in shape for Cu and Au. The Ni and Pd samples have transient ellipticity signals of similar shape, while their transient rotation signals are now different. As far as the main peak is concerned, all three hcp metal samples showed a signal of similar shape both in rotation and ellipticity, although some signals were slightly bipolar.

Together with the clear bipolarity of the Pd transient rotation signal, this indicates the presence of two contributions to the pure SOKE signal that are shifted in time.

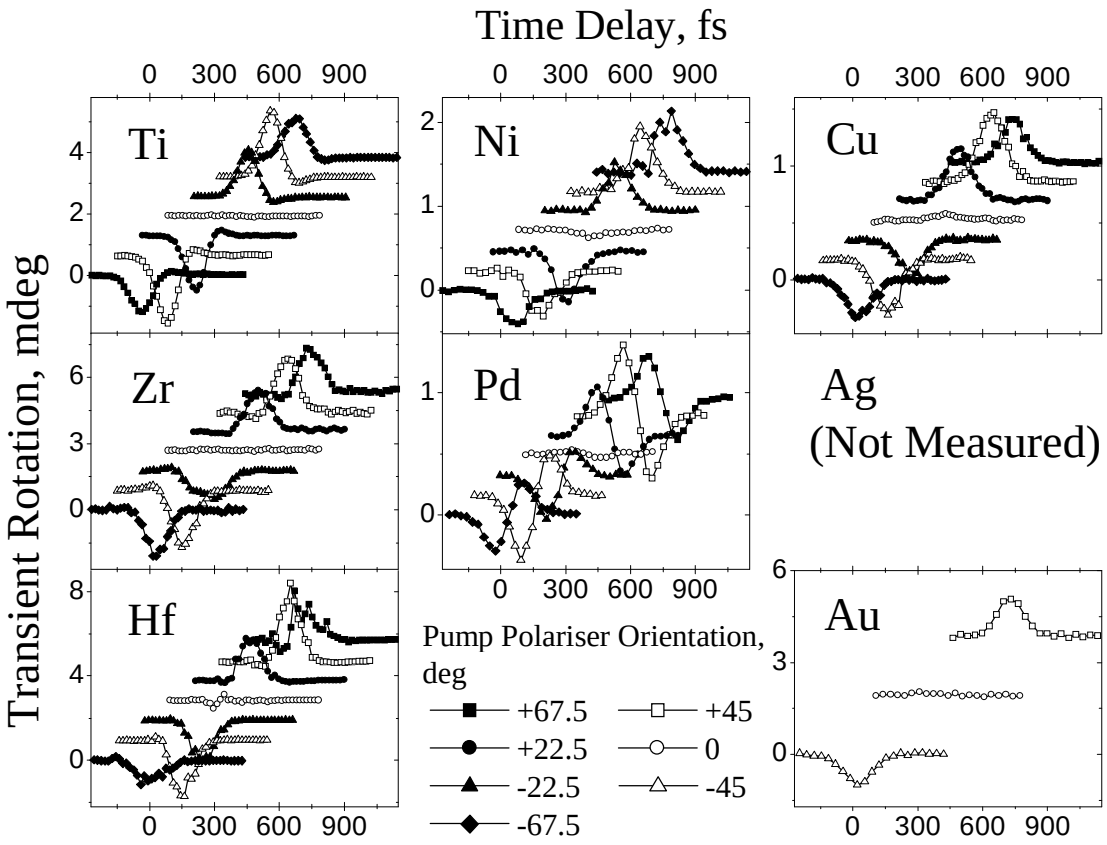

Figure 5.3 The transient rotation signals obtained in geometry 2 are presented. The signals obtained from different samples are arranged according to their position in the periodic table of elements.

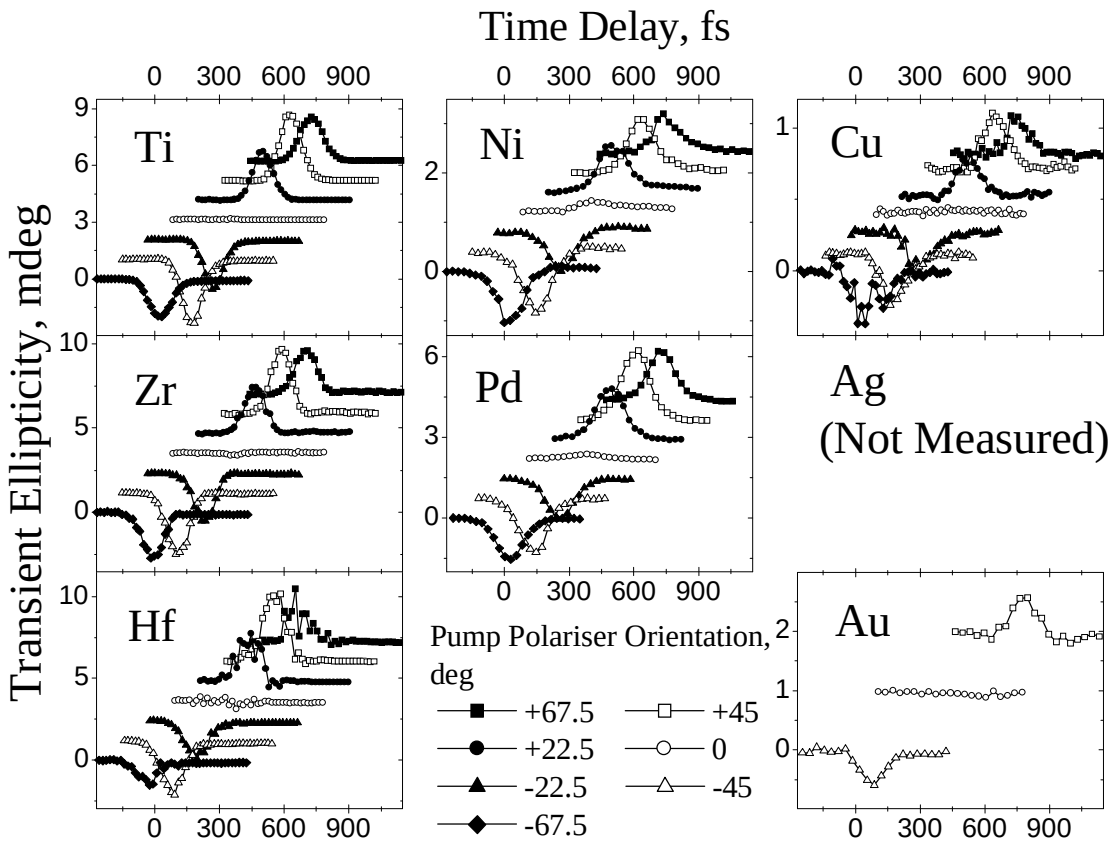

Figure 5.4 The transient ellipticity signals obtained in geometry 2 are presented. The signals obtained from different samples are arranged according to their position in the periodic table of elements.

5.3 Theory

5.3.1 Earlier Work and this Thesis

The dependence of the magnitude of the SIFE and SOKE upon the sample parameters and the pump intensity and polarisation was calculated by Zheludev et al. in the continuous wave excitation limit for circular and linear pump polarisations[75]. The generalisation of this theory for the case of elliptically polarised pump (1.2.14)-(1.2.16) was published by Wilks and Hicken[130]. In order to apply these equations to a femtosecond pump-probe experiment, an additional assumption had to be invoked that the signal should have the shape of the pump-probe intensity crosscorrelation, and the magnitude derived from the continuous wave model. It was suggested that these effects are due to the orientation of the electron linear and angular momentum. However, to the best of my knowledge, no attempts have been made to include the electron momentum relaxation within the description of the shape of time resolved SIFE and SOKE signals obtained from metallic samples. The time delay between the SIFE and SOKE peaks observed by Wilks and Hicken in aluminium[130] was explained in terms of the model described below.

The aim of this section is to develop the simplest model capable of describing the SIFE and SOKE signal shapes observed in the experiments. The model is based upon simple rate equations for electrons with different linear and (or) angular momentum. No attempts have been made to account for the band structures of different samples or subtleties of optical absorption theory.

The electron dynamics in metals are investigated with femtosecond time resolution in two photon photoemission experiments[3]. The idea that the signal can be described by a double convolution of an exponential decay with the laser pulse shape is

commonly used there, and served as a starting point for the model described below. Similar expressions were also used to fit time resolved polarisation signals obtained from semiconductors[131] and lately metallic Al[130]. However, only the contributions with longer (picosecond) relaxation times were fitted in this way, while the pump-probe crosscorrelation was still used to fit the initial peak that was observed on femtosecond time scales.

5.3.2 Simple Picture of Transient Optical Absorption

The probability of the optical absorption of photon with energy $E=\hbar\omega$ may be described as

$$S(E) = \int_{-\infty}^{+\infty}\int_{-\infty}^{+\infty} N(\varepsilon)\left|\tilde{M}(\varepsilon,\varepsilon',E)\right|H(\varepsilon')d\varepsilon d\varepsilon', \qquad (5.3.1)$$

where $N(\varepsilon)$ and $H(\varepsilon)$ are the total numbers of electrons and holes per unit energy at the energy level ε. $N(\varepsilon)$ and $H(\varepsilon)$ are equal to $\nu(\varepsilon)\zeta(\varepsilon)$ and $(1-\nu(\varepsilon))\zeta(\varepsilon)$, respectively, where $\nu(\varepsilon)$ is the electron distribution function, described at equilibrium by the Fermi-Dirac function (1.2.12), and $\zeta(\varepsilon)$ is the electron density of states (DOS). The function $\tilde{M}(\varepsilon,\varepsilon',E)$ is proportional to the probability of an electron transition from an individual state at energy ε to an individual state at energy ε' upon absorption of a photon of energy E. Conservation of energy demands that $\tilde{M}(\varepsilon,\varepsilon') = M(\varepsilon,\varepsilon')\delta(\varepsilon'-\varepsilon-E)$ so that the integration over ε' may be easily carried out, and we obtain

$$S(E) = \int_{-\infty}^{+\infty} N(\varepsilon)\left|M(\varepsilon,\varepsilon+E)\right|H(\varepsilon+E)d\varepsilon, \qquad (5.3.2)$$

Generally, the function $M(\varepsilon,\varepsilon+E)$ depends upon the matrix element for the electric dipole transitions between levels ε and $\varepsilon+E$, and hence upon the electronic structure of the sample. In order to rigorously treat the intraband processes, a realistic phonon

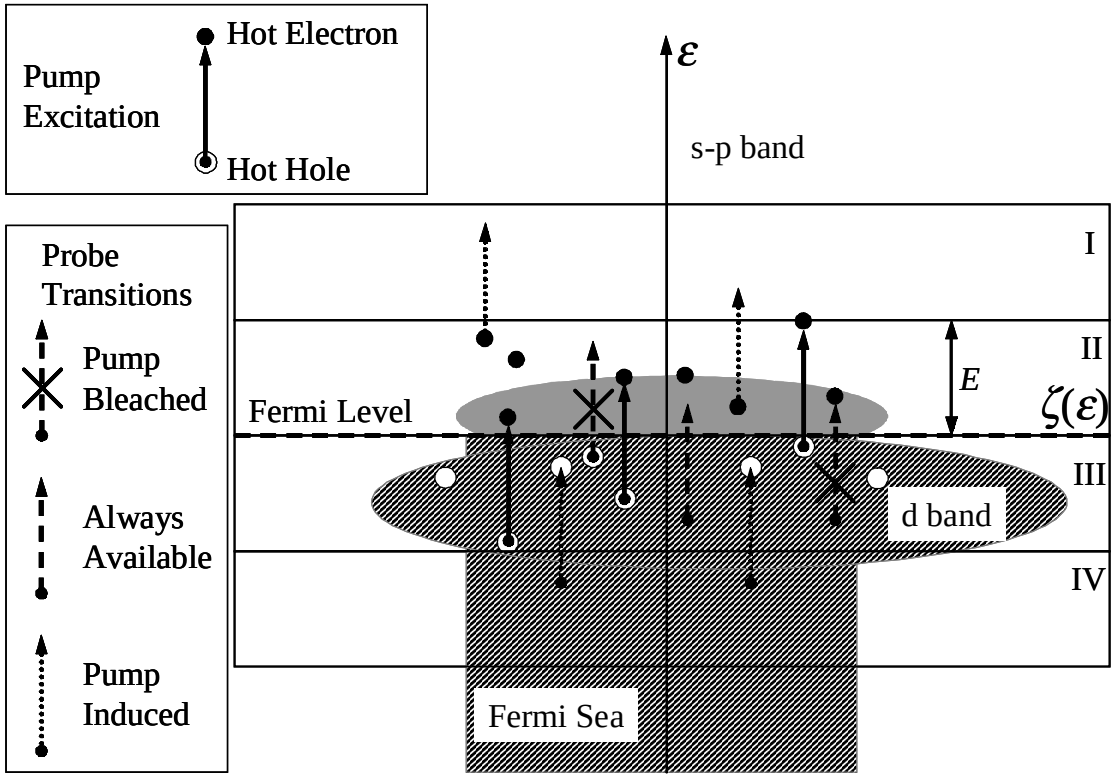

Figure 5.5 The effect of the pump excitation is schematically illustrated. In particular, it is shown how some transitions for the probe pulse are bleached and some are induced by the pump.

spectrum must also be considered. In addition, $M(\varepsilon,\varepsilon+E)$ depends upon the incident optical polarisation and the distribution electrons between different linear and angular momentum states. For the present argument, we simply postulate its existence.

For the unperturbed state at zero temperature, one may write

$$N(\varepsilon)=\begin{cases}0, & \text{for } \varepsilon>\varepsilon_F,\\ N_0(\varepsilon) & \text{for } \varepsilon<\varepsilon_F,\end{cases} \tag{5.3.3}$$

$$H(\varepsilon)=\begin{cases}H_0(\varepsilon), & \text{for } \varepsilon>\varepsilon_F,\\ 0, & \text{for } \varepsilon<\varepsilon_F,\end{cases} \tag{5.3.4}$$

where N_0 and H_0 are the unperturbed numbers of electrons and holes, respectively. Hence, one may write the unperturbed absorption probability at photon energy E as

$$S_0(E) = \int_{\varepsilon_F - E}^{\varepsilon_F} N_0(\varepsilon)\left|M(\varepsilon, \varepsilon + E)\right|H_0(\varepsilon + E)d\varepsilon \,. \tag{5.3.5}$$

If the electronic system is instantaneously excited by an intensive pump pulse, as shown in Figure 5.5, and remains in the excited state then

$$S(E) = I_1 + I_2 + I_3 \,, \tag{5.3.6}$$

where

$$I_1 = \int_{\varepsilon_F - 2E}^{\varepsilon_F - E} N_0(\varepsilon) M(\varepsilon, \varepsilon + E) h(\varepsilon + E) d\varepsilon \,, \tag{5.3.7}$$

$$I_2 = \int_{\varepsilon_F - E}^{\varepsilon_F} (N_0(\varepsilon) - h(\varepsilon)) M(\varepsilon, \varepsilon + E)(H_0(\varepsilon + E) - n(\varepsilon + E)) d\varepsilon \,, \tag{5.3.8}$$

$$I_3 = \int_{\varepsilon_F}^{\varepsilon_F + E} n(\varepsilon) M(\varepsilon, \varepsilon + E) H_0(\varepsilon + E) d\varepsilon \,, \tag{5.3.9}$$

where $n(\varepsilon)$ and $h(\varepsilon)$ are the numbers of non-equilibrium electrons and holes, respectively, excited to energy level ε. Strictly speaking, the function $M(\varepsilon,\varepsilon+E)$ is also modified by the pump. For the sake of simplicity, we neglect this effect and consider only the effects of the pump induced electron redistribution within the phase space.

In a pump-probe experiment, only *changes* in the absorption probability $\Delta S(E)=S(E)-S_0(E)$ may be sensed. Since $n(\varepsilon),h(\varepsilon) << N_0(\varepsilon),H_0h(\varepsilon)$, we retain only terms that are of first order in $n(\varepsilon)$ and $h(\varepsilon)$, and hence obtain

$$\begin{aligned}
\Delta S(E) \propto & \int_{\varepsilon_F - 2E}^{\varepsilon_F - E} N_0(\varepsilon)\left|M(\varepsilon, \varepsilon + E)\right| h(\varepsilon + E) d\varepsilon \\
& - \int_{\varepsilon_F - E}^{\varepsilon_F} N_0(\varepsilon)\left|M(\varepsilon, \varepsilon + E)\right| n(\varepsilon + E) d\varepsilon \\
& - \int_{\varepsilon_F - E}^{\varepsilon_F} h(\varepsilon)\left|M(\varepsilon, \varepsilon + E)\right| H_0(\varepsilon + E) d\varepsilon \\
& + \int_{\varepsilon_F}^{\varepsilon_F + E} n(\varepsilon)\left|M(\varepsilon, \varepsilon + E)\right| H_0(\varepsilon + E) d\varepsilon .
\end{aligned} \tag{5.3.10}$$

As one can see, the effect of the pump excitation is twofold. Firstly, the probe transition from region III to region II in Figure 5.5 is bleached by the presence of holes

in region III (third integral in the right hand side of (5.3.10)), and by the presence of electrons in region II (second integral). Secondly, the same hole and electron populations also permit optical transitions in which electrons are excited from region IV to region III (first integral), and from region II to region I (second integral). Hence, four different processes may contribute to the transient absorption change $\Delta S(E)$. In the dynamic case, the numbers of hot electrons and holes $n(\varepsilon)$ and $h(\varepsilon)$ must be replaced by time dependent functions $n(\varepsilon,t)$ and $h(\varepsilon,t)$ that account for the finite energy relaxation of the non-equilibrium carriers. The functions are calculated in section 5.3.4.

5.3.3 Model of SIFE and SOKE

In the SIFE and the SOKE, the sample acquires a linear and (or) circular birefringence upon absorption of an intense elliptically polarised pump pulse, that results from transfer of the linear and (or) angular momentum to the optically excited hot electrons. The linearly polarised probe pulse can be represented as a superposition of either two circularly polarised pulses with opposite helicities, or two linearly polarised pulses with polarisation axes that are parallel and perpendicular to that of the pump. The probe polarisation is then modified due to the difference in the refraction and absorption of the two circularly polarised components for the SIFE, and (or) the linearly polarised components for the SOKE.

Using (5.3.10), we describe the SIFE and SOKE by

$$\begin{aligned}\Delta S_{\mathrm{P}}(E,t) \propto & \int_{\varepsilon_F-2E}^{\varepsilon_F-E} N_0(\varepsilon) M(\varepsilon,\varepsilon+E) \delta h_{\mathrm{P}}(\varepsilon+E,t)\, d\varepsilon \\ & - \int_{\varepsilon_F-E}^{\varepsilon_F} N_0(\varepsilon) M(\varepsilon,\varepsilon+E) \delta n_{\mathrm{P}}(\varepsilon+E,t)\, d\varepsilon \\ & - \int_{\varepsilon_F-E}^{\varepsilon_F} \delta h_{\mathrm{P}}(\varepsilon,t) M(\varepsilon,\varepsilon+E) H_0(\varepsilon+E)\, d\varepsilon \\ & + \int_{\varepsilon_F}^{\varepsilon_F+E} \delta n_{\mathrm{P}}(\varepsilon,t) M(\varepsilon,\varepsilon+E) H_0(\varepsilon+E)\, d\varepsilon,\end{aligned} \tag{5.3.11}$$

where P denotes either the SIFE or the SOKE. Here, $\delta n_{\mathrm{P}}(\varepsilon,t)$ is the difference in the

number of electrons with angular momentum parallel and antiparallel to the pump linear momentum, in the case of the SIFE, and the difference in the number of electrons with linear momentum parallel and perpendicular to the axis of linear birefringence, in the case of the SOKE. Similarly, $\delta h_P(\varepsilon,t)$ represents the modified momentum distribution of the holes. The orientation of the electron linear momentum vector varies continuously, and hence our assignment of an electron to one of the two populations with orthogonal linear momentum is an assumption. Likewise the angular momentum may occupy a range of values depending upon the coupling scheme within the metal. In order to account for the transient rotation and ellipticity of the probe pulse, ΔS_P and M are now considered to be complex numbers, so that the transient rotation and ellipticity are given by the real and imaginary parts of ΔS_P. We also assume that M does not depend upon the electronic angular and linear momentum. In other words, the sample is assumed to be isotropic and nonmagnetic.

5.3.4 Rate Equations

Let us consider the number of electrons or holes at an energy level ε. We assume that every electron with this energy is in one of four states defined by the two possible values of the linear momentum and the angular momentum. The number of electrons or holes changes either via elastic scattering between these four states, or via inelastic scattering from the energy level. In the relaxation time approximation, both these processes and the excitation by the pump pulse can be described by the following system of kinetic equations in the relaxation time approximation (also known as the rate equations)

$$\dot{\rho}^{\uparrow Y} = -\alpha^{\uparrow Y}\rho^{\uparrow Y} + \alpha^{\uparrow\uparrow YZ}\rho^{\uparrow Z} + \alpha^{\uparrow\downarrow YY}\rho^{\downarrow Y} + \alpha^{\uparrow\downarrow YZ}\rho^{\downarrow Z} + sqI(t), \qquad (5.3.12)$$

$$\dot{\rho}^{\uparrow Z} = \alpha^{\uparrow\uparrow ZY}\rho^{\uparrow Y} - \alpha^{\uparrow Z}\rho^{\uparrow Z} + \alpha^{\uparrow\downarrow ZY}\rho^{\downarrow Y} + \alpha^{\uparrow\downarrow ZZ}\rho^{\downarrow Z} + rqI(t), \qquad (5.3.13)$$

$$\dot{\rho}^{\downarrow Y} = \alpha^{\downarrow\uparrow YY}\rho^{\uparrow Y} + \alpha^{\downarrow\uparrow YZ}\rho^{\uparrow Z} - \alpha^{\downarrow Y}\rho^{\downarrow Y} + \alpha^{\downarrow\downarrow YZ}\rho^{\downarrow Z} + spI(t), \quad (5.3.14)$$

$$\dot{\rho}^{\downarrow Z} = \alpha^{\downarrow\uparrow ZY}\rho^{\uparrow Y} + \alpha^{\downarrow\uparrow ZZ}\rho^{\uparrow Z} + \alpha^{\downarrow\downarrow ZY}\rho^{\downarrow Y} - \alpha^{\downarrow Z}\rho^{\downarrow Z} + rpI(t), \quad (5.3.15)$$

where the source terms in the right hand side are defined for electrons by

$$I(\varepsilon,x,t) = \frac{2A_0}{\sigma E}\sqrt{\frac{\ln 2}{\pi}}\exp\left\{-\frac{x}{l_0} - \frac{4\ln 2(t-t_0)^2}{\sigma^2}\right\}N_0(\varepsilon - E)\left|M(\varepsilon - E,\varepsilon)\right|H_0(\varepsilon), \quad (5.3.16)$$

and for holes by

$$I(\varepsilon,x,t) = \frac{2A_0}{\sigma E}\sqrt{\frac{\ln 2}{\pi}}\exp\left\{-\frac{x}{l_0} - \frac{4\ln 2(t-t_0)^2}{\sigma^2}\right\}N_0(\varepsilon)\left|M(\varepsilon,\varepsilon + E)\right|H_0(\varepsilon + E). \quad (5.3.17)$$

In these equations, the function $\rho_j^{\sigma 1\sigma 2}$ is the number of electrons ($n_P(\varepsilon,t)$) or holes ($h_P(\varepsilon,t)$) in state $\sigma 1\sigma 2$, where $\sigma 1$ represent $\uparrow$ ("angular momentum up") or $\downarrow$ ("angular momentum down"), and $\sigma 2$ represents Y (linear momentum parallel to the y-axis) or Z (linear momentum parallel to the z-axis); $\alpha^{\sigma 1\sigma 2}$ is the total scattering rate (inelastic and elastic processes) for state $\sigma 1\sigma 2$; $\alpha^{\sigma 1\sigma 1'\sigma 2\sigma 2'}$ is the elastic scattering rate from state $\sigma 1'\sigma 2'$ to state $\sigma 1\sigma 2$; A_0 is the pump pulse energy per unit excited volume, which is equal to Sl_0, where S is the pump spot area and l_0 is the optical skin-depth of the material; σ is the full width at half maximum (FWHM) of the pump pulse; t_0 is the time of arrival of the pump pulse at the sample, and t is the time variable. The parameters p and q describe the efficiency of angular momentum orientation so that for linearly polarised pump p=q=0.5, and for left and right circular polarisation p=1, q=0, and p=0, q=1, respectively. Let us choose the coordinate system so that the z-axis is at 45° to the probe plane of polarisation. Then, the parameters r and s describe the efficiency of linear momentum orientation parallel to the z- and y-axes, respectively, so that for pump polarised either circularly or linearly parallel or perpendicular to the probe polarisation r=s=0.5, and for linear polarisation parallel to the z- and y-axis r=1, s=0, and r=0, s=1, respectively.

Let us denote $\rho_0 = \rho^{\uparrow Y} + \rho^{\uparrow Z} + \rho^{\downarrow Y} + \rho^{\downarrow Z}$, $\rho_{\updownarrow} = (\rho^{\uparrow Y} + \rho^{\uparrow Z}) - (\rho^{\downarrow Y} + \rho^{\downarrow Z})$, $\rho_{YZ} = (\rho^{\uparrow Z} + \rho^{\downarrow Z}) - (\rho^{\uparrow Y} + \rho^{\downarrow Y})$, and $\rho_X = (\rho^{\downarrow Y} + \rho^{\uparrow Z}) - (\rho^{\uparrow Y} + \rho^{\downarrow Z})$. We note that ρ_0 is the total number of hot electrons (holes), $\rho_{\updownarrow}$ and ρ_{YZ} are the angular and linear momentum polarisations of the hot electron (hole) population $\delta n_{SIFE}(\varepsilon,t)$ and $\delta n_{SOKE}(\varepsilon,t)$ ($\delta h_{SIFE}(\varepsilon,t)$ and $\delta h_{SOKE}(\varepsilon,t)$), while the physical meaning of ρ_X is unclear.

If we assume that the total scattering rates $\alpha^{\sigma 1 \sigma 2}$ are all equal to the same constant α, and that the scattering rates $\alpha^{\sigma 1 \sigma 1' \sigma 2 \sigma 2'}$ are equal to $\alpha^{\updownarrow}$, if $\sigma 1' \neq \sigma 1$ and $\sigma 2' = \sigma 2$; α^{YZ}, if $\sigma 1' = \sigma 1$ and $\sigma 2' \neq \sigma 2$; and α^{X}, if $\sigma 1' \neq \sigma 1$ and $\sigma 2' \neq \sigma 2$, then we obtain

$$\dot{\rho}_0 = -(\alpha - \alpha^{YZ} - \alpha^{\updownarrow} - \alpha^{X})\rho_0 + I(x,t), \tag{5.3.18}$$

$$\dot{\rho}_{\updownarrow} = -(\alpha - \alpha^{YZ} + \alpha^{\updownarrow} + \alpha^{X})\rho_{\updownarrow} + (r+s)(q-p)I(x,t), \tag{5.3.19}$$

$$\dot{\rho}_{YZ} = -(\alpha + \alpha^{YZ} - \alpha^{\updownarrow} + \alpha^{X})\rho_{YZ} + (r-s)(q+p)I(x,t), \tag{5.3.20}$$

$$\dot{\rho}_X = -(\alpha + \alpha^{YZ} + \alpha^{\updownarrow} - \alpha^{X})\rho_X + (r-s)(q-p)I(x,t). \tag{5.3.21}$$

All these equations have the same form and may be solved analytically to obtain the particular integral

$$\rho^* = \frac{A_0^* \exp\left\{-\frac{x}{l_0} + \left(\frac{\sigma\alpha^*}{4\sqrt{\ln 2}}\right)^2 - \alpha^*(t-t_0)\right\}}{2E}\left(1 + erf\left(\frac{2\sqrt{\ln 2}(t-t_0)}{\sigma} - \frac{\sigma\alpha^*}{4\sqrt{\ln 2}}\right)\right), \tag{5.3.22}$$

where

$$\rho^* = \begin{cases} \rho_0, \\ \rho_{\updownarrow} = \begin{cases} \delta n_{SIFE}(\alpha_n^{SIFE}(\varepsilon),t), \text{ or} \\ \delta h_{SIFE}(\alpha_h^{SIFE}(\varepsilon),t), \end{cases} \\ \rho_{YZ} = \begin{cases} \delta n_{SOKE}(\alpha_n^{SOKE}(\varepsilon),t), \text{ or} \\ \delta h_{SOKE}(\alpha_h^{SOKE}(\varepsilon),t), \end{cases} \\ \rho_X, \end{cases} \tag{5.3.23}$$

$$\alpha^* = \begin{cases} \alpha\ -\alpha^{YZ} -\alpha^{\updownarrow} -\alpha^{X} \equiv \alpha_0, \\ \alpha\ -\alpha^{YZ} +\alpha^{\updownarrow} +\alpha^{X} \equiv \alpha_{\updownarrow} = \begin{cases} \alpha_n^{\mathrm{SIFE}}(\varepsilon), \text{ or} \\ \alpha_h^{\mathrm{SIFE}}(\varepsilon), \end{cases} \\ \alpha\ +\alpha^{YZ} -\alpha^{\updownarrow} +\alpha^{X} \equiv \alpha_{YZ} = \begin{cases} \alpha_n^{\mathrm{SOKE}}(\varepsilon), \text{ or} \\ \alpha_h^{\mathrm{SOKE}}(\varepsilon), \end{cases} \\ \alpha\ +\alpha^{YZ} +\alpha^{\updownarrow} -\alpha^{X} \equiv \alpha_X, \end{cases} \tag{5.3.24}$$

and

$$A_0^*(\varepsilon) = A_0 N_0(\varepsilon - E)\left|M(\varepsilon - E, \varepsilon)\right| H_0(\varepsilon) \times \begin{cases} 1, \\ (r+s)(q-p), \\ (r-s)(q+p), \\ (r-s)(q-p), \end{cases} \tag{5.3.25}$$

for electrons, and

$$A_0^*(\varepsilon) = A_0 N_0(\varepsilon)\left|M(\varepsilon, \varepsilon + E)\right| H_0(\varepsilon + E) \times \begin{cases} 1, \\ (r+s)(q-p), \\ (r-s)(q+p), \\ (r-s)(q-p), \end{cases} \tag{5.3.26}$$

for holes.

The dependence upon energy enters these expressions through that of the relaxation rates (5.3.24). For example, the Fermi liquid theory predicts that the inelastic scattering rate of electrons is proportional to square of the excess energy relative to the Fermi level. Therefore, the integrals in (5.3.11) should be now evaluated. However, in our simplified approach we avoid this in the following way. We divide the integration interval in every integral in (5.3.11) into several parts so that in each interval we can neglect the dependence of the various relaxation rates upon energy. Then we can rewrite (5.3.11) as

$$\Delta S_{\mathrm{P}}(E,t) \propto \sum_{j=1}^{\xi_h} k_{h,j}^P \delta h_{\mathrm{P}}(\alpha_{h,j}^P, t) + \sum_{j=1}^{\xi_n} k_{n,j}^P \delta n_{\mathrm{P}}(\alpha_{n,j}^P, t), \tag{5.3.27}$$

where the complex coefficients $k_{h,j}^P$ and $k_{n,j}^P$ are given by

$$k^P_{h,j} = \int_{\varepsilon_{h,j}}^{\varepsilon_{h,j+1}} A_0^*(\varepsilon)\big(N_0(\varepsilon - E)M(\varepsilon - E,\varepsilon) - M(\varepsilon,\varepsilon + E)H_0(\varepsilon + E)\big)d\varepsilon\,, \tag{5.3.28}$$

$$k^P_{n,j} = \int_{\varepsilon_{n,j}}^{\varepsilon_{n,j+1}} A_0^*(\varepsilon)\big(M(\varepsilon,\varepsilon + E)H_0(\varepsilon + E) - N_0(\varepsilon - E)M(\varepsilon - E,\varepsilon)\big)d\varepsilon\,, \tag{5.3.29}$$

$$\varepsilon_{h,1} = \varepsilon_F - E\,,\ \ \varepsilon_{h,\xi_h+1} = \varepsilon_F\,,\ \ \varepsilon_{n,1} = \varepsilon_F\,,\ \ \varepsilon_{n,\xi_n+1} = \varepsilon_F + E\,, \tag{5.3.30}$$

and the functions $\delta h_{\mathrm{P}}(\alpha^P_{h,j},t)$ and $\delta n_{\mathrm{P}}(\alpha^P_{n,j},t)$ are defined by equations (5.3.22)-(5.3.24), but without the prefactor $A_0^*(\varepsilon)$. In the simplest case when one neglects the energy dependence of the scattering rate, there are only two terms in the right hand side of (5.3.27): one for electrons and one for holes.

By comparing with equations (1.2.14) and (1.2.15), it is easy to see that parameters *r*, *s*, *q*, and *p* must depend upon the orientation of the quarter wave plate φ in the experiment with elliptically polarised pump as

$$\begin{aligned} r &= \frac{1}{2}\big(1+\sin 4\varphi\big),\ \ s = \frac{1}{2}\big(1-\sin 4\varphi\big), \\ q &= \frac{1}{2}\big(1+\sin 2\varphi\big),\ \ p = \frac{1}{2}\big(1-\sin 2\varphi\big), \end{aligned} \tag{5.3.31}$$

and upon the orientation of the polarizer ψ in an experiment with linearly polarised pump as

$$r = \frac{1}{2}\big(1+\sin 2\psi\big),\ \ s = \frac{1}{2}\big(1-\sin 2\psi\big),\ \ q = p = \frac{1}{2}. \tag{5.3.32}$$

The rotation and ellipticity signals are equal to the real and imaginary parts of (5.3.27), respectively.

5.3.5 Simulations

As far as the experiments are concerned, the main result of this calculation is that a transient SIFE or SOKE signal may in general contain several contributions of the form (5.3.22), convolved with the temporal form of the probe intensity, for which we

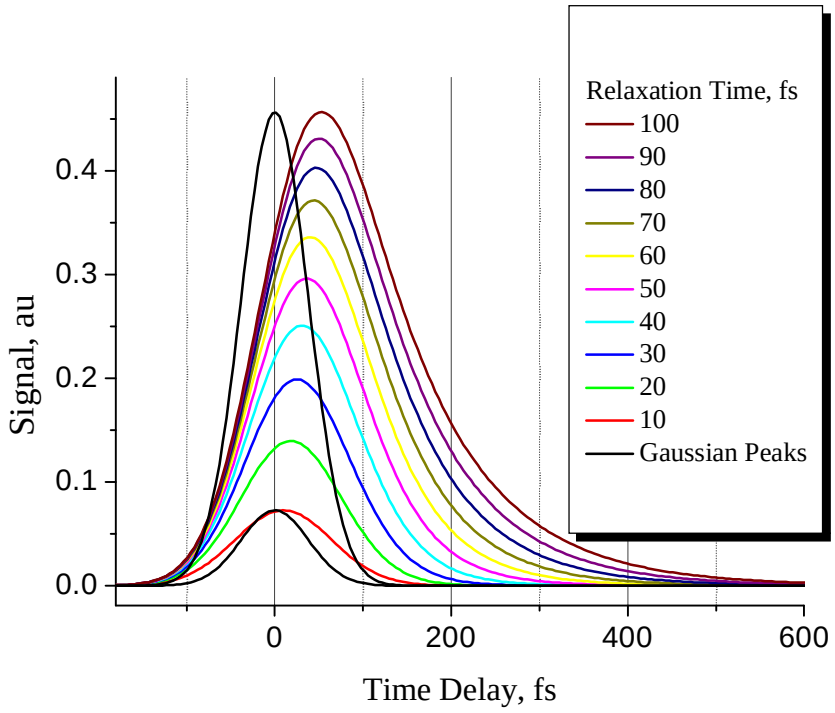

Figure 5.6 The dependence of the signal shape defined in equation (5.3.22) upon the relaxation time $\tau^{*}=1/\alpha^{*}$ is illustrated. The FWHM was set to 90 fs. The signal was convolved with the temporal form of the probe intensity.

assumed a Gaussian shape. Let us consider a signal that is described by a single term of the type given in (5.3.22). The dependence of the signal shape upon the relaxation time $\tau^{*}=1/\alpha^{*}$ is illustrated in Figure 5.6. Increasing the relaxation time gives rise to four effects: the time resolved signal becomes bigger and more asymmetric, it broadens, and the position of the maximum shifts towards positive time delay.

In order to fit our data it was necessary to include two terms of the type given in (5.3.22)

$$\theta^{SIFE(SOKE)}(\eta^{SIFE(SOKE)}) \propto$$
$$\frac{1}{2}\sum_{j=1}^{2} A_{\theta(\eta),j}^{SIFE(SOKE)}\left(1+erf\left(\frac{t_d\sqrt{2\ln 2}}{\sigma}-\frac{\sigma}{2\tau_j^{SIFE(SOKE)}\sqrt{2\ln 2}}\right)\right)\exp\left\{-\frac{t_d}{\tau_j^{SIFE(SOKE)}}\right\}, \quad (5.3.33)$$

where $A_{\theta(\eta),j}^{SIFE(SOKE)}$ are the amplitudes of the SIFE and SOKE signal components in rotation and ellipticity, and t_d is the pump-probe time delay. In fitting the experimental data, these should be treated as adjustable parameters. Also, for a particular metal, the same four relaxation times $\tau_1^{SIFE(SOKE)}$ and $\tau_2^{SIFE(SOKE)}$ should be used in fitting the SIFE and SOKE rotation and ellipticity signals, while the value of the zero delay time t_0 should be the same for all four traces. As the model does not allow us to identify the physical origin of the two contributions, the results of the fitting procedure will require additional interpretation.

So far, we have neglected any transport effects. However, ballistic electron transport takes place on femtosecond time scales and may cause reduction of the signal, if hot electrons are able to leave the excited volume of the sample. This may be accounted for crudely by substituting the skin depth l_0 in equations above by l_0+l_{bal}, where the ballistic range l_{bal} is understood to be the average distance a hot electron can travel in the direction away from the surface before it is first scattered. This distance depends upon the average collision frequency and the electron group velocity, and has a value of about 100 nm for noble metals[9].

5.4 Analysis and Discussion

5.4.1 Time Resolved SIFE and SOKE Contributions

For the signals measured in geometry 1, both the SIFE and SOKE contributions were present simultaneously. These could be separated since, according to equations (1.2.14) and (1.2.15), for pairs of signals with φ equal to +22.5° and +67.5° (or alternatively -22.5° and -67.5°) the SIFE component has the same magnitude and sign, while the SOKE component has the same magnitude but opposite sign. This means that the difference divided by 2 of the signals at +22.5° and +67.5° (or -22.5° and -67.5°) contains only the SOKE component, while their sum contains only the SIFE component, but multiplied by $\sqrt{2}$ in comparison with that measured at φ=±45°. In order to improve the signal-to-noise ratio and to remove any remaining background due to the reflectivity breakthrough, the SOKE signals extracted from pairs of signals at +22.5° and +67.5°, and -22.5° and -67.5° were averaged. Similarly, the SIFE components extracted from these pairs of signals and divided by $\sqrt{2}$ were averaged with the SIFE signals measured at φ=±45°. The extracted time resolved SIFE and SOKE contributions to the signal measured in geometry 1 are shown in Figure 5.7. We note that, strictly speaking, formulae (1.2.14)-(1.2.16) are valid only at normal incidence. However, they provide a reasonable approximation to the present experimental configuration since the pump and probe beams are strongly refracted towards the film normal within the sample.

It is easy to see that there is a striking similarity between the relative signs and relative magnitudes of the SIFE and SOKE signals shown in Figure 5.7 within the group of noble metals. Zr and Hf define a second group to which Ti can also be assigned if

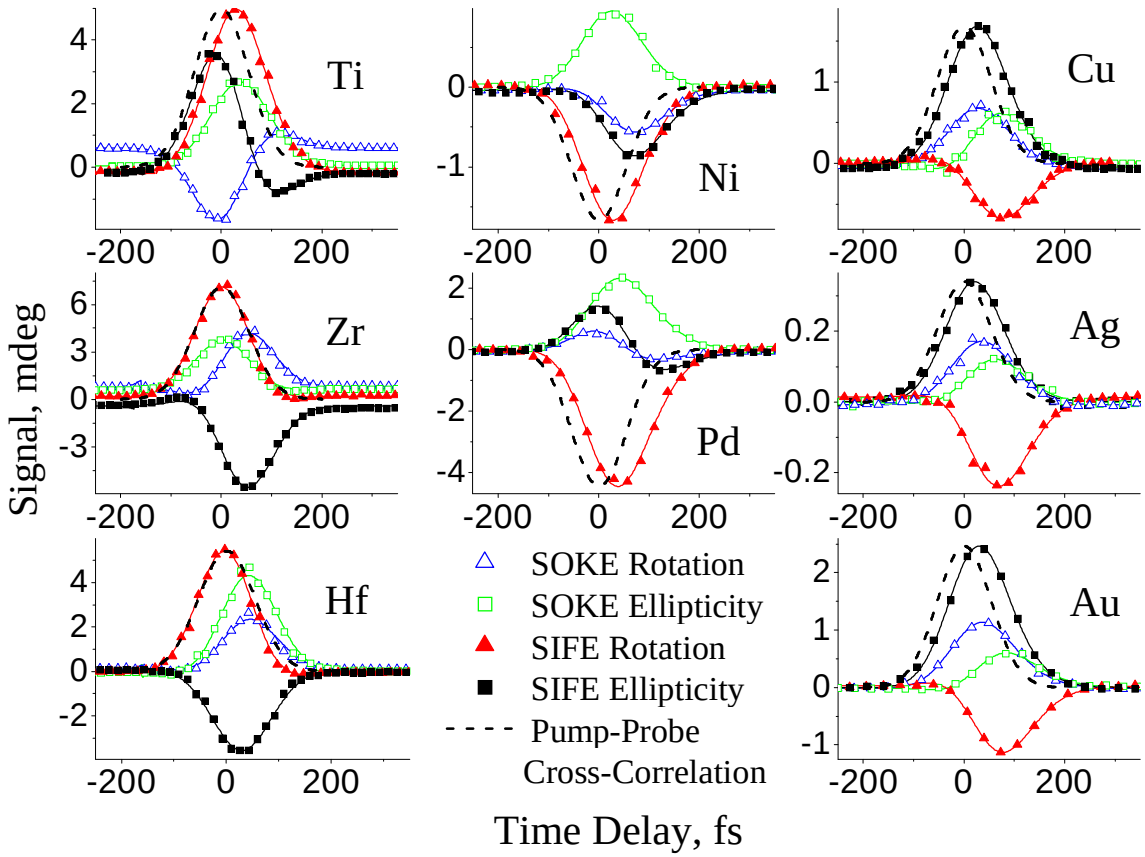

Figure 5.7 The SIFE and SOKE contributions to the transient polarization response (symbols are data points, and solid curves are fits to (5.3.33), as explained in the text) are shown with the pump-probe intensity cross-correlation for the different samples measured.

one assumes that the bipolar shapes of the Ti SIFE ellipticity and SOKE rotation traces result from the presence of two peak-like contributions (two each for SIFE and SOKE) that have different centre positions and opposite signs. One of these peaks tends to make the SIFE and SOKE signals similar to those of Zr and Hf, while the other peak breaks the similarity. Making similar allowance for the bipolar shape of the Pd SIFE ellipticity and SOKE rotation signals, Pd and Ni form another group. The relative signs and magnitudes of the signals differ substantially between the three different groups. To make this observation even clearer, the complex amplitudes of the SIFE (F_-) and

SOKE ($F_+/2$), as defined by equation (1.2.16), determined from the maximum values of signals shown in Figure 5.7 are plotted in Figure 5.8 for the different metals. The "alternative" values of F_- and $F_+/2$ for Ti and Pd are shown by dashed lines. The three groups correspond to three different columns of the periodic table of elements, and so a different colour has been used for each group.

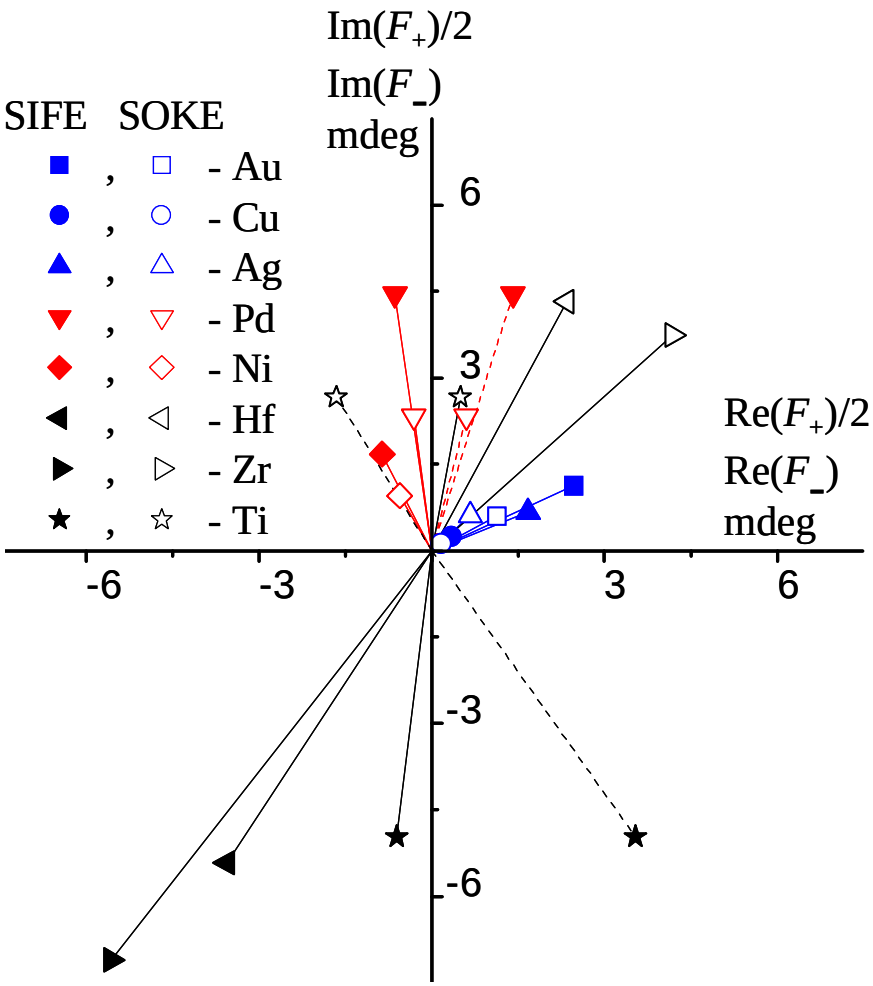

Figure 5.8 The complex SIFE (F_-) and SOKE ($F_+/2$) magnitudes are shown with filled and open symbols, respectively, on the complex plane for different samples. Different colours were used to denote metals from different groups of the periodical table. Dashed lines correspond to the "alternative" values of F_- and F_+ for Ti and Pd that correspond to the peaks breaking the similarity with the other metals in their groups.

The electronic structure is similar within each group as far as optical properties are concerned. For example, at the photon energy used in our experiments the optical response of the noble metals is entirely due to intraband optical transitions[132], while that of Ti, Zr, and Hf is dominated by interband transitions[133,134]. The optical structures of Ni and Pd are more complicated, and both interband and intraband transitions can contribute[134]. This interpretation is supported by the observation that the signals of largest and smallest magnitude occur in Zr and Ag, respectively.

5.4.2 Linear and Angular Momentum Relaxation Times

The SIFE and SOKE contributions (both in rotation and ellipticity) generally occur at different time delays. However, the zero delay condition must be uniquely defined. Therefore the non-linear response cannot be described as a cross-correlation of the pump and probe intensity envelopes, as has been previously assumed (for example see Ref. 127), and hence, cannot be used for the purpose of pulse width measurements. The temporal positions of the SIFE and SOKE peaks are summarised in Table 5.2. The same allowance for the bipolar shaped signals of Pd and Ti is made. One can see that the relative order of appearance of the SIFE and SOKE peaks is the same within each group of metals, the only exception being the transient ellipticity signal of Hf in which the SIFE and SOKE have opposite order to that in Ti and Zr.

The temporal shapes of the SIFE and SOKE signals may be described by a convolution of the probe intensity envelope with evolution functions for the sample polarisation, as discussed in the previous section. This transient polarisation results from optical orientation of electronic linear and angular momentum and decays on timescales of tens of femtoseconds. Differences in the relaxation times of the SIFE and SOKE cause their peak positions to be shifted by different amounts, as shown in Figure 5.7, and as is readily apparent when SIFE and SOKE are both present in the same measurement, as in geometry 1.

	SIFE Rotation, fs	SIFE Ellipticity, fs	SOKE Rotation, fs	SOKE Ellipticity, fs
Cu	77	27	29	75
Ag	71	21	35	63
Au	77	31	37	85
Ni	27	70	72	25
Pd	39	131 (-1)	117 (-9)	43
Ti	30	110 (-10)	110 (-8)	38
Zr	0	53	57	2
Hf	-3	29	45	43

Table 5.2 The temporal positions of the SIFE and SOKE peaks are summarised. The numbers in parenthesis for Ti and Pd correspond to the "alternative" peaks that break the similarity with the other metals in their groups.

The relaxation times have been extracted by fitting the measured SIFE and SOKE signals to equation (5.3.33). The bipolar shapes of the extracted SIFE and SOKE components for Ti and Pd suggest the presence of two contributions for each effect of opposite sign and different relaxation times. Hence, a superposition of two double convolutions in the equation (5.3.33) was used in the fitting. This has been further justified by the fitting process. For a particular metal, it was not possible to obtain a satisfactory fit with a model that contained a single double convolution, if the same value of the zero delay time was used for all four traces. The fitted SIFE and SOKE contributions are represented in Figure 5.7 by solid curves. The fitting parameters are summarised in Table 5.3. The statistical significance of the fit is discussed below.

	SIFE		SOKE	
	τ_1, fs ($A_{\theta,1}$, $A_{\eta,1}$, au)	τ_2, fs ($A_{\theta,2}$, $A_{\eta,2}$, au)	τ_1, fs ($A_{\theta,1}$, $A_{\eta,1}$, au)	τ_2, fs ($A_{\theta,2}$, $A_{\eta,2}$, au)
Cu	**25** (20.6, -3.4)	**27.5** (-19.5, 5.0)	**22.5** (8.0, 44.9)	**23.5** (-8.5, -43.3)
Ag	**24.5** (11.10, 0.51)	**26** (-10.80, -0.09)	**22** (8.88, 15.68)	**22.5** (-8.93, -15.48)
Au	**27.5** (175.6, -54.6)	**28** (-173.9, 56.5)	**31.5** (56.6, 136.7)	**32** (-57.2, -136.0)
Ni	**25.5** (-24.2, -78.7)	**26.5** (22.7, 79.8)	**24.5** (-70.9, 11.4)	**25** (70.0, -12.3)
Pd	**30** (54.3, 72.5)	**31.5** (-56.6, -68.5)	**9.5** (-4.7, 2.6)	**44** (0.79, -2.30)
Ti	**9** (-11.8, 38.6)	**23** (11.4, -12.0)	**17** (203.4, 126.1)	**18** (-192.1, -125.0)
Zr	**10.5** (71.8, 158.8)	**14.5** (-39.8, -124.9)	**10** (150.9, -33.1)	**13** (-120.7, 18.8)
Hf	**11** (134.5, 82.6)	**13** (-103.1, -77.7)	**10.5** (162.4, 288.3)	**12** (-148.9, -265.4)

Table 5.3 The parameters obtained by fitting to equation (5.3.33) the SIFE and SOKE contributions shown in Figure 5.7 are presented.

The values presented in Table 5.3 fall into two categories. In the first, occupied by the noble metals and Ni, the difference of the two relaxation times for SIFE (or SOKE) is small. Within the framework of the theory developed in the previous section, this suggests that the transient polarisation response results from excitation of transitions in one particular region of the band structure. The initial and final states occupy finite phase volumes that may be large for intraband transitions. The corresponding relaxation time will generally exhibit dispersion associated with the range of initial and final states that are involved. The use of two similar relaxation

times in our model provides a crude representation of this dispersion, which may lead to a small shift in the position of the maximum in the signal. Alternatively, if the relaxation times differ significantly, as in Hf, Zr, Pd SOKE and Ti SIFE, then the signal may originate from states in two distinctly different places in the band structure. These states may even have the same energy, since time resolved two photon photoemission experiments[3] have shown that hot electron lifetimes at a particular energy depend on whether excitation was caused by an interband or intraband transition.

After the initial coherence of the electron-hole pairs has been broken, the distribution of linear and angular momentum of the hot electrons and holes may still retain some memory of the pump polarisation. The action of a linearly polarised pump pulse reduces the symmetry of the momentum space electron distribution and induces an axial symmetry. The SOKE relaxation times characterise the recovery of the symmetry of the distribution, but only in the region of the band structure sensed by the probe beam. The latter region itself represents a sub region of region II in Figure 5.5 for electrons, and a sub region of region III for holes.

Because the linear momentum of the photon is small compared to that of the electrons and phonons, electronic linear momentum is conserved in interband transitions, and hence only vertical transitions are allowed, as shown in Figure 1.10. Then, due to energy conservation, the detection region is a narrow sub region of region II in Figure 5.5, for electrons, and a narrow sub region of region III, for holes. Therefore any inelastic scattering results in removal of an electron (hole) from the detection region and leads to a change in the measured linear momentum. Because a phonon, the linear momentum of which is finite, participates in an intraband transition, electronic linear momentum is not conserved, and hence indirect transitions are also allowed, as shown in Figure 1.10. Then, the detection region may continuously span the entire region II in Figure 5.5, for electrons, and the entire region III, for holes.

Inelastically scattered electrons and holes are then more likely to remain within the detection region and contribute to the transient polarisation response. This implies that experiments involving intraband transitions should provide a better estimate of the momentum relaxation time.

The action of a circularly polarised pulse leads to a repopulation of electrons and holes between states with a different angular momentum component in the direction of the pump pulse wave vector. The corresponding SIFE relaxation time describes the recovery of the symmetry of the initial angular momentum distribution. Again it is preferable that the probe response is dominated by intraband transitions or else inelastic scattering may obscure the relaxation of hot electron (hole) angular momentum.

5.4.3 Third Order Susceptibility Tensor Components

Using the magnitudes of the SIFE and SOKE contributions shown in Figure 5.8 and equations (1.2.14)-(1.2.16), it is possible to extract the values of the $\chi^{(3)}$ components. However in doing this one should bear in mind that the formulae were derived for cw excitation, and are not strictly speaking applicable when the pump pulse and the SIFE and SOKE response do not overlap exactly in time. Hence, there is a question as to what intensity to use: the peak value or the value at the moment when the polarisation response is at maximum. Our heuristic theory does not include the $\chi^{(3)}$ components explicitly, and so does not provide any further insight. In order to be consistent with other works, we substitute the peak magnitudes from Figure 5.8 and the peak intensity to equation (1.2.16).

The non-vanishing $\chi^{(3)}$ components are summarized in Table 5.4 together with the assumed values of the complex refractive index. To the best of our knowledge, the ultrafast third-order non-linearity has been explored in only a few pure metals (Au[8], Ni[126-129], In[126] and Al[130]). Our results for Ni are in good order of magnitude agreement

	n+ik	Re(χ_{xxyy}), 10^{-11} esu	Im(χ_{xxyy}), 10^{-11} esu	Re(χ_{xyyx}), 10^{-11} esu	Im(χ_{xyyx}), 10^{-11} esu
Cu	0.246+i4.95 [136]	4.6	-10	1.9	0.76
Ag	0.144+i5.19 [136]	1.7	-2.9	0.012	0.009
Au	0.178+i4.99 [136]	6.2	-17	0.32	0.62
Ni	2.33+i4.59 [136]	12	-14	1.3	-0.82
Pd	2.00+i5.04 [134]	29 (9.4)	-43 (-52)	0.46 (1.6)	-1.1 (-0.54)
Ti	3.11+i4.01 [133]	-1.9 (-1.3)	-0.78 (-1.0)	-20 (10)	-35 (-47)
Zr	2.98+i3.65 [133]	-7.5	2.3	-52	-20
Hf	2.65+i2.83 [133]	-3.2	-2.2	-17	-7.5

Table 5.4 The real and imaginary parts of the non-vanishing components of $\chi^{(3)}$, extracted from data shown in Figure 5.8 using equations (1.2.16), are presented for different metals together with the real and imaginary parts of the complex refractive index $\hat{n} = n + ik$ used in the calculations. The values in parenthesis for Ti and Pd correspond to the "alternative" peaks of the bipolar signals discussed in the text and shown by dashed lines in Figure 5.8.

with a value of $\left|\mathrm{Im}(\chi_{xxyy} - \chi_{xyyx})\right| = 3\times10^{-10}$ esu deduced at 810 nm in Ref. 127, and $\chi_{xxyy} = (1.3 - i2.7)\times10^{-10}$ esu, $\chi_{xyyx} = (-9.0 + i1.7)\times10^{-12}$ esu deduced at 790 nm and normal incidence in Ref. 129. The discrepancy with a value of $\left|\chi_{xxyy} - \chi_{xyyx}\right| = 1.5\times10^{-8}$ esu deduced for Au in Ref. 8 is greater and is most likely due to the longer wavelength used in that study. The values of the $\chi^{(3)}$ components are plotted in the complex plane in Figure 5.9 so that similarities and differences between the different metals may be observed. The values differ considerably in magnitude and so have been normalized to lie on the unit circle. The different metals still fall into well

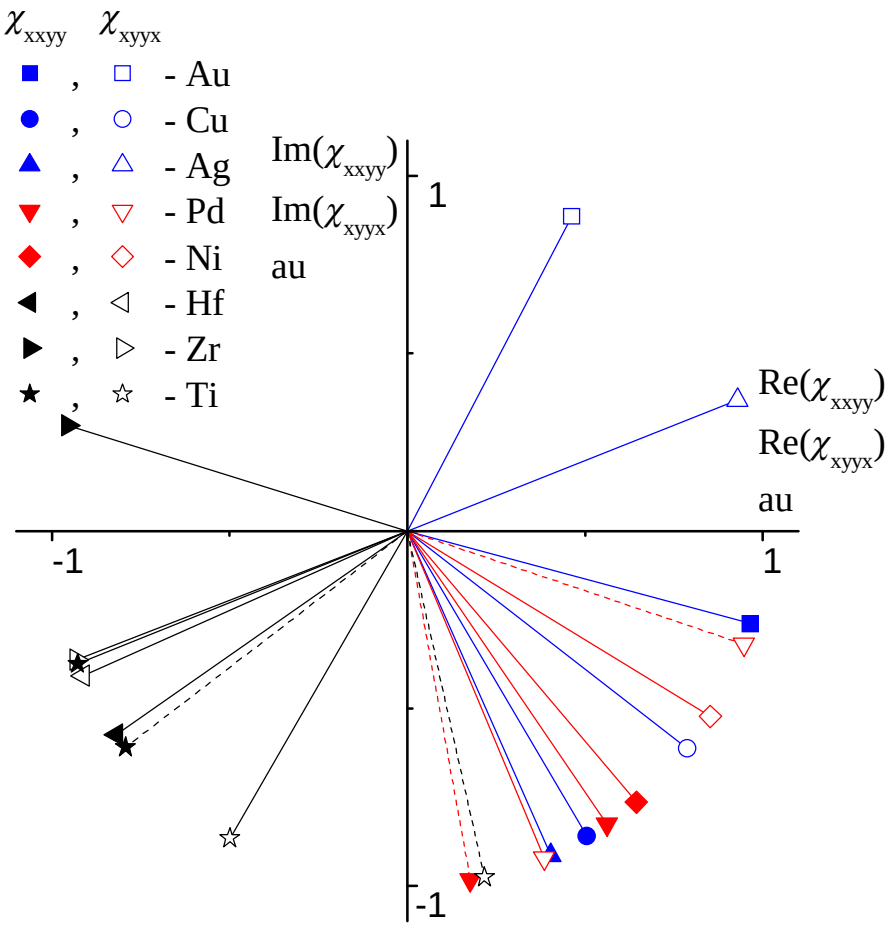

Figure 5.9 The complex components χ_{xxyy} (filled symbols) and χ_{xyyx} (open symbols) of $\chi^{(3)}$ extracted using equations (1.2.14)-(1.2.16) are plotted on the complex plane for different samples. The same symbols and line styles are used as in Figure 5.8.

defined if less distinct groups. However, it should be noted that large percentage errors may occur in values that have been calculated from the difference of two measured quantities.

5.4.4 Analysis and Significance of the Results

Let us now discuss the precision and consistency of the measurements by considering two consequences of equations (1.2.14) and (1.2.15). Firstly, the SOKE

contributions extracted from measurements with an elliptically polarised pump in geometry 1 and shown in Figure 5.7 should be the same as the SOKE signals measured in experiments with a linearly polarised pump in geometry 2 for ψ=45°, since the pump intensity in the latter experiments was half of that in the former case. In order to increase the signal-to-noise ratio, the SOKE signals measured in geometry 2 and shown in Figure 5.3 and Figure 5.4 were averaged with a weighting factor equal to $1/\sin 2\psi$. The averaged SOKE signals, which according to equation (1.2.15) are equivalent to the signals for ψ=45°, are shown in Figure 5.10. The fitted curves were obtained with the relaxation times values from Table 5.3, which were obtained from data in geometry 1,

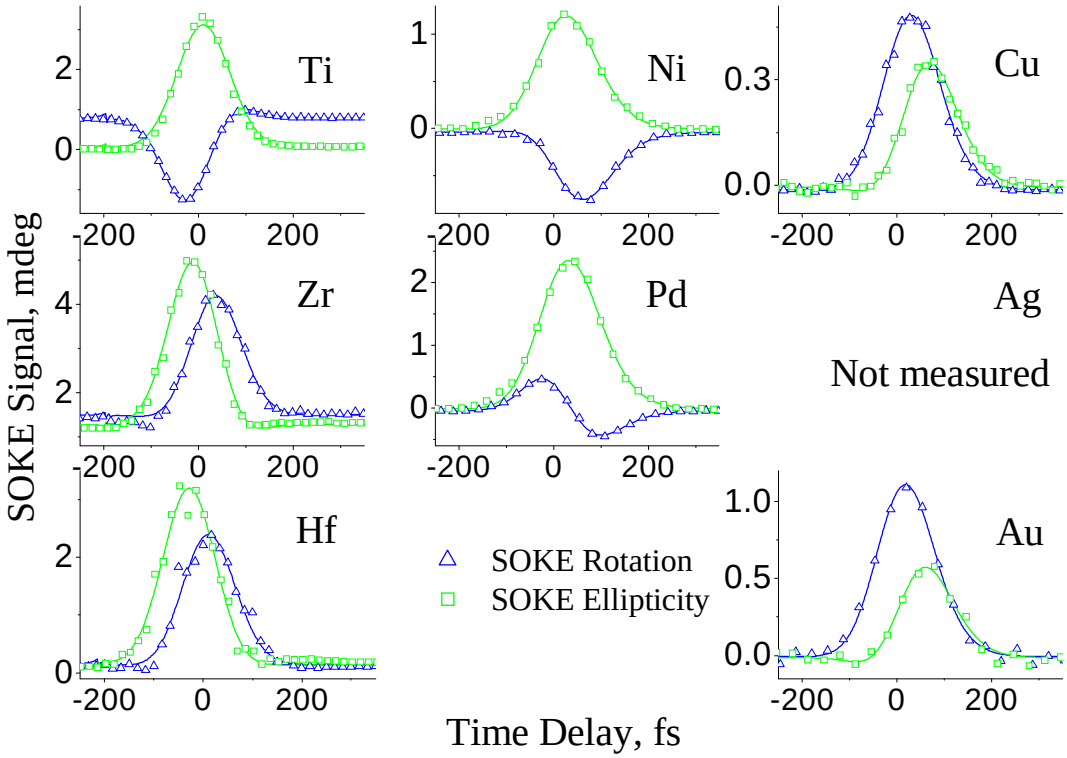

Figure 5.10 The average SOKE signals measured in geometry 2 are shown for different metals. The symbols represent data points, and the lines are fits to equation (5.3.33) using relaxation times from the data obtained in geometry 1.

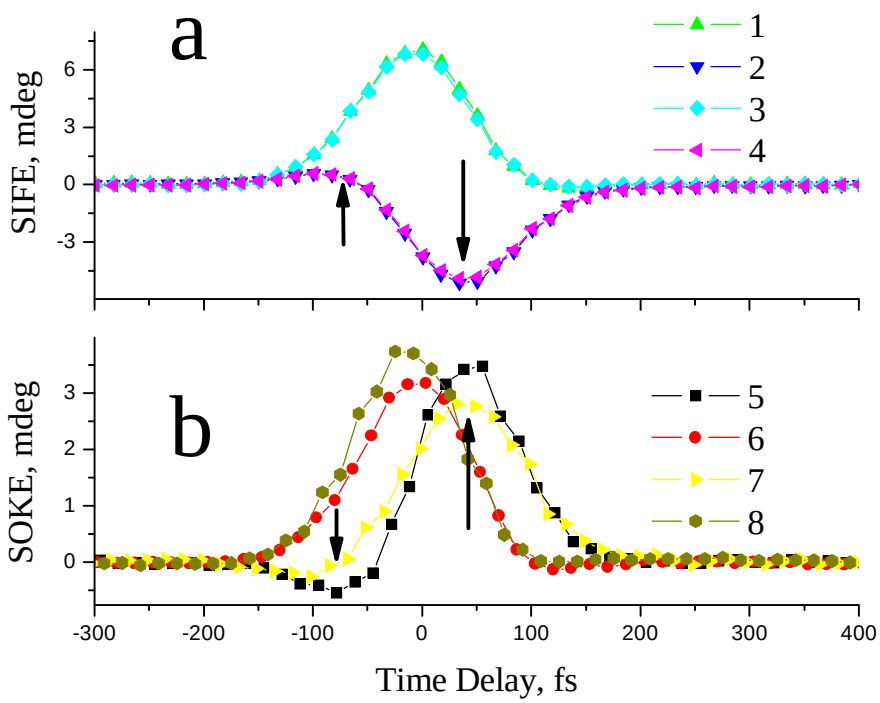

Figure 5.11 The consistency of the procedure described in the text for separating the SIFE and SOKE contributions to the signal is illustrated for Zr. Arrows point to the different peaks of the bipolar signals. a) Traces 1 and 2 are the SIFE rotation and ellipticity components, respectively, measured with a circularly polarized pump (e.g. for φ=±45°). Traces 3 and 4 are the SIFE rotation and ellipticity components, respectively, extracted from signals at φ=±22.5°,±67.5°. b) Traces 5 and 6 are the SOKE rotation and ellipticity components, respectively, extracted from signals at φ=±22.5°,±67.5°. Traces 7 and 8 are the SOKE rotation and ellipticity components, respectively, measured with a linearly polarized pump (e.g. for ψ=±45°).

and only the values of the amplitudes $A_{\theta(\eta),j}^{SIFE(SOKE)}$ in equation (5.3.33) were adjusted.

Secondly, as discussed before, the SIFE contributions extracted from measurements in geometry 1 as the sum of the signals at +22.5° and +67.5° (or -22.5° and -67.5°) divided by $\sqrt{2}$ should be the same (to a sign) as those measured at φ=±45°.

As a typical example, Figure 5.11 (a) illustrates a reassuring agreement between the Zr SIFE components measured with a circular pump ($\varphi = \pm 45°$) and those extracted by the procedure for separating the SOKE and SIFE that was described above. It also shows that the bipolarity of the signals is not an artefact induced by the method of analysis. The agreement between the SOKE contributions measured with a linear pump (geometry 2) and deduced from the measurements with an elliptical pump (geometry 1) is not quite as good. While the time delay between the rotation and ellipticity signals is the same, the bipolarity of the rotation is less pronounced in the measurements performed in geometry 2. The magnitudes of the SOKE signals differ by about 15% which provides a measure of the experimental error. The results of measurements in geometry 1 were used in the quantitative analysis above, since both the SIFE and SOKE components were present in the same signal in this case.

Equation (5.3.33) was found to provide a good description of the observed SIFE and SOKE signal. However, as one can see from Table 5.3, in cases where the percentage difference in the two fitted relaxation times for a particular effect was small (less than 10 per cent), the values of the two associated amplitudes were found to almost cancel and hence the errors in the fitted parameters were comparable to or larger than the parameter values. This indicates a possible degeneracy in the fit and suggests that a more accurate model or a shorter optical pulse width may be needed. Any such model must be based on a solution of the Boltzmann kinetic equations with realistic assumptions about the band structure and interactions among quasi-particles. Nevertheless, our model is the simplest capable of reproducing the shape of the observed signals, including those with the bipolar shape, and it reveals the characteristic time scales of the underlying dynamics.

5.5 Summary

In summary, femtosecond ellipsometric measurements performed with an elliptically polarised pump have been performed to directly investigate the decay of optically induced transient linear and circular polarisation in metals. The response of different metals has been shown to fall into groups that correspond to the positions of the metals within the periodic table. The non-vanishing components of the third-order optical susceptibility tensor $\chi^{(3)}$ have been extracted. A simple model has been introduced that successfully fits the shapes of the signals. In some cases two distinct relaxation times may be identified, that are interpreted in terms of scattering of the linear and angular momentum of the excited electrons. The values of the relaxation times may be important for understanding the transport in hot electron devices such as the spin valve transistor or magnetic tunnel transistor. The capability of this new technique could be further enhanced through the use of shorter pulses and by separately tuning the wavelength of pump and probe, so that the mechanisms responsible for linear and angular momentum relaxation in metals may be better explored and understood.

Chapter 6. Transient Temperature Dynamics

6.1 Introduction

The study of ultrafast electronic processes in metals by means of the optical pump-probe measurements has an almost twenty year history. In the pioneering work of Schoenlein et al.[137] a 100 nm Au film was investigated. The electron-lattice relaxation time was found to be 3 ps and 2 ps for pump beam fluences of 4 and 0.4 mJ/cm^2, respectively. These values were related to a rise of the electron heat capacity with increasing electron temperature. Elsayed-Ali et al.[138] studied a 20 nm Cu film in a transmission geometry and found that the electron-lattice relaxation time increased from 1 ps for a pump fluence of 1.4 mJ/cm^2 (8 nJ per pulse) to 4 ps for a pump fluence of 11.4 mJ/cm^2 (65 nJ per pulse). They also found that the amplitude of the transmissivity changed in proportion to the pump fluence. Groeneveld et al.[139] examined the response of a 45 nm Ag film near the surface plasmon resonance. By measuring on and off resonance, they were able to discriminate between heating of the lattice and the electrons. They found an electron-lattice relaxation time of 670 fs for a pump fluence of 0.0019 mJ/cm^2. Sun et al.[72] studied three gold films of thickness 20, 40, and 120 nm in the low perturbation limit. They observed the electron thermalisation time to be 0.5 ps far from, and 1-2 ps close to the Fermi level, and obtained an electron-lattice relaxation time of 1 ps. These time constants were independent of the pump power for fluences in the range of 2.5-200 μJ/cm^2. The reflectivity response of the thickest sample suggested the presence of ballistic electron transport.

The results of the first femtosecond pump-probe investigations of electron dynamics in metals were analysed by assuming a simple linear dependence of the

reflectivity signal upon the transient electron temperature, and the electron occupation number. This was in spite of the earlier thermo-modulation studies of the temperature dependence of reflectivity of metals[140] that suggested more complicated dependence. Most of the theoretical effort was devoted to the kinetics of electron thermalisation[70,120,141-144]. This approach turned out to be sufficiently productive that much information about the electron-phonon coupling constant and electron thermalisation time has now been gathered[7]. However, the investigations of Hohlfeld and co-workers[4,9] showed that a more realistic description of the temperature dependence of the metallic reflectivity may be essential for a correct interpretation of the experiments.

The aim of this chapter is to obtain an analytical solution of the two temperature model equations. The non-thermal electron dynamics are treated in the relaxation time approximation approach developed in the previous section. The solutions are used for fitting the measured reflectivity signals, and the characteristic relaxation times of the electron dynamics are extracted. In this thesis, no attempts have been made to rigorously account for the dependence of the sample reflectivity upon either the transient temperature or the sample band structure, and no firm interpretation of the extracted relaxation times is offered. Instead, the question of the relationship between the transient reflectivity and electron temperature is addressed experimentally through measurements of the transient reflectivity spectra in two colour pump-probe experiment.

6.2 Theory

6.2.1 Kinetic Equation in Relaxation Time Approximation

As discussed above, absorption of a pump pulse leads to the creation of a non-equilibrium population of hot electrons. The scattering among the hot electron population as well as from the phonons, defects etc., results in the creation of the equilibrium electron distribution described by the Fermi-Dirac function (1.2.12). In the two temperature model, it is assumed that electrons may be divided into two subsystems, one of which is in local equilibrium while the other is not. The details of the non-equilibrium state are neglected, although they may be very important, and both subsystems are characterized by the amount of excess energy obtained relative to the unperturbed state. The excess energy of the Fermi subsystem is equal to the product of the excess electron temperature ΔT_e and the electron heat capacitance C_e, which is in turn proportional to the transient electron temperature $T_e=T_0+\Delta T_e$, where T_0 is the ambient (unperturbed) temperature. The excess energy of the non-Fermi subsystem (per unit volume) is given by

$$\Delta E = \int_{\varepsilon_F}^{+\infty}(\varepsilon-\varepsilon_F)\gamma_e(\varepsilon)\zeta(\varepsilon)d\varepsilon + \int_{-\infty}^{\varepsilon_F}(\varepsilon_F-\varepsilon)\gamma_h(\varepsilon)\zeta(\varepsilon)d\varepsilon\,, \tag{6.2.1}$$

where $\gamma_{e,h}(\varepsilon)$ are the hot electron and hot hole occupation numbers, and $\zeta(\varepsilon)$ is the electron density of states. The kinetic equations for these non-Fermi occupation numbers in the relaxation time approximation are

$$\dot{\gamma}_e(\varepsilon) = -\frac{\gamma_e(\varepsilon)}{\tau_e(\varepsilon)} + \frac{I(\varepsilon,x,t)}{\zeta(\varepsilon)}\,, \tag{6.2.2}$$

for electrons, and

$$\dot{\gamma}_h(\varepsilon) = -\frac{\gamma_h(\varepsilon)}{\tau_h(\varepsilon)} + \frac{I(\varepsilon, x, t)}{\zeta(\varepsilon)}, \tag{6.2.3}$$

for holes, where $I(\varepsilon,x,t)$ is defined by (5.3.16) in (6.2.2) and by (5.3.17) in (6.2.3), and $\tau_e(\varepsilon)$ and $\tau_h(\varepsilon)$ are the electron and hole relaxation times. The latter depend upon energy ε as we discussed in the previous chapter. Let us multiply (6.2.2) by $\zeta(\varepsilon)(\varepsilon-\varepsilon_F)$ and (6.2.3) by $\zeta(\varepsilon)(\varepsilon_F-\varepsilon)$, integrate them with respect to energy over the interval from ε_F to $+\infty$ and from $-\infty$ to ε_F, respectively. Finally, adding the two integrals together we obtain

$$\begin{aligned}\Delta\dot{E} = &-\int_{\varepsilon_F}^{+\infty} \frac{(\varepsilon-\varepsilon_F)\gamma_e(\varepsilon)\zeta(\varepsilon)}{\tau_e(\varepsilon)} d\varepsilon - \int_{-\infty}^{\varepsilon_F} \frac{(\varepsilon_F-\varepsilon)\gamma_h(\varepsilon)\zeta(\varepsilon)}{\tau_h(\varepsilon)} d\varepsilon + \\ &+ \frac{2A_0S_0}{\sigma}\sqrt{\frac{\ln 2}{\pi}} \exp\left\{-\frac{x}{l_0} - \frac{4\ln 2(t-t_0)^2}{\sigma^2}\right\},\end{aligned} \tag{6.2.4}$$

where S_0 is a function of the pump photon frequency, given by equation (5.3.5).

We assume now that the first two terms in the right hand side of this equation can be reduced by

$$-\int_{\varepsilon_F}^{+\infty} \frac{(\varepsilon-\varepsilon_F)\gamma_e(\varepsilon)\zeta(\varepsilon)}{\tau_e(\varepsilon)} d\varepsilon - \int_{-\infty}^{\varepsilon_F} \frac{(\varepsilon_F-\varepsilon)\gamma_h(\varepsilon)\zeta(\varepsilon)}{\tau_h(\varepsilon)} d\varepsilon = -\frac{\Delta E}{\tau_{th}}, \tag{6.2.5}$$

where τ_{th} is the electron thermalisation time, which describes the "transport" of electrons from the non-Fermi to the Fermi subsystem. This thermalisation time is generally greater than the energy dependent relaxation times in (6.2.4), since the latter include additional contributions from elastic scattering processes. Also this definition of τ_{th} is rather arbitrary, as is the subdivision of electrons into the two subsystems.

Hence, we obtain the following equation describing the energy relaxation of the non-Fermi electron population

$$\Delta\dot{E} = -\frac{\Delta E}{\tau_{th}} + \frac{2A_0S_0}{\sigma}\sqrt{\frac{\ln 2}{\pi}} \exp\left\{-\frac{x}{l_0} - \frac{4\ln 2(t-t_0)^2}{\sigma^2}\right\}. \tag{6.2.6}$$

This equation has the form of equations (5.3.18)-(5.3.21) from the previous chapter and can be solved in the same way, giving

$$\Delta E(x,t) = \frac{A_0 S_0 \exp\left\{-\frac{x}{l_0} + \frac{\sigma^2}{16\tau_{th}^2 \ln 2} - \frac{t-t_0}{\tau_{th}}\right\}}{2} \times \\ \times\left(1 + erf\left(\frac{2\sqrt{\ln 2}(t-t_0)}{\sigma} - \frac{\sigma}{4\tau_{th}\sqrt{\ln 2}}\right)\right), \tag{6.2.7}$$

Let us represent the thermalisation rate as

$$\frac{1}{\tau_{th}} = \frac{1}{\tau_{e-e}} + \frac{1}{\tau_{e-ph}}, \tag{6.2.8}$$

where $\tau_{\text{e-e}}$ and $\tau_{\text{e-ph}}$ are the electron-electron and hot electron-phonon thermalisation times, respectively. Also, because the pump spot size in our experiments is much greater than the film thickness, the transient temperature gradient in the direction normal to the film surface is much greater than that within the film plane. Hence, we can neglect heat transport in the lateral direction. Finally, we neglect the heat transport by the lattice, since this is a much slower process than the diffusive electron heat transport in metals, and the heat exchange between the electron and phonon subsystems. Hence, we rewrite the two temperature model equations as

$$C_{\text{e}} \frac{\partial T_{\text{e}}}{\partial t} = -G(T_{\text{e}} - T_{\text{l}}) + \frac{\partial}{\partial x}\left(\kappa_{\text{e}} \frac{\partial T_{\text{e}}}{\partial x}\right) + \frac{\Delta E(x,t)}{\tau_{e-e}}, \tag{6.2.9}$$

$$C_{\text{l}} \frac{\partial T_{\text{l}}}{\partial t} = G(T_{\text{e}} - T_{\text{l}}) + \frac{\Delta E(x,t)}{\tau_{e-ph}}. \tag{6.2.10}$$

Let us consider the boundary conditions for the electron temperature at the film surfaces. Since there is no heat transport through the front surface

$$\left.\frac{\partial T_{\text{e,l}}}{\partial x}\right|_{x=0} = 0. \tag{6.2.11}$$

The processes at the interface between the film and its substrate are more complicated, and generally one has to consider heat propagation in the latter. However, we neglect the thermal resistance of the interface and assume that the film temperature at the interface is equal to that of the substrate, while the latter always remains at the ambient temperature

$$T_{\mathrm{e,l}}\big|_{x=d} = T_0\,, \tag{6.2.12}$$

where d is the film thickness. This may be justified for samples grown on Si, since Si has very high heat conductivity of 148 W/(m·K) and capacitance of 702 J/(kg·K). For example, these numbers respectively are 71.8 W/(m·K) and 246 J/(kg·K) for Pd, i.e. a few times smaller. This assumption is also supported by the fact that the substrates are about 1 mm thick, i.e. at least three orders of magnitude greater then the film thickness. Hence, the film substrate serves as heat reservoir in our experiments. However, we must note that these assumptions might not be valid for the noble metals, as their thermal conductivity is very large.

6.2.2 Analytical Solution of the Two Temperature Model Equations in the Low Perturbation Limit

Generally, these equations can be solved numerically. Here, we consider two limiting cases in which an analytical solution can be obtained. In the first, we neglect the dependence of the material parameters upon the electron temperature. This can be justified in the low perturbation limit where the excess electron temperature ΔT_{e} is small compared to the ambient temperature. The material parameters depend upon the number of Fermi electrons, and hence also upon the number of non-Fermi electrons. This dependence can be neglected in the low perturbation limit. Then equations (6.2.9)-(6.2.10) represent a system of coupled inhomogeneous linear differential equations of second order with constant coefficients. Such a system may be solved by first

considering a complimentary system that has the same form but without the source terms.

The general solutions of the complimentary system $T_{e,h}(t,x)$ and $T_{l,h}(t,x)$ are found by seeking solutions of the form $T_{e,h}(t,x)=\Theta_e(t)X(x)$, $T_{l,h}(t,x)=\Theta_l(t)X(x)$, and solving the eigenvalue problem for $X(x)$ using the boundary conditions (6.2.11) and (6.2.12). Such a factorisation is possible under the assumption that the lattice heat transport is much slower than both the diffusive electron heat transport and the heat exchange between the electron and phonon subsystems. In this case, the lattice temperature profile follows that of the electron temperature. The result of the calculation is

$$T_{e,h}(x,t) = T_0 + \sum_{n=0}^{\infty}\left(A_n \exp(-\alpha_n t) + B_n \exp(-\beta_n t)\right)\cos(k_n x), \tag{6.2.13}$$

$$T_{l,h}(x,t) = T_0 + \sum_{n=0}^{\infty}\left(\begin{array}{l} A_n \dfrac{\kappa_e k_n^2 - \alpha_n C_e + G}{G}\exp(-\alpha_n t) + \\ + B_n \dfrac{\kappa_e k_n^2 - \beta_n C_e + G}{G}\exp(-\beta_n t)\end{array}\right)\cos(k_n x), \tag{6.2.14}$$

where the wave numbers of the spatial harmonics are given by

$$k_n = \frac{\pi}{d}\left(\frac{1}{2}+n\right), \tag{6.2.15}$$

and the corresponding relaxation rates are given by

$$\alpha_n, \beta_n = \frac{G(C_e + C_l) + \kappa_e k_n^2 C_l \mp \sqrt{G^2(C_e + C_l)^2 + \kappa_e^2 k_n^4 C_l{}^2 + 2\kappa_e k_n^2 C_l G(C_l - C_e)}}{2C_e C_l}, \tag{6.2.16}$$

where A_n and B_n are arbitrary constants, determined from initial conditions.

In order to solve the inhomogeneous problem, we must decompose the spatial prefactor of the source term in (6.2.7) into the spatial harmonics of the homogeneous solution, i.e.

$$\exp\left(-\frac{x}{l_0}\right) = \sum_{n=0}^{\infty} a_n \cos(k_n x), \tag{6.2.17}$$

where

$$a_n = \frac{2\delta}{1+\pi^2\delta^2\left(\frac{1}{2}+n\right)^2}\left(1+(-1)^n\pi\delta\left(\frac{1}{2}+n\right)e^{-\delta}\right), \tag{6.2.18}$$

and $\delta=l_0/d$. As in the case of the transient polarisation, we may crudely account for the ballistic electron transport, by substituting by l_0+l_{bal} for l_0, where l_{bal} is the ballistic range[9]. Then, we obtain the solution by allowing the constants A_n and B_n in (6.2.13) and (6.2.14) to become functions of time, and substituting the modified homogeneous solutions (6.2.13) and (6.2.14) into the original inhomogeneous equations. The functions $A_n(t)$ and $B_n(t)$ are determined by direct integration of the first order ordinary differential equations obtained from the requirement that equation (6.2.9) is satisfied for each harmonic separately. Equation (6.2.10) is always satisfied by (6.2.14), since it does not contain spatial derivatives. The necessary initial condition is that the transient electron temperature must be equal to the ambient temperature at a sufficiently large negative time delay. We then obtain

$$\Delta T_{e,l}(x,t) = \frac{A_0 S_0}{2C_e}\sum_{n=0}^{\infty}\Theta_{e,l}^n(t)\cos(k_n x), \tag{6.2.19}$$

where

$$\Theta_{e,l}^n(t) = \frac{a_n}{\beta_n-\alpha_n}\left(\begin{array}{l} q_{e,l}^n\left\{1+erf\left(\frac{2\sqrt{\ln 2}(t-t_0)}{\sigma}-\frac{\sigma\beta_n}{4\sqrt{\ln 2}}\right)\right\}\exp\left(-\beta_n(t-t_0)\right)- \\ -r_{e,l}^n\left\{1+erf\left(\frac{2\sqrt{\ln 2}(t-t_0)}{\sigma}-\frac{\sigma\alpha_n}{4\sqrt{\ln 2}}\right)\right\}\exp\left(-\alpha_n(t-t_0)\right)- \\ -s_{e,l}^n\left\{1+erf\left(\frac{2\sqrt{\ln 2}(t-t_0)}{\sigma}-\frac{\sigma}{4\tau_{th}\sqrt{\ln 2}}\right)\right\}\exp\left(-\frac{t-t_0}{\tau_{th}}\right) \end{array}\right), \tag{6.2.20}$$

$$q_e^n = \frac{\dfrac{\kappa_e k_n^2 - \alpha_n C_e + G}{C_e \tau_{e-e}} - \dfrac{G}{C_l \tau_{e-ph}}}{\dfrac{1}{\tau_{th}} - \beta_n} \exp\left(\frac{\sigma^2 \beta_n^{\,2}}{16 \ln 2} \right), \tag{6.2.21}$$

$$r_e^n = \frac{\dfrac{\kappa_e k_n^2 - \beta_n C_e + G}{C_e \tau_{e-e}} - \dfrac{G}{C_l \tau_{e-ph}}}{\dfrac{1}{\tau_{th}} - \alpha_n} \exp\left(\frac{\sigma^2 \alpha_n^{\,2}}{16 \ln 2} \right), \tag{6.2.22}$$

$$s_e^n = \frac{(\beta_n - \alpha_n)\left(\dfrac{1}{\tau_{th}\tau_{e-e}} - \dfrac{\alpha_n + \beta_n}{\tau_{e-e}} + \dfrac{\kappa_e k_n^2 + G}{C_e \tau_{e-e}} - \dfrac{G}{C_l \tau_{e-ph}} \right)}{\left(\dfrac{1}{\tau_{th}} - \beta_n \right)\left(\dfrac{1}{\tau_{th}} - \alpha_n \right)} \exp\left(\frac{\sigma^2}{16 \tau_{th}^2 \ln 2} \right), \tag{6.2.23}$$

$$q_l^n = \frac{\left(\dfrac{\kappa_e k_n^2 - \alpha_n C_e + G}{C_e \tau_{e-e}} - \dfrac{G}{C_l \tau_{e-ph}} \right)\left(\kappa_e k_n^2 - \beta_n C_e + G \right)}{\left(\dfrac{1}{\tau_{th}} - \beta_n \right) G} \exp\left(\frac{\sigma^2 \beta_n^{\,2}}{16 \ln 2} \right), \tag{6.2.24}$$

$$r_l^n = \frac{\left(\dfrac{\kappa_e k_n^2 - \beta_n C_e + G}{C_e \tau_{e-e}} - \dfrac{G}{C_l \tau_{e-ph}} \right)\left(\kappa_e k_n^2 - \alpha_n C_e + G \right)}{\left(\dfrac{1}{\tau_{th}} - \alpha_n \right) G} \exp\left(\frac{\sigma^2 \alpha_n^{\,2}}{16 \ln 2} \right), \tag{6.2.25}$$

$$s_l^n = (\beta_n - \alpha_n) \times$$
$$\times \frac{\left(\dfrac{\left(\kappa_e k_n^2 - C_e \alpha_n + G \right)\left(\kappa_e k_n^2 - C_e \beta_n + G \right)}{C_e G \tau_{th}} + \dfrac{C_e - G\tau_{th}}{C_l \tau_{th} \tau_{e-ph}} \right)}{\left(\dfrac{1}{\tau_{th}} - \beta_n \right)\left(\dfrac{1}{\tau_{th}} - \alpha_n \right)} \exp\left(\frac{\sigma^2}{16 \tau_{th}^2 \ln 2} \right), \tag{6.2.26}$$

It is easy to show that the series (6.2.19) converges. To be a rigorous solution of the problem, (6.2.19) must also have convergent and differentiable derivatives. The proof of this latter condition is a much more difficult task. In practice, it is necessary only to retain a finite number of terms in (6.2.19) to obtain an approximate solution to the general problem. The solution is however exact if the spatial prefactor of the source term in (6.2.7) consists of a superposition of a finite number of the harmonic

eigenfunctions in (6.2.17). We must therefore approximate the source term with a finite expansion of harmonic eigenfunctions so that the exact solution may be applied. This approximate representation of the spatial profile of the injected pump energy is illustrated in Figure 6.1 for two Au films with thicknesses of 28.1 nm and 1 μm, assuming parameters from Ref. 9. In particular, one can see that in the case of the 1 μm film retention of just five terms on the right hand side of (6.2.17) can provide a reasonable representation of the source term on the left hand side. For the 28.1 nm film,

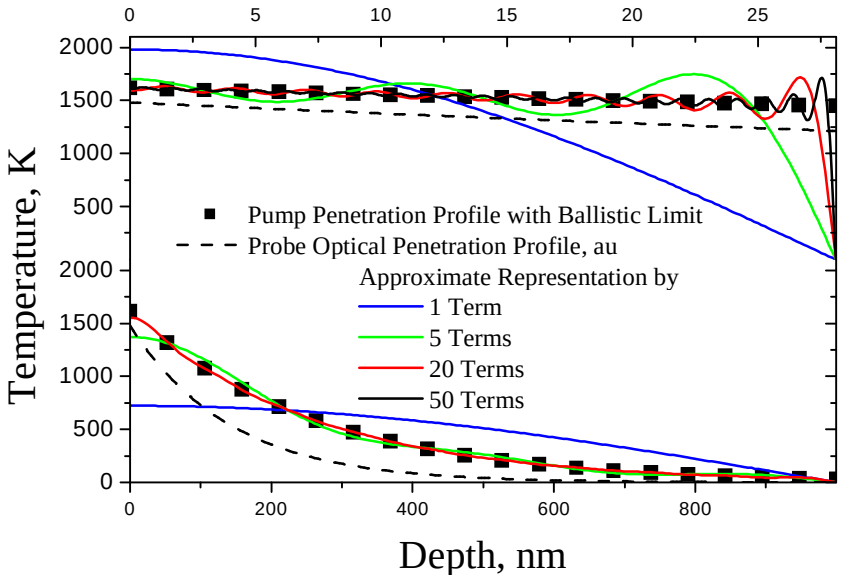

Figure 6.1 The approximate representation of the spatial profile of the injected pump energy is illustrated (in temperature units) for Au films with thicknesses of 28.1 nm (upper set of curves) and 1 μm (lower set of curves). The symbols correspond to the spatial profile given by the left hand side of equation (6.2.17) in which l_0 is equal to the sum of the optical skin depth of 141 nm and the ballistic range of 117 nm. The curves were calculated by retaining a finite number of terms from the right hand side. The dashed lines represent the spatial profile of the optical probe, given by the left hand side of equation (6.2.17) after setting l_0 equal to the optical skin depth.

more terms are required to obtain a good agreement. However, in this case the temperature distribution is virtually uniform across the film thickness, and so the transport term in equation (6.2.9) can be neglected. The solution of the problem in this case will be given in the next section.

Within the linear approximation, the contribution to the signal due to a change in either the electron or lattice temperature is proportional to the convolution of the function (6.2.19) with the spatio-temporal profile of the probe pulse

$$S_{e,l}(t_d) \propto \int_0^d dx \int_{-\infty}^{\infty} dt \left\{ \Delta T_{e,l}(x,t) \frac{2}{\sigma d} \sqrt{\frac{\ln 2}{\pi}} \exp\left\{ -\frac{x}{l_0} - \frac{4 \ln 2 (t - t_1)^2}{\sigma^2} \right\} \right\}, \qquad (6.2.27)$$

where $t_d = t_1 - t_0$ is the time delay between the pump and probe pulses. The integration with respect to time is equivalent to substitution of σ by $\sigma\sqrt{2}$, and the integration with respect to x is equivalent to multiplying each term in the right hand side of (6.2.19) by $a_n/2$, where a_n is given by (6.2.18). Note that in this case the parameter l_0 in a_n is strictly equal to the optical skin depth.

Similarly, the contribution to the signal from the non-Fermi electron population, is proportional to the convolution of function (6.2.7) with the probe pulse spatio-temporal profile

$$S_{\text{hot}}(t_d) \propto \int_0^d dx \int_{-\infty}^{\infty} dt \left\{ \Delta E(x,t) \frac{2}{\sigma d} \sqrt{\frac{\ln 2}{\pi}} \exp\left\{ -\frac{x}{l_0} - \frac{4 \ln 2 (t - t_1)^2}{\sigma^2} \right\} \right\}. \qquad (6.2.28)$$

The integration with respect to time is again equivalent to substitution of σ by $\sigma\sqrt{2}$, and the integration with respect to x simply scales the entire function. In fact, integrals (6.2.27) and (6.2.28) represent an average of the signal over the volume of the film with a weighting factor given by the optical penetration profile of the probe, shown in Figure 6.1 by the dashed lines.

Figure 6.2 presents the electron and lattice temperatures calculated from equations

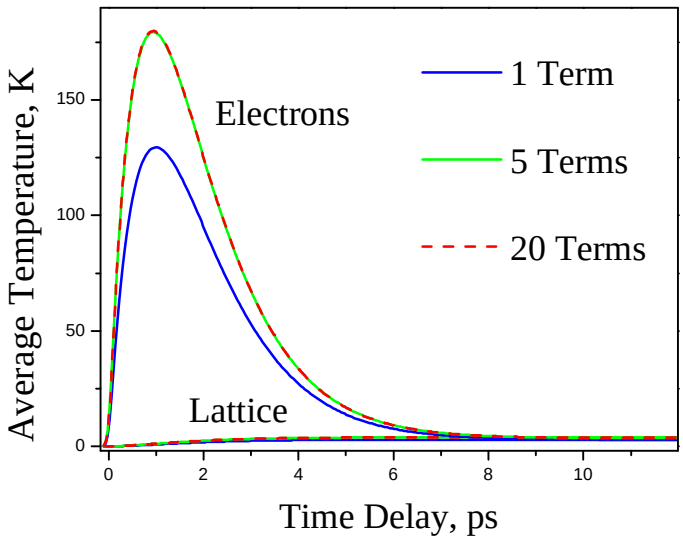

Figure 6.2 The simulated average transient electron and lattice temperatures are shown for the 1 μm thick Au film. The different curves correspond to approximate solutions given by retention of a finite number of terms in the right hand side of equation (6.2.19).

(6.2.19)-(6.2.26) and averaged by (6.2.27) for the 1 μm Au film. We used the parameter values for Au given in Ref. 9 and the pulse parameters characteristic of our experiment. One can see that the solutions given by retention of five and twenty terms in (6.2.19) are virtually identical, suggesting that just a few terms may be sufficient for fitting the experimental data. The electron and lattice temperatures have very different behaviour initially, but converge at longer time delays. It is interesting to note that the average electron temperature in this case is about an order of magnitude lower than the electron temperature at the surface of the film in Figure 6.1. This is due to the finite pulse duration and the electron thermalisation time, heat exchange between the electrons and the lattice, and heat transport into the bulk of the film. These processes were taken into account in Figure 6.2, while in Figure 6.1 instantaneous deposition of energy into

the system was assumed. The non-Fermi electron contribution has a temporal form similar to that shown in Figure 5.6, but with a longer relaxation time in the general case.

The transient reflectivity response may contain contributions from the Fermi electrons, the lattice temperature, and the hot electron population. As one can see from equations (6.2.7) and (6.2.19), all three contributions may be expressed as a linear superposition of the same functions. Hence, the reflectivity response will consist of the same functions. However, the relative weights of the different functions will be different from those predicted by (6.2.19). Hence, we will use the following form in the fitting the experimental data

$$\frac{\delta R}{R} \propto \frac{1}{2}\sum_{j=1}^{N} A_j \left(1 + erf\left(\frac{t_d\sqrt{2\ln 2}}{\sigma} - \frac{\sigma}{2\tau_j\sqrt{2\ln 2}}\right)\right)\exp\left\{-\frac{t_d}{\tau_j}\right\}, \qquad (6.2.29)$$

which is similar to equation (5.3.33) used in the previous chapter. Here $\delta R/R$ is the fractional change of the sample reflectivity; A_j and τ_j are the amplitudes and relaxation times of the different contributions to the signal; and the number of contributions N will be set to the smallest value for which a reasonable fit to the data can be obtained. Because of the strongly nonlinear dependence of the reflectivity upon the electron temperature, illustrated in Figure 1.9, the assumed proportionality between the transient reflectivity and the transient temperature can be justified only in the low perturbation limit.

According to equation (6.2.16), the relaxation times that describe the signal generally have a mixed character and depend upon both the electron-phonon coupling constant and the thermal conductivity. This makes it difficult to interpret the relaxation times observed within the experiment. However, it is common within the literature to ascribe relaxation times of a few picoseconds to electron-phonon scattering, and relaxation times of the order of nanoseconds to the thermal conduction from the optically probed region.

6.2.3 Analytical Solution of the Two Temperature Model Equations in the High Perturbation Limit

In the high perturbation limit, one must take into account the linear dependence of the electronic heat capacity upon the transient temperature, i.e. $C_e=A_eT_e$. Other simplifying assumptions can then be made. Let us assume that the lattice temperature remains constant during the experiment $T_l=T_l^*$, so that we need to consider only the transient electron temperature. This is justified because the heat capacity of the lattice is usually much greater than that of the electrons, and so the change in the temperature of the lattice is much smaller than that of the electrons. Let us also consider time scales longer than the electron-electron thermalisation time but shorter than the characteristic time for the heat transport. We may then rewrite equation (6.2.9) as

$$A_eT_e\frac{\partial T_e}{\partial t}=-G(T_e-T_l). \tag{6.2.30}$$

Applying the initial condition $\Delta T_e(t_0)=\Delta T_{e,max}$, direct integration yields the solution

$$t-t_0=-\frac{A}{G}\left(T_e-T_{e,\max}+T_0\ln\frac{T_e-T_0}{T_{e,\max}-T_0}\right), \tag{6.2.31}$$

where the first term dominates at short time delays, for large perturbations when $T_e\approx T_{e,max}$, and the second term dominates at long time delays, for small perturbations when $T_e\approx T_0$.

On the other hand, if the thermal conductivity is neglected, equations (6.2.9)-(6.2.10) may be integrated to yield

$$\Delta T_e(t) = \frac{A_0 S_0(E)\exp\left(-\dfrac{x}{l_0}\right)}{2\left(C_l + C_e\right)} \times \left(\begin{array}{l} \left\{1 + erf\left(\dfrac{2\sqrt{\ln 2}\left(t-t_0\right)}{\sigma}\right)\right\} \\ + q\left\{1 + erf\left(\dfrac{2\sqrt{\ln 2}\left(t-t_0\right)}{\sigma} - \dfrac{\sigma\gamma}{4\sqrt{\ln 2}}\right)\right\}\exp\left(-\gamma\left(t-t_0\right)\right) \\ - s\left\{1 + erf\left(\dfrac{2\sqrt{\ln 2}\left(t-t_0\right)}{\sigma} - \dfrac{\sigma}{4\tau_{th}\sqrt{\ln 2}}\right)\right\}\exp\left(-\dfrac{t-t_0}{\tau_{th}}\right) \end{array} \right), \tag{6.2.32}$$

where

$$q = \frac{\dfrac{C_l}{C_e\tau_{e-e}} - \dfrac{1}{\tau_{e-ph}}}{\dfrac{1}{\tau_{th}} - \gamma}\exp\left(\frac{\sigma^2\gamma^2}{16\ln 2}\right), \tag{6.2.33}$$

$$s = \frac{\dfrac{1}{\tau_{e-e}}\left(1 + \dfrac{C_l}{C_e}\right) - \gamma}{\dfrac{1}{\tau_{th}} - \gamma}\exp\left(\frac{\sigma^2}{16\tau_{th}^2\ln 2}\right), \tag{6.2.34}$$

and the pure electron-phonon relaxation rate is given by

$$\gamma = \frac{G\left(C_e + C_l\right)}{C_e C_l}. \tag{6.2.35}$$

Let us now analyse the asymptotic behaviour of solutions (6.2.31) and (6.2.32) for time delays sufficiently long that the difference between the transient electron and lattice temperatures is already very small, yet short enough that we can still neglect diffusive heat transport. For this time interval, we obtain from (6.2.31)

$$T_e(t) \approx T_0 + \left(\left(T_{e,\max} - T_0\right)\exp\left(\frac{T_{e,\max} - T_0}{T_0}\right)\right)\exp\left(-\frac{G}{AT_0}\left(t - t_0\right)\right), \tag{6.2.36}$$

and from (6.2.32)

$$T_e(x,t) \approx T_{equ} + \left(\frac{A_0 S_0(E) q \exp\left(-\frac{x}{l_0}\right)}{C_l + C_e} \exp\left(\frac{\sigma^2 \gamma^2}{16 \ln 2}\right) \right) \exp\left(-\gamma\left(t - t_0\right)\right), \qquad (6.2.37)$$

where the final electron-lattice equilibration temperature is given by

$$T_{equ} = T_0 + \frac{A_0 S_0(E) \exp\left(-\frac{x}{l_0}\right)}{C_l + C_e}. \qquad (6.2.38)$$

By comparing these two expressions, it is easy to construct a function that approaches (6.2.31) at short time delays, where the excess electron temperature is very high and the temperature dependence of the electron heat capacitance cannot be neglected, but which also has the correct behaviour, described by (6.2.32), at longer time delays where the low perturbation solution is a good approximation. This may be done by substituting T_{equ} for T_0, and the relaxation rate $\frac{G}{AT_0}$ for γ into (6.2.31). The result is

$$t - t_0 = -\frac{A}{G}\left(T_e - T_{e,\max}\right) - \frac{1}{\gamma} \ln \frac{T_e - T_{equ}}{T_{e,\max} - T_{equ}}. \qquad (6.2.39)$$

This equation describes an initial linear decay of the transient temperature in the high perturbation limit[9], which transforms into an exponential decay at longer time delays in the low perturbation limit. In order to fit the experimental data to this equation, we plot the time delay as a function of the reflectivity rather than the reflectivity as a function of the time delay. This can only work if the signal has a monotonic dependence upon time, and so the signals have to be cut at the point where they reach their maximum. The reflectivity response will be assumed to be proportional to the transient electron temperature. While this will be shown to be an oversimplification, a rigorous calculation of the dependence of the reflectivity upon the electron temperature using equations (1.2.11)-(1.2.13) is beyond the scope of this thesis.

6.3 Experimental Results and Discussion

6.3.1 Single Colour Measurements

Measurements were performed using the experimental setup described in section 2.1 of chapter 2. The samples were those discussed in the previous chapter (Table 5.1). The scan duration was adjusted for each sample so as to include the characteristic features of the reflectivity signal in each case. However, because of the low signal-to-noise ratio of the reflectivity response of the Ni and Ag films, we did not measure their reflectivity on longer time scales, where the signal was generally very weak. In order to improve the signal-to-noise ratio, the signals were averaged in a manner that will be discussed below. To facilitate comparison of the signal magnitudes, the average signals were normalised to the pump pulse energy, a value of 2 nJ, being typical for the measurements. All the averaged signals had the same temporal shape. The pump was circularly polarised unless otherwise indicated.

The reflectivity signals measured from the noble metal films are presented in Figure 6.3. The Cu reflectivity signal was obtained by averaging five scaled signals measured at pump pulse energies of 1.25, 1.5, 1.75, and 1.9 nJ (two). Three exponential contributions were required to fit the signal. The contribution with the shortest relaxation time of 46 fs had negative amplitude and is associated with the electron-electron thermalisation process. The relaxation time of 408 fs is associated with heat transfer between the electron and phonon systems, and is approximately half the value reported in Ref. 138 for a pump pulse energy of 8 nJ. This is reasonable in view of the dependence upon pump fluence observed in Ref. 138. The relaxation time of 840 ps is associated with diffusive heat transport into the bulk of the film.

The Ag reflectivity signal was obtained by averaging seven scaled signals measured at pump pulse energy of 1.75 nJ, corresponding to settings of the quarter wave

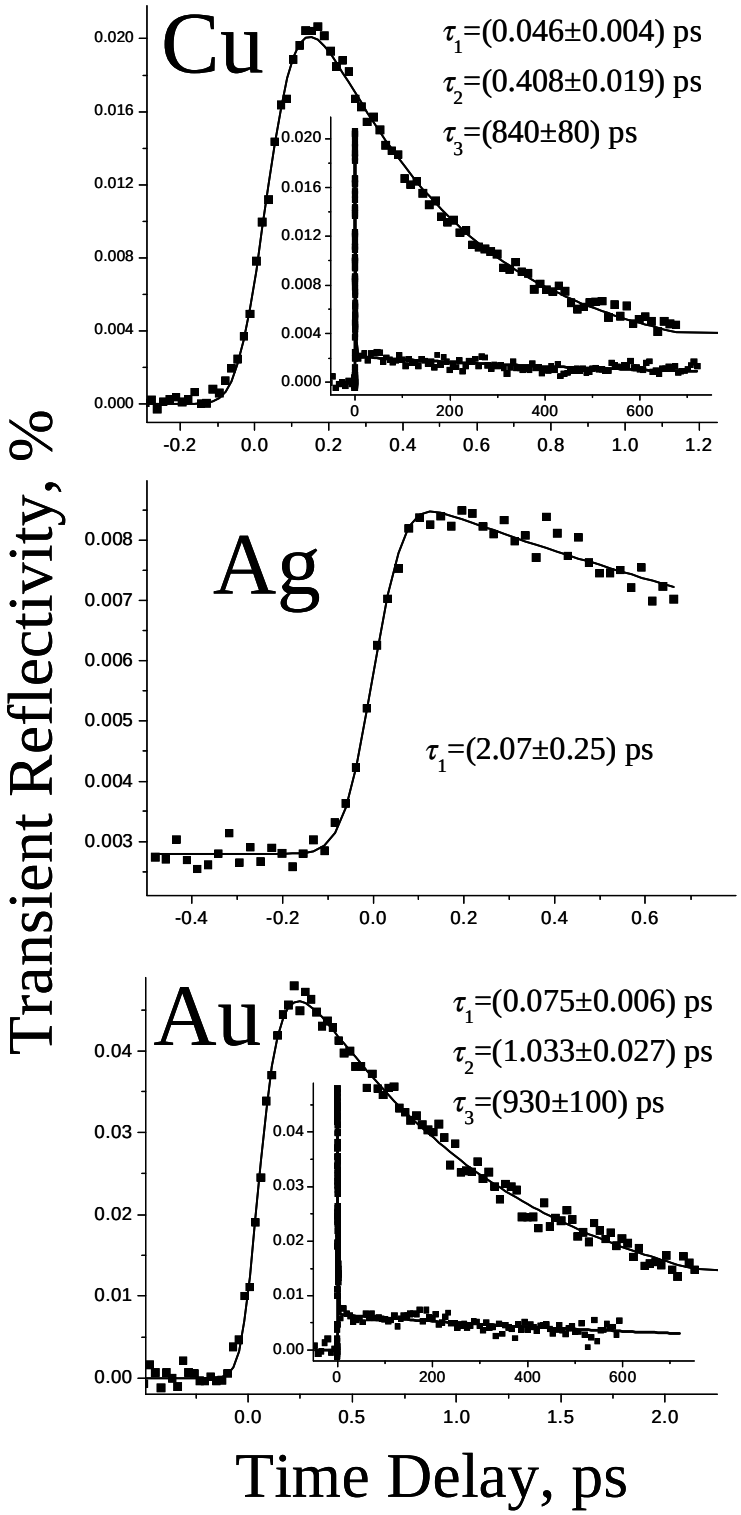

Figure 6.3 The transient reflectivity signals obtained from the noble metal films are presented. The symbols represent data points and the lines are fits to equation (6.2.29). The insets show the signals on a longer time scale. The values of the relaxation times obtained from the fits are also shown.

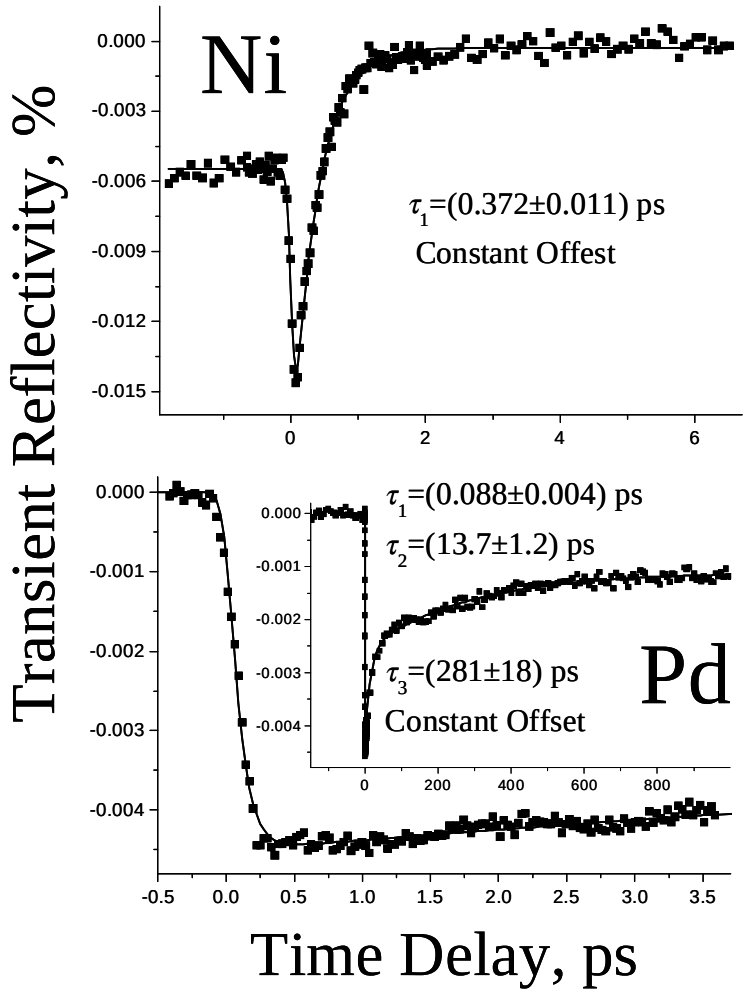

Figure 6.4 The transient reflectivity signals obtained from the Ni and Pd films are presented. The symbols represent data points and the lines are fits to equation (6.2.29). The insets show the signals on a longer time scale. The values of the relaxation times obtained from the fits are also shown.

plate orientation in geometry 1 of the previous chapter in the range of -67.5° to +67.5°. The extracted relaxation time of 2.07 ps cannot be reliably interpreted because of the short duration of the signal.

The Au reflectivity signal was obtained by averaging seven scaled signals measured at pump pulse energies of 1.25 (two), 1.5, 1.56, 1.75, 1.8 and 2 nJ. As in the case of Cu, three exponential contributions with relaxation times of 75 fs (negative),

1.033 ps, and 930 ps were required to fit the signal. The relaxation time of 1.033 ps closely matches the value reported in Ref. 72, where measurements were performed using low pump fluences.

Figure 6.4 presents the reflectivity response of Ni and Pd. As in the case of Ag, the Ni signal was obtained by averaging seven scaled signals measured at a pump pulse energy of 1.8 nJ, corresponding to a quarter wave plate orientation in geometry 1 of the previous chapter ranging from -67.5° to +67.5°. The extracted relaxation time of 372 fs is associated with the electron-phonon relaxation, while the effect of diffusive heat transport could not be resolved on this time scale, and instead gave rise to a constant offset. The latter was modelled by a term in equation (6.2.29) with a very long relaxation time of typically 10 ns.

The Pd reflectivity signal was obtained by averaging five scaled signals measured at pump pulse energies of 1.25, 1.5, 1.75, 2 and 2.25 nJ. Three exponential contributions with relaxation times of 88 fs, 13.7 ps, and 281 ps, and a constant offset were required to fit the signal. While the relaxation time of 88 fs is most likely to be associated with the electron-electron thermalisation process, the other two relaxation times may be associated with the combined action of the electron-phonon interaction and heat transport.

Figure 6.5 presents the reflectivity response of Ti and Hf. The Ti reflectivity signal was obtained by averaging five scaled signals measured at pump pulse energies of 1.25, 1.5, 1.75, 1.9 and 2 nJ. The Hf reflectivity signalwas obtained by averaging four signals measured at pump pulse energies of 1.25, 1.5, 1.75, and 2 nJ. In each case four exponential contributions were required to obtain a good fit. The initial sharp peak of Ti is described by relaxation times of 16, 54 (positive), and 80 fs. This suggests that the electron-electron and electron-phonon scattering take place on similar time scales. Behaviour of this kind cannot be reliably described by our model, and should instead be

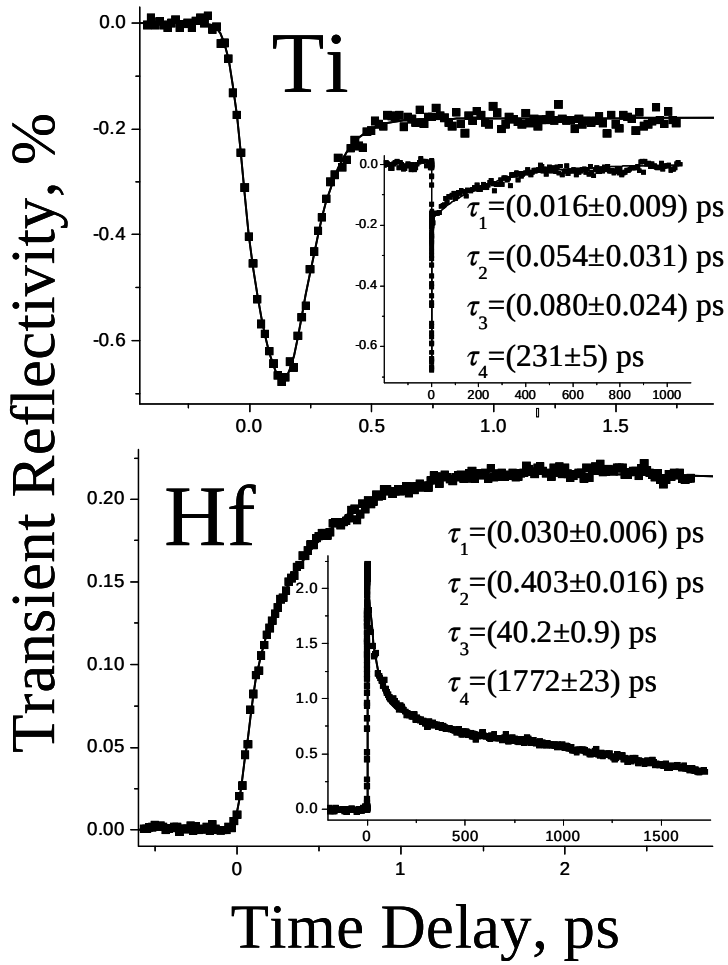

Figure 6.5 The transient reflectivity signals obtained from the Ti and Hf films are presented. The symbols represent data points and the lines are fits to equation (6.2.29). The insets show the signals on a longer timer scale. The values of the relaxation times obtained from the fits are also shown.

considered by a model, that takes into account the full details of the electron dynamics. The onset of the Hf reflectivity signal is gradual, and so the associated relaxation times of 30 and 403 fs are somewhat longer. While the latter can be interpreted as the electron-phonon relaxation time, the former seems to be too small to describe the electron-electron thermalisation within a transition metal. The relaxation times of

231 ps in Ti and 1772 ps in Hf are associated with heat transport, while the 40.2 ps relaxation time in Hf may also involve electron-phonon scattering.

The Zr reflectivity response presented in Figure 6.6 seems to be the most interesting example. The top and bottom panels represents signals acquired using a circularly and linearly polarised pump with energy of 2.25 nJ. Four scaled signals were averaged in the upper panel, while two scaled signals were averaged in the lower panel. One can see that the two signals differ through the presence of a sharp peak at short time delays. Although present in both signals, it is only visible in the signal when the pump and probe are polarised in the same plane. The peak is described by a relaxation time of 19 fs, and is associated with the transient linear dichroism induced by

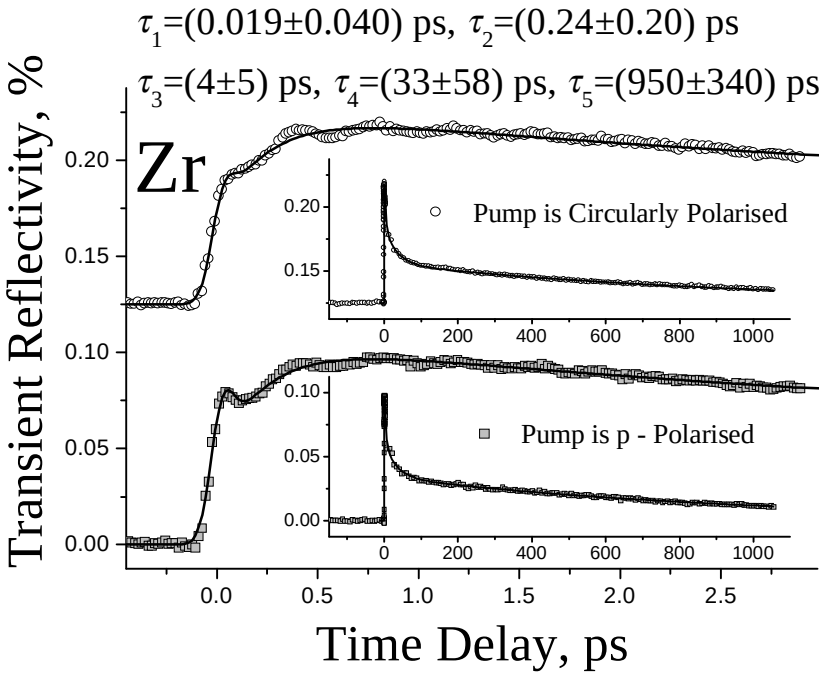

Figure 6.6 The transient reflectivity signal obtained from the Zr film is presented for the excitation with circularly (top panel) and linearly (bottom panel) polarised pump. The symbols represent data points and the lines are fits to equation (6.2.29). The insets show the signals on a longer timer scale. The values of the relaxation times obtained from the fits are also shown.

the pump pulse, an effect that was observed previously in Al[130]. The other four relaxation times are most likely associated with contributions of electron-phonon scattering and heat transport. As in the case of Al, the signal contains oscillations that sit on top of the multi-exponential shape. The frequency of the oscillations was extracted from a fast Fourier transform of the difference of the measured signal and the fitted curve, as shown in Figure 6.7. The extracted frequency of about 2.47 THz (9.7 meV) is much higher than the value of about 0.01 THz expected for the standing acoustic wave in a Zr film of this thickness. Therefore, the nature of the mode is different from that observed previously in Al. The frequency and amplitude of the oscillations are seen to be independent of the pump helicity. The observed mode is identified as the transverse-optical (TO) mode near the Γ-point of the Zr phonon

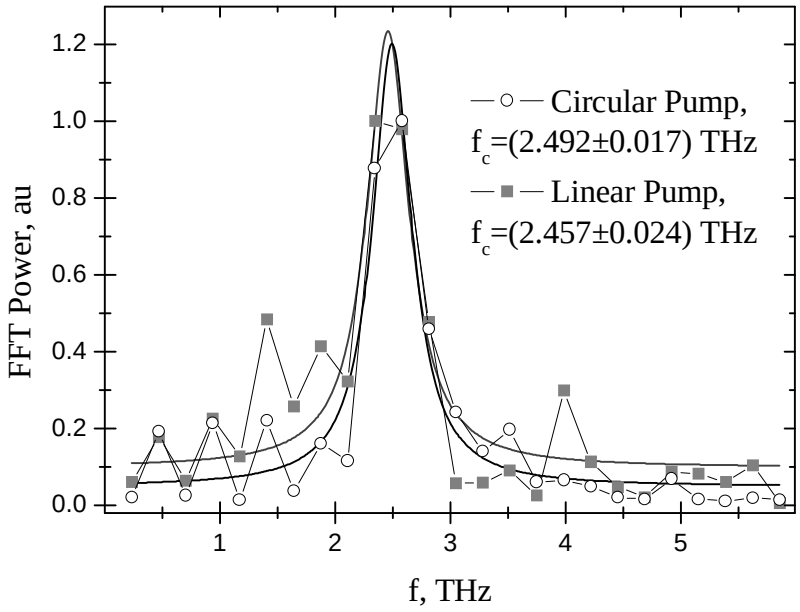

Figure 6.7 The Fourier spectra of the difference between the signals measured from the Zr film and the fits to equation (6.2.29) are presented for excitation with the circular and linear pump. The curves with and without symbols represent the data points and Lorentzian fits, respectively.

spectrum. The frequency of this mode was calculated to be 9.7 meV at 295 K in Ref. 145, while the inelastic neutron scattering measurements of Ref. 146 yielded a somewhat greater value of 10.59 meV at the same temperature. The discrepancy between the latter value and our measurements can be explained by the increased temperature in the pump-probe experiment, since the same neutron scattering experiments reported a value of 9.6 meV at 773 K.

There are several reasons why the observation of this mode is important. Firstly, the optical excitation of coherent optical phonons has been observed mostly in polymers, semiconductors, and semimetals. To the best of our knowledge, the only metal in which a coherent optical phonon has been excited is Gd[11]. Secondly, this is the first time that a transverse rather than longitudinal (LO) phonon has been observed. Thirdly, in Ref. 11 the oscillations were observed by the SHG technique, while the linear reflectivity response was "flat". Therefore, the mode observed in Ref. 11 was localised near the surface of the film, while the mode that we observed must have a significant amplitude within the bulk of the film. Fourth, our sample was sputtered, while an epitaxial film was studied in Ref. 11. Finally, this result has an important technological implication. It was argued in Ref. 11 that a coherent magnon of identical frequency can be excited by the phonon, although also localised near the film surface. Hence, our results suggests that high frequency magnetisation dynamics could be excited in the bulk of a ferromagnetic (or ferrimagnetic, or antiferromagnetic) sample that support the optical excitation of coherent optical phonons.

6.3.2 Two Colour Measurements

The measurements were performed using the experimental setup described in section 2.3 of chapter 2. The sample was the Au film studied in the previous chapter (Table 5.1). The reflectivity spectra acquired at different time delays are shown in

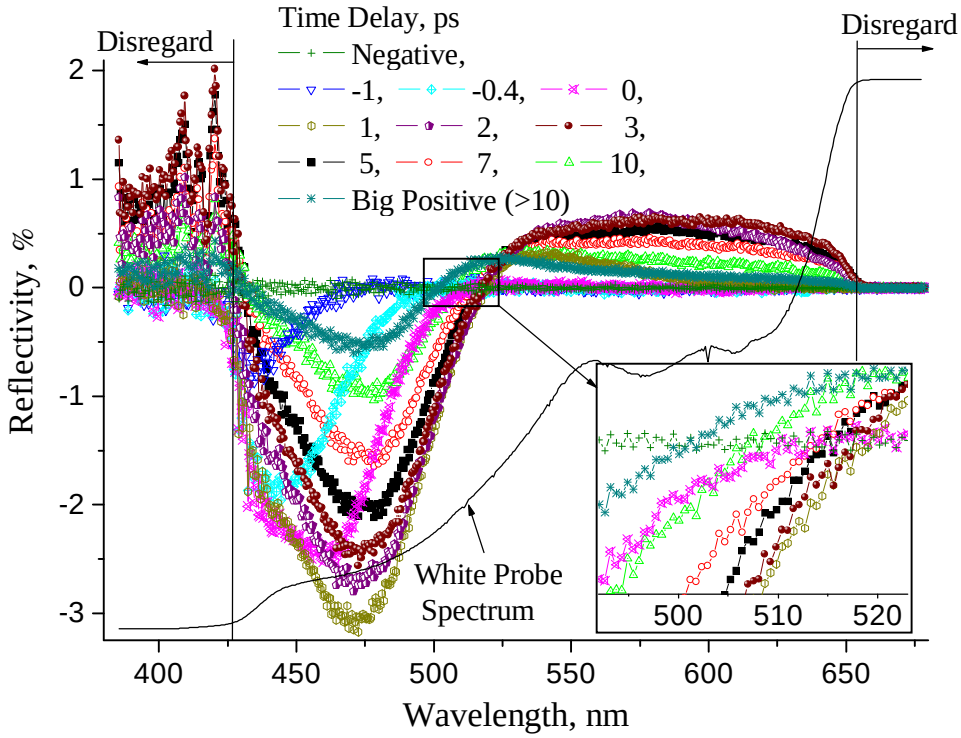

Figure 6.8 The transient reflectivity spectra obtained from the Au sample are shown for different pump-probe time delays. The inset shows the shift of the zero crossing point with time delay. The white light continuum spectrum is shown by the solid black line.

Figure 6.8. The spectrum of the white line continuum is shown on the same plot. For very short wavelengths (about 400 nm) the probe was too weak to produce meaningful results, while at very long wavelengths it was so strong that the detectors in the array were saturated. Hence, we will not consider the signal in these latter regions. At negative time delays, the signal vanishes over the entire spectral range as expected. At zero time delay, the signal appears first in the blue region and spans the entire range after approximately 2 ps. At later time delays, the shape of the signal is bipolar with a zero crossing point at a wavelength of about 510 nm. It is interesting to note that the position of the zero crossing point does not remain the same with changing time delay,

as shown in the inset of Figure 6.8. This point roughly corresponds to the interband transition threshold[9,72]. However, its precise position depends also upon details of the temperature and the wavelength dependence of the complex dielectric function of the sample. As the electron temperature decreases with time delay, the zero crossing point shifts towards shorter wavelengths, which is consistent with the calculations in Ref. 9 shown in Figure 1.9. In Ref. 72, calculations were performed that suggest that the same trend is instead due to the non-thermal electron subsystem. At present, we are not able to say which interpretation is more relevant to our observation. However, our data may help to identify the correct mechanism if a suitable model for the sample reflectivity is developed, since the spectra at different time delays can be analysed without invoking a model for the electron dynamics.

By averaging the signal over a wavelength range of a few tens of nanometres we were also able to construct time resolved reflectivity signals for different wavelengths, which are shown in Figure 6.9. While the shift of the onset of the signals is due to chirp of the probe pulse introduced by the water cell, their temporal shape also changes with the probe wavelength. In particular, the signal changes sign at a wavelength of 513 nm. The exponential decay of the signals was fitted to the solution of the two temperature model in the high perturbation limit (6.2.39), assuming firstly that the transient reflectivity is proportional to the electron temperature, and secondly a value of $71\ \frac{J}{m^3 K^2}$ for the constant A[9]. The fitted curves are shown in Figure 6.10. The fitting allowed us to extract values for the electron-phonon coupling constant and the electron-phonon equilibration temperature.

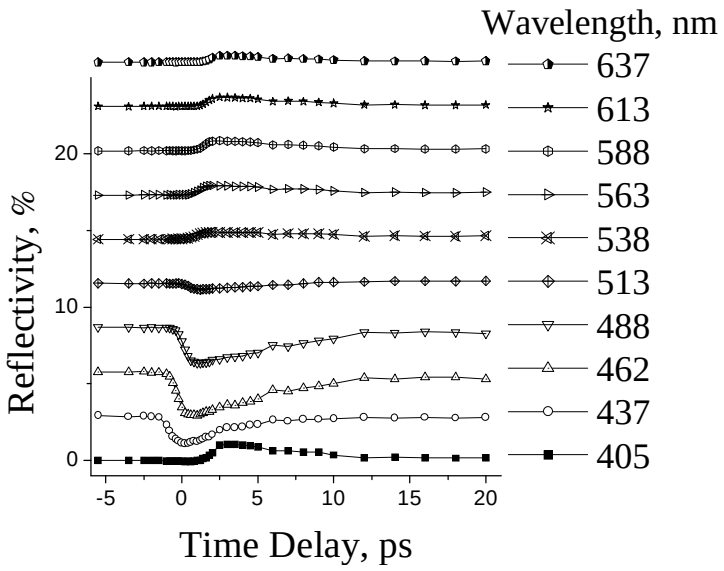

Figure 6.9 The time resolved reflectivity signals constructed from the spectra in Figure 6.8 are shown for different probe wavelengths.

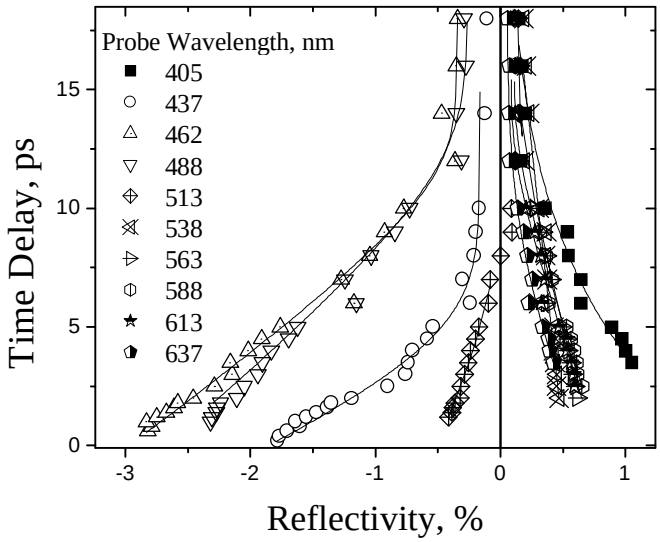

Figure 6.10 The fit of the reflectivity signals shown in Figure 6.9 is illustrated for different probe wavelengths. The symbols and solid lines represent the data points and the fitted curves, respectively.

The extracted electron-phonon coupling constant values are plotted against wavelength in Figure 6.11. Although the error bars are in some cases quite large, the values are seen to depend upon the probe wavelength. Similar scatter was observed in the values obtained for the electron-phonon equilibration temperature (not shown). This emphasises the importance of developing a proper model for the sample reflectivity function before making any physical interpretation of the time resolved signals, particularly in the vicinity of the interband transition. Without such a model, the relaxation times extracted in the previous section of this chapter cannot be reliably interpreted.

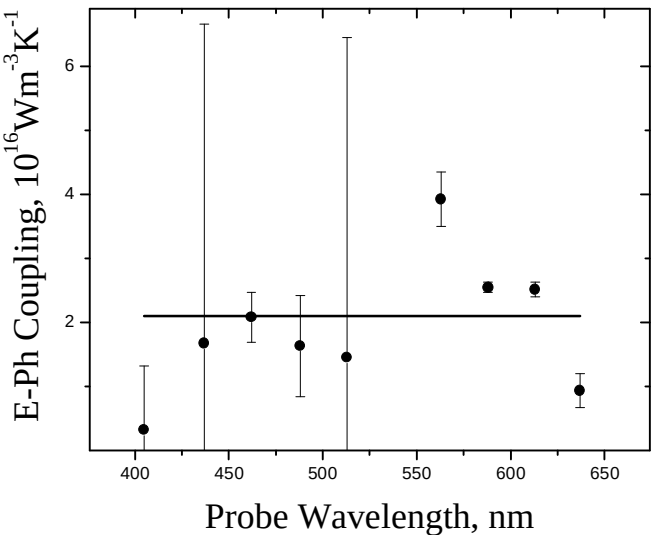

Figure 6.11 The values of the electron-phonon coupling constant extracted from the fittings shown in Figure 6.10 are plotted against the probe wavelength. The solid line denotes the value of the constant derived in Ref. 9.

6.4 Summary

In this chapter, two analytical solutions of the two temperature model equations have been derived in the low and high perturbation limits, respectively. The non-Fermi electron relaxation was treated in the relaxation time approximation. It was shown that the relaxation times that describe the decay of the transient temperature may have a mixed character, being associated with a combination of electron-phonon relaxation and diffusive heat transport into the bulk of the film. The solutions were used for the analysis of reflectivity data obtained in both single colour and two colour experiments. The relaxation times were extracted for the different processes contributing to the electron relaxation. However, the results of the two colour measurements showed that the interpretation of the relaxation times may not be reliable unless a proper model for the dependence of the reflectivity upon the electron temperature is used. One interesting feature of the data is the appearance of oscillations observed within the reflectivity response of Zr that we ascribe to the excitation of a coherent transverse optical phonon by the pump pulse.

Summary

Generally, if a system is subject to a perturbation with duration short on the time scales of its internal dynamics, then it enters a non-equilibrium (transient) state. The subsequent dynamics and relaxation of the system can be then traced using a suitable probe that is sensitive to the state of the system and which also has duration short compared to the characteristic time scales of the dynamics and relaxation. Precessional magnetisation dynamics in a magnetic sample can be excited by magnetic pulses that have a rise time shorter than the period of the precession. Electron dynamics in a sample of an arbitrary nature can be excited by an incident light pulse with duration shorter than the electron relaxation time. In this thesis, dynamics of each type have been investigated in thin metallic films and elements, using both experimental and theoretical methods.

In chapter 3, an analytical theory of macrospin magnetisation dynamics in response to a pulsed magnetic field was developed for a ferromagnetic exchange coupled double layer element of square shape. The dynamics are characterised by the presence of two coupled precessional modes. Analytical expressions were derived for the mode frequencies and damping, and the signal shape in the frequency and time domains. The application of the results was demonstrated through the description of experimental data obtained from a thin magnetic film, a sheet spin valve sample, and a square magnetic element.

Chapter 4 was devoted to investigations of the magnetisation dynamics in micron sized arrays of nanosized magnetic elements by time resolved scanning Kerr microscopy and numerical simulations. The main result of this chapter was the observation of a crossover from the uniform mode precession to precession localised

near the edges of the elements as the size of the elements was reduced. The crossover occurs at an element size of 220 nm, for which the two modes of precession make approximately equal contributions to the signal. The edge mode is confined by the enhanced demagnetising field near the edges perpendicular to the external static field. The demagnetised regions occupy a larger relative area of the element as its aspect ratio is reduced. The conclusion that the dynamics of the magnetic nanoelements are spatially nonuniform may have a significant impact upon magnetic data storage technology.

In chapter 5, a new technique for measurements of the electron linear and angular momentum relaxation times was developed. It was based upon femtosecond ellipsometric measurements of the sample response to an elliptically polarised pump pulse. In this case, the different time scales for the electron angular and linear momentum relaxation reveal themselves through a time shift between the specular inverse Faraday effect (SIFE) and specular optical Kerr effect (SOKE) contributions to the signal. The relative magnitude of the two contributions depends on whether the transient rotation or ellipticity is measured. The shape of the individual contributions depends upon the details of the electronic and optical properties of the sample at the wavelength of the pump and probe pulses. The measurements were performed upon eight different thin film samples of noble and transition metals (Cu, Ag, Au, Ni, Pd, Ti, Zr, and Hf). For each sample, characteristic relaxation times for the electronic angular and linear momentum were extracted using a specially developed theoretical model. The magnitudes of the measured SIFE and SOKE contributions were used to extract the values of the non-vanishing components of the third-order optical susceptibility tensor. A systematic dependence of the signal character and the extracted parameter values upon the underlying electronic structure was revealed. The values of the relaxation times and the components of the third-order optical susceptibility tensor are expected to

be important for the design of hot electron devices and all-optical switches, respectively. The observed correlation between an elements response and its electronic structure will impact future understanding of non-linear processes in metals, and may stimulate theoretical research in this direction. The capability of this new technique could be further enhanced through the use of shorter pulses and by tuning the wavelength of pump and probe, so that the mechanisms responsible for linear and angular momentum relaxation in metals may be explored and understood.

In chapter 6, analytical solutions of the two temperature model in the low and high perturbation limits were obtained and applied in the description of single and two colour pump-probe reflectivity measurements. In the former type of measurement, the relaxation times underlying the response of the Cu, Au, Pd, Ti, Zr, and Hf samples were extracted. However, the results of the two colour experiment have shown that the relaxation times may not be reliably interpreted without proper modelling of the dependence of the sample reflectivity upon the electron temperature and probe wavelength. Terahertz frequency oscillations were observed in the reflectivity response of the Zr sample, and interpreted as a coherently excited transverse optical phonon. The results of this chapter could be used in the design of media for heat assisted magnetic recording where efficient heat sinks are of key importance.

In conclusion, a rich variety of experimental data has been collected within this thesis, and the first steps have been taken towards developing an understanding of underlying physical phenomena. In my opinion, the main direction for future investigation lies in developing theoretical models allowing reliable quantitative analyses of the data. Regerding the reflectivity measurements, the main problem lies in relating the transient reflectivity signal to the transient temperature. For the femtosecond ellipsometry, a theory relating the observed temporal form of the signal to the underlying electronic properties is needed. For the time resolved scanning Kerr

microscopy studies of the magnetisation dynamics in arrays of small elements, simulations of the dynamics of the arrays rather than just single elements and tuning of the exchange parameter are required, although this will only become feasible when faster machines become available. From the experimental point of view, it would be interesting to study the element arrays with a technique that provides enhanced spatial resolution. Given the low frequency of some of the observed modes, the time resolved X-ray magnetic circular dichroism may be a suitable technique although near field magneto-optical techniques could be required at higher frequencies. For the femtosecond ellipsometry, in addition to the extensions mentioned above, it would be interesting to study a greater variety of elements in order to see how far the observed trends extend. For the reflectivity, two colour studies of transition metal samples would be particularly interesting, since they generally possess a rich band structure in the visible range.

Bibliography

1 P.M.W. French, “The Generation of Ultrashort Laser Pulses”, Rep. Progr. Phys. **58**, 169 (1995).

2 R.J. Hicken, “Ultrafast Nanomagnets: Seeing Data Storage in a New Light”, Philos. Trans. Roy. Soc. A **361**, 2827 (2003).

3 H. Petek and S. Ogawa, “Femtosecond Time-Resolved Two-Photon Photoemission Studies of Electron Dynamics in Metals”, Progr. Surf. Sci. **56**, 239 (1997).

4 J. Hohlfeld, U. Conrad, J.G. Müller, S.S. Wellershoff, and E. Matthias, “Femtosecond Time-Resolved Linear and Second-Order Reflectivity of Metals”, in *Nonlinear Optics in Metals*, Edited by K.H. Bennemann, Clarendon, Oxford, 1998.

5 M.R. Freeman and W.K. Hiebert, “Stroboscopic Microscopy of Magnetic Dynamics”, Top. Appl. Phys. **83**, 93 (2001).

6 A. Barman, V.V. Kruglyak, R.J. Hicken, A. Kundrotaite, and M. Rahman, “Anisotropy, Damping, and Coherence of Magnetization Dynamics in a 10 µm Square $Ni_{81}Fe_{19}$ Element”, Appl. Phys. Lett. **82**, 3065 (2003).

7 S.D. Brorson, A. Kazeroonian, J.S. Moodera, D.W. Face, T.K. Cheng, E.P. Ippen, M.S. Dresselhaus, and G. Dresselhaus, “Femtosecond Room-Temperature Measurement of the Electron-Phonon Coupling Constant λ in Metallic Superconductors”, Phys. Rev. Lett. **64**, 2172 (1990).

8 N.I. Zheludev, P.J. Bennet, H. Loh, S.V. Popov, I.R. Shatwell, Y.P. Svirko, V.E. Gusev, V.F. Kamalov, and E.V. Slobodchikov, “Cubic Optical Nonlinearity of Free Electrons in Bulk Gold”, Opt. Lett. **20**, 1368 (1995).

9 J. Hohlfeld, S.S. Wellershoff, J. Gudde, U. Conrad, V. Jahnke, and E. Matthias, “Electron and Lattice Dynamics Following Optical Excitation of Metals”, Chem. Phys. **251**, 237 (2000).

10 G.P. Zhang, W. Hübner, E. Beaurepaire, and J.-Y. Bigot, “Laser-Induced Ultrafast Demagnetization: Ferromagnetism, a New Frontier?”, Top. Appl. Phys. **83**, 245 (2001).

11 A. Melnikov, I. Radu, U. Bovensiepen, O. Krupin, K. Starke, E. Matthias, and M. Wolf., “Coherent Optical Phonons and Parametrically Coupled Magnons Induced by Femtosecond Laser Excitation of the Gd(0001) Surface”, Phys. Rev. Lett. **91**, 227403 (2003).

12 J.-G. Zhu and Y. Zheng, “The Micromagnetics of Magnetoresistive Random Access Memory”, Top. Appl. Phys. **83**, 289 (2001).

13 S.E. Russek, R.D. McMichael, M.J. Donahue, and S. Kaka, “High Speed Switching and Rotational Dynamics in Small Magnetic Thin Film Devices”, Top. Appl. Phys. **87**, 93 (2003).

14 B. Heinrich and J.A.C. Bland (Editors), *Ultrathin Magnetic Structures IV: Applications of Nanomagnetism*, Springer-Verlag, Berlin, 2004.

15 M.L. Plumer, J. van Ek, D. Weller (Editors), *The Physics of Ultrahigh-Density Magnetic Recording*, Springer-Verlag, Berlin, 2001.

16 W.K. Hiebert, G.E. Vallentine, and M.R. Freeman, “Comparison of Experimental and Numerical Micromagnetic Dynamics in Coherent Precessional Switching and Modal Oscillations”, Phys. Rev. B **65**, R140404 (2002).

17 T. Gerrits, H.A.M. van den Berg, J. Hohlfeld, L. Bar, T. Rasing, “Ultrafast Precessional Magnetization Reversal by Picosecond Magnetic Field Pulse Shaping”, Nature **418**, 509 (2002).

18 W.K. Hiebert, G.E. Ballentine, L. Lagae, R.W. Hunt, and M.R. Freeman, “Ultrafast Imaging of Incoherent Rotation Magnetic Switching with Experimental and Numerical Micromagnetic Dynamics”, J. Appl. Phys. **92**, 392 (2002).

19 I.V. Baryakhtar and V.G. Baryakhtar, “A Motion Equation for Magnetization: Dynamics and Relaxation” Ukr. J. Phys. **43**, 1433 (1998).

20 D.L. Mills and S.M. Rezende, “Spin Damping in Ultrathin Magnetic Films”, Top. Appl. Phys. **87**, 27 (2003).

21 E. Beaurepaire, J.-C. Merle, A. Daunois, and J.-Y. Bigot, “Ultrafast Spin Dynamics in Ferromagnetic Nickel”, Phys. Rev. Lett. **76**, 4250 (1996).

22 E. Beaurepaire, M. Maret, V. Halté, J.-C. Merle, A. Daunois, and J.-Y. Bigot, "Spin Dynamics in $CoPt_3$ Alloy Films: A Magnetic Phase Transition in the Femtosecond Time Scale", Phys. Rev. B **58**, 12134 (1998).

23 J. Hohlfeld, Th. Gerrits, M. Bilderbeek, Th. Rasing, H. Awano, and N. Ohta, "Fast Magnetization Reversal of GdFeCo Induced by Femtosecond Laser Pulses", Phys. Rev. B **65**, 12413 (2001).

24 Y.I. Gorobets, Y.I. Dzhezherya, and A.F. Kravets, "Magnetization reversal of ferromagnetic granules by field of circularly-polarized electromagnetic waves", Metallofiz. Nov. Techn. **25**, 27 (2003).

25 M. van Kampen, C. Jozsa, J.T. Kohlhepp, P. LeClair, L. Lagae, W.J.M. de Jonge, and B. Koopmans, "All-Optical Probe of Coherent Spin Waves", Phys. Rev. Lett. **88**, 227201 (2002).

26 Q. Zhang, A.V. Nurmikko, A. Anguelouch, G. Xiao, and A. Gupta, "Coherent Magnetization Rotation and Phase Control by Ultrashort Optical Pulses in CrO_2 Thin Films", Phys. Rev. Lett. **89**, 177402 (2002).

27 G.Ju, A.V. Nurmikko, R.F.C. Farrow, R.F. Marks, M.J. Carey, and B.A. Gurney, "Ultrafast Time Resolved Photoinduced Magnetization Rotation in a Ferromagnetic/Antiferromagnetic Exchange Coupled System", Phys. Rev. Lett. **82**, 3705 (1999).

28 T. Rasing, H. van der Berg, T. Gerrits, and J. Hohlfeld, "Ultrafast Magnetization and Switching Dynamics", Top. Appl. Phys. **87**, 213 (2003).

29 A. Barman, V.V. Kruglyak, R.J. Hicken, C.H. Marrows, M. Ali, A. Hindmarch, and B.J. Hickey, "Characterization of Spin Valves Fabricated on Opaque Substrates by Optical Ferromagnetic Resonance", Appl. Phys. Lett. **81**, 1468 (2002).

30 A. Barman, V.V. Kruglyak, R.J. Hicken, A. Kundrotaite, and M. Rahman, "Observation of Incoherent Picosecond Magnetisation Dynamics in Micron Sized $Ni_{81}Fe_{19}$ Elements by Time Resolved Scanning Kerr Effect Microscopy", IEE Proc.-Sci. Meas. Technol. **150**, 261 (2003).

31 R.J. Hicken, A. Barman, V.V. Kruglyak, and S. Ladak, "Optical Ferromagnetic Resonance Studies of Thin Film Magnetic Structures", J. Phys. D: Appl. Phys. **36**, 2183 (2003).

32 A. Barman, V.V. Kruglyak, R.J. Hicken, A. Kundrotaite, and M. Rahman, "Shape Dependent Anisotropy and Damping of Picosecond Magnetisation Dynamics in a Micron Sized $Ni_{81}Fe_{19}$ Element", J. Magn. Magn. Mater. **272-276**, 2121 (2004).

33 A. Barman, V.V. Kruglyak, R.J. Hicken, J.M. Rowe, J. Scott, A. Kundrotaite, and M. Rahman, "Imaging the Dephasing of the Spin Wave Modes of a Square Thin Film Magnetic Element", Phys. Rev. B **69**, 174426 (2004).

34 A. Barman, V.V. Kruglyak, R.J. Hicken, J. Scott, A. Kundrotaite, and M. Rahman, "Dependence of anisotropy and damping on shape and aspect ratio in micron sized $Ni_{81}Fe_{19}$ elements", J. Appl. Phys. **95**, 6998 (2004).

35 A. Hubert, R. Schäfer, *Magnetic Domains: the Analysis of Magnetic Microstructures*, Springer-Verlag, Berlin, 1998.

36 P. Langevin, "Magnétisme et Théorie de Électrons", Ann. Chim. Phys. **5**, 70 (1905).

37 P. Weiss, "L'Hypothèse du Cham Moléculaire et la Propriété Ferromagnétique", J. de Phys. Rad. **6**, 661 (1907).

38 W. Heisenberg, "Zur Theorie des Ferromagnetismus", Z. Phys. **49**, 619 (1928).

39 J. Dorfman, Nature **119**, 353 (1928).

40 J. Frenkel, Z. Phys. **49**, 31 (1928).

41 N.S. Akulov, "Zur Theorie der Magnetisierungskurve von Einkristallen", Z. Phys. **67**, 794 (1931).

42 R. Becker, "Zur Theorie der Magnetisierungskurve", Z. Phys. **62**, 253 (1930).

43 K. Honda and S. Kaya, Sci. Rep. Tohoku Imp. Univ. **15**, 721 (1926).

44 J. Frenkel and J. Dorfman, "Spontaneous and Induced Magnetization in Ferromagnetic Bodies", Nature **126**, 274 (1930).

45 F. Bloch, "Zur Theorie des Austauschproblems und der Remanenzerscheinung der Ferromagnetika" Z. Phys. **74**, 295 (1932).

46 W. Heisenberg, "Zur Theorie der Magnetostriktion und der Magnetisierungskurve", Z. Phys. **69**, 287 (1931).

47 L.D. Landau and E.M. Lifshitz, "On the Theory of the Dispersion of Magnetic Permeability in Ferromagnetic Bodies", Phys. Zs. der Sowjetunion. **8**, 153 (1935).

48 W.F. Brown, “Theory of the Approach to Magnetic Saturation”, Phys. Rev. **58**, 736 (1940).

49 A. Aharoni, *Introduction to the Theory of Ferromagnetism*, Oxford University Press, Oxford, 2000.

50 V.G. Baryakhtar and Y.I. Gorobets, *Cylindrical Magnetic Domains and Their Lattices*, Naukova Dumka, Kiyv, 1988 (in Russian).

51 D.L. Mills, “Thermodynamic Properties of Ultrathin Magnetic Structures”, in *Ultrathin Magnetic Structures I*, Edited by B. Heinrich and J.A.C. Bland, Springer-Verlag, Berlin, 1994.

52 G. Bertotti, *Hysteresis in Magnetism*, Academic Press, San Diego, 1998.

53 A.H. Morrish, The Physical Principles of Magnetism, John Wiley & and Sons, New York, 1965.

54 A.I. Akhiezer, V.G. Baryakhtar and S.V. Peletminskii, *Spin waves*, North Holland, Amsterdam, 1968.

55 B. Heinrich and J.A.C. Bland (Editors), *Ultrathin Magnetic Structures I*, Springer-Verlag, Berlin, 2004.

56 A.G. Gurevich and G.A. Melkov, *Magnetization oscillations and waves*, CRC Press, Boca Raton, 1996.

57 T.L. Gilbert, Phys. Rev. **100**, 1243 (1955).

58 C. Kittel, “On the Theory of Ferromagnetic Resonance Absorption”, Phys. Rev. **73**, 155 (1948).

59 K.Y. Guslienko, S.O. Demokritov, B. Hillebrands, and A.N. Slavin, “Effective Dipolar Boundary Conditions for Dynamic Magnetization in Thin Magnetic Stripes”, Phys. Rev. B **66**, 132402 (2002).

60 L.R. Walker, “Magnetostatic Modes in Ferromagnetic Resonance”, Phys. Rev. **105**, 390 (1957).

61 R.W. Damon and J.R. Eshbach, “Magnetostatic Modes of a Ferromagnetic Slab”, J. Phys. Chem. Solids **19,** 308 (1961).

62 M. Donahue and D.G. Porter, OOMMF User's Guide, Version 1.0, Interagency Report NISTIR 6376, NIST, Gaithersburg, MD, 1999: URL: http://math.nist.gov/oommf.

63 M. Born and E. Wolf, *Principles of Optics: Electromagnetic Theory of Propagation, Interference and Diffraction of Light*, Cambridge University Press, 1999.

64 Z.Q. Qiu and S.D. Bader, "Kerr Effect and Surface Magnetism", in *Nonlinear Optics in Metals*, Edited by K.H. Bennemann, Clarendon, Oxford, 1998.

65 S.D. Bader and J.L. Erskine, "Magneto-Optical Kerr Effect in Ultrathin Magnetic Structures", in *Ultrathin Magnetic Structures II*, Edited by B. Heinrich and J.A.C. Bland, Springer-Verlag, Berlin, 1994.

66 G. Metzger, P. Pluvinage, and R. Tourget, Ann. Phys. **10**, 5 (1965).

67 J. Wu, J.R. Moore, and R.J. Hicken, "Optical Pump-Probe Studies of the Rise and Damping of Ferromagnetic Resonance Oscillations in a Thin Fe Film", J. Magn. Magn. Mater. **222**, 189 (2000).

68 J.-Y. Bigot, "Femtosecond Magneto-Optical Processes in Metals", C. R. Acad. Sci. Paris, Série IV **2**, 1483 (2001).

69 F. Vallée, "Ultrafast spectroscopy of metals", C. R. Acad. Sci. Paris, Série IV **2**, 1469 (2001).

70 P. van Hall, "Ultrafast Processes in Ag and Au: A Monte Carlo Study", Phys. Rev. B **63**, 104301 (2001).

71 S.I. Anisimov, B.L. Kapeliovich, and T.L. Perelman, Zh. Eksp. Teor. Fiz. **66**, 776 (1974) [Sov. Phys. JETP **39**, 375 (1975)].

72 C.-K. Sun, F. Vallée, L.H. Acioli, E.P. Ippen, and J.G. Fujimoto, "Femtosecond-Tunable Measurement of Electron Thermalization in Gold", Phys. Rev. B **50**, 15337 (1994).

73 E. Knoesel, A. Hotzel, and M. Wolf, "Ultrafast Dynamics of Hot Electrons and Holes in Copper: Excitation, Energy Relaxation, and Transport effects", Phys. Rev. B **57**, 12812 (1998).

74 S. Link, H.A. Durr, and W. Eberhardt, "Femtosecond Spectroscopy", J. Phys.: Cond. Matt. **13**, 7873 (2001).

75 S.V. Popov, Y.P. Svirko, and N.I. Zheludev, “Pump-Probe Reflective Polarization-Sensitive Nonlinear Optics”, J. Opt. Soc. Am. B **13**, 2729 (1996); Y.P. Svirko and N.I. Zheludev, *Polarization of Light in Nonlinear Optics*, Wiley, New York, 1998.

76 R. Wilks, “Measurements of Linear and Circular Birefringence in Metals by Femtosecond Optical Pump-Probe Spectroscopy”, PhD Thesis, Exeter, 2003.

77 J. Wu, “Optical Pump-Probe Studies of Spin Dynamics in Ferromagnetic Materials”, PhD Thesis, Exeter, 2001.

78 U.D. Keil, H.J. Gerritsen, J.E.M. Haverkort, and J.H. Wolter, “Generation of Ultrashort Electrical Pulses with Variable Pulse Widths”, Appl. Phys. Lett. **66**, 1629 (1995).

79 M. Bauer, R. Lopusnik, J. Fassbender, and B. Hillebrands, “Suppression of Magnetic-Field Pulse-Induced Magnetization Precession by Pulse Tailoring”, Appl. Phys. Lett. **76**, 2758 (2000).

80 H.W. Schumacher, C. Chappert, P. Crozat, R.C. Sousa, P.P. Freitas, and M. Bauer, “Coherent Suppression of Magnetic Ringing in Microscopic Spin Valve Elements”, Appl. Phys. Lett. **80**, 3781 (2002).

81 B. Koopmans, “Laser-Induced Magnetization Dynamics”, Top. Appl. Phys. **87**, 253 (2003).

82 T. Kampfrath, R.G. Ulbrich, F. Leuenberger, M. Münzenberg, B. Sass, and W. Felsch, “Ultrafast Magneto-Optical Response of Iron Thin Films”, Phys. Rev. B **65**, 104429 (2002).

83 R. Wilks, N.D. Hughes, and R.J. Hicken, “Investigation of Ultrafast Spin Dynamics in a Ni Thin Film”, J. Appl. Phys. **91**, 8670 (2002).

84 B. Heinrich, “Ferromagnetic Resonance in Ultrathin Film Structures”, in *Ultrathin Magnetic Structures II*, Edited by B. Heinrich and J.A.C. Bland, Springer-Verlag, Berlin, 1994.

85 J.F. Gregg, “Frequency Domain Magnetic Measurements from Kilohertz to Gigahertz”, Top. Appl. Phys. **83**, 217 (2001).

86 B. Hillebrands and G. Güntherodt, “Brillouin Light Scattering in Magnetic Superlattices”, in *Ultrathin Magnetic Structures II*, Edited by B. Heinrich and J.A.C. Bland, Springer-Verlag, Berlin, 1994.

87 S.O. Demokritov and B. Hillebrands, “Spin Waves in Larerally Confined Magnetic Structures”, Top. Appl. Phys. **83**, 65 (2001).

88 K.B. Hathaway, “Theory of Exchange Coupling in Magnetic Multilayers”, in *Ultrathin Magnetic Structures II*, Edited by B. Heinrich and J.A.C. Bland, Springer-Verlag, Berlin, 1994.

89 J. Fassbender, “Magnetization Dynamics Investigated by Time-Resolved Kerr Effect Magnetometry”, Top. Appl. Phys. **87**, 59 (2003).

90 T.M. Crawford, T.M. Silva, C.W. Teplin, and C.T. Rogers, ”Subnanosecond Magnetization Dynamics Measured by the Second-Harmonic Magneto-Optic Kerr Effect”, Appl. Phys. Lett. **74**, 3386 (1999).

91 S. Pizzini, J. Vogel, M. Bonfim, and A. Fontain, “Time-Resolved X-Ray Magnetic Circular Dichroism – A Selective Probe of Magnetization Dynamics on Nanosecond Timescales”, Top. Appl. Phys. **87**, 155 (2003).

92 H.W. Schumacher, C. Chappert, R.C. Sousa, P.P. Freitas, and J. Miltat, “Quasiballistic Magnetization Reversal”, Phys. Rev. Lett. **90**, 17204 (2002).

93 T.J. Silva, C.S. Lee, T.M. Crawford, and C.T. Rogers, “Inductive Measurement of Ultrafast Magnetization Dynamics in Thin-Film Permalloy”, J. Appl. Phys. **85**, 7849 (1999).

94 M. Covington, T.M. Crawford, and G.J. Parker, “Time-Resolved Measurement of Propagating Spin Waves in Ferromagnetic Thin Films”, Phys. Rev. Lett. **89**, 237202 (2002).

95 A.B. Kos, J.P. Nibarger, R. Lopusnik, T. J. Silva, and Z. Celinski, “Cryogenic Pulsed Inductive Microwave Magnetometer”, J. Appl. Phys. **93**, 7068 (2003).

96 J. Wu, N.D. Hughes, J.R. Moore, and R.J. Hicken, “Excitation and Damping of Spin Excitations in Ferromagnetic Thin Films”, J. Magn. Magn. Mater. **241**, 96 (2002).

97 T.M. Crawford, P. Kabos, and T.J. Siva, “Coherent Control of Precessional Dynamics in Thin Film Permalloy”, Appl. Phys. Lett. **76**, 2113 (2000).

98 J. Wu, D.S. Schmool, N.D. Hughes, J.R. Moore, and R.J. Hicken, "Picosecond Large Angle Reorientation of the Magnetization in $Ni_{81}Fe_{19}$ Circular Thin-Film Elements", J. Appl. Phys. **91**, 278 (2002).

99 W.K. Hiebert, A. Stankiewicz, and M.R. Freeman, "Direct Observation of Magnetic Relaxation in a Small Permalloy Disk by Time-Resolved Scanning Kerr Microscopy", Phys. Rev. Lett. **79**, 1134 (1997).

100 Y. Acremann, C.H. Back, M. Buess, O. Portmann, A. Vaterlaus, D. Pescia, and H. Melchior, "Imaging Precessional Motion of the Magnetization Vector", Science **290**, 492 (2000).

101 Y. Acremann, A. Kashuba, M. Buess, D. Pescia, and C.H. Back, "Magnetic Spatial Non-Uniformities on the Picosecond Timescale", J. Magn. Magn. Mater. **239**, 346 (2002).

102 J.P. Park, P. Eames, D.M. Engebretson, J. Berezovsky, and P.A. Crowell, "Spatially Resolved Dynamics of Localized Spin-Wave Modes in Ferromagnetic Wires", Phys. Rev. Lett. **89**, 277201 (2002).

103 J. Zak E.R. Moog, C. Liu, and S.D. Bader, "Magneto-Optics of Multilayers with Arbitrary Magnetization Directions", Phys. Rev. B **43**, 6423 (1991).

104 A. Moser, K. Takano, D.T. Margulies, M. Albrecht, Y. Sonobe, Y. Ikeda, S.H. Sun, and E.E. Fullerton, "Magnetic Recording: Advancing into the Future", J. Phys. D: Appl. Phys. **35**, R157 (2002).

105 M. Belov, Z. Liu, R. D. Sydora, and M. R. Freeman, "Modal Oscillation Control in Internally Patterned $Ni_{80}Fe_{20}$ Thin Film Microstructures", Phys. Rev. B. **69**, 94414 (2004).

106 J. Jorzick, S.O. Demokritov, B. Hillebrands, M. Bailleul, C. Fermon, K.Y. Guslienko, A.N. Slavin, D.V. Berkov, and N.L. Gorn, "Spin Wave Wells in Nonellipsoidal Micrometer Size Magnetic Elements", Phys. Rev. Lett. **88**, 47204 (2002).

107 S. Tamaru, J.A. Bain, R.J.M. van de Veerdonk, T.M. Crawford, M. Covington, and M.H. Kryder, "Imaging of Quantized Magnetostatic Modes Using Spatially Resolved Ferromagnetic Resonance", J. Appl. Phys. **91**, 8034 (2002).

108 S. Jung, B. Watkins, L. DeLong, J.B. Ketterson, and V. Chandrasekhar, "Ferromagnetic Resonance in Periodic Particle Arrays", Phys. Rev. B **66**, 132401 (2002).

109 Y. Zhai, J. Shi, X.Y. Zhang, L. Shi, Y.X. Xu, H.B. Haung, Z.H. Lu, and H.R. Zhai, "A Study of the Non-Uniform Effect on the Shape Anisotropy in Patterned NiFe Films of Ferromagnetic Resonance", J. Phys.: Cond. Matter **14**, 7865 (2002).

110 G.N. Kakazei, P.E. Wigen, K.Yu. Guslienko, V. Novosad, A.N. Slavin, V.O. Golub, N.A. Lesnik, and Y. Otani, "Spin-Wave Spectra of Perpendicularly Magnetized Circular Submicron Dot Arrays", Appl. Phys. Lett. **85**, 443 (2004).

111 T.M. Crawford, M. Covington, and G.J. Parker, "Time-Domain Excitation of Quantized Magnetostatic Spin-Wave Modes in Patterned NiFe Thin Film Ensembles", Phys. Rev. B **67**, 24411 (2003).

112 C. Kittel, "Excitation of Spin Waves in a Ferromagnet by a Uniform rf Field", Phys. Rev. **110**, 1295 (1958).

113 B.A. Kalinikos and A.N. Slavin, "Theory of Dipole-Exchange Spin-Wave Spectrum for Ferromagnetic Films with Mixed Exchange Boundary Conditions", J. Phys. C **19**, 7013 (1986).

114 P.H. Bryant, J.F. Smyth, S. Schultz, and D.R. Fredkin, "Magnetostatic-Mode Spectrum of Rectangular Ferromagnetic Particles", Phys. Rev. B **47**, 11255 (1993).

115 A. Aharoni, "Demagnetizing Factors for Rectangular Ferromagnetic Prisms", J. Appl. Phys. **83**, 3432 (1998).

116 J. Miltat, G. Albuquerque, and A. Thiaville, "An Introduction to Micromagnetics in the Dynamic Regime", Top. Appl. Phys. **83**, 1 (2001).

117 S. Jung, J.B. Ketterson, and V. Chandrasekhar, "Micromagnetic calculations of ferromagnetic resonance in submicron ferromagnetic particles", Phys. Rev. B **66**, 132405 (2002).

118 F. Schreiber and Z. Frait, "Spin-Wave Resonance in High-Conductivity Films: The Fe-Co Alloy System", Phys. Rev. B **54**, 6473 (1996).

119 R. Jansen, "The Spin-Valve Transistor: A Review and Outlook", J. Phys. D **36**, R289 (2003).

120 R. Knorren, G. Bouzerar, and K.H. Bennemann, “Theory for the Dynamics of Excited Electrons in Noble and Transition Metals”, J. Phys.: Cond. Matt. **14**, R739 (2002).

121 Q.F. Zhang, W.M. Liu, Z.Q. Xue, J.L. Wu, S.F. Wang, D.L. Wang, and Q.H. Gong, “Ultrafast Optical Kerr effect of Ag–BaO Composite Thin Films”, Appl. Phys. Lett. **82**, 958 (2003).

122 G. Ma, J. He, and S.-H. Tang, “Femtosecond Nonlinear Birefringence and Nonlinear Dichroism in Au:TiO_2 Composite Films”, Phys. Lett. A **306**, 348 (2003).

123 H.I. Elim, W. Ji, A.H. Yuwono, J.M. Xue, and J. Wang, “Ultrafast Optical Nonlinearity in Poly(methylmethacrylate)-TiO_2 Nanocomposites”, Appl. Phys. Lett. **82**, 2691 (2003).

124 G.V. Prakash, M. Cazzanelli, Z. Gaburro, L. Pavesi, F. Iacona, G. Franzò, and F. Priolo, “Nonlinear Optical Properties of Silicon Nanocrystals Grown by Plasma-Enhanced Chemical Vapor Deposition”, J. Appl. Phys. **91**, 4607 (2002).

125 Q. Chen, E.H. Sargent, N. Leclerc, and A.-J. Attias, “Ultrafast Nonresonant Third-Order Optical Nonlinearity of a Conjugated 3,3’-bipyridine Derivative from 1150 to 1600 nm”, Appl. Phys. Lett. **82**, 4420 (2003).

126 P.J. Bennet, S. Dhanjal, Y.P. Svirko, and N.I. Zheludev NI, “Cubic Optical Nonlinearities of Metals in the Vicinity of the Melting Point”, J. Modern Opt. **45**, 1009 (1998).

127 P.J Bennett, A. Malinowski, B.D. Rainford, I.R. Shatwell, Y.P. Svirko, and N.I. Zheludev, “Femtosecond Pulse Duration Measurements Utilizing an Ultrafast Nonlinearity of Nickel”, Opt. Comm. **147**, 148 (1998).

128 P.J Bennett, V. Albanis, Y.P. Svirko, and N.I. Zheludev, “Femtosecond Cubic Optical Nonlinearity of Thin Nickel Films”, Opt. Lett. **24**, 1373 (1999).

129 R. Wilks, R.J. Hicken, M. Ali, B.J. Hickey, J.D.R. Buchanan, A.T.G. Pym, and B.K. Tanner, “Investigation of Ultrafast Demagnetization and Cubic Optical Nonlinearity of Ni in the Polar Geometry”, J. Appl. Phys. **95**, 7441 (2004).

130 R. Wilks and R.J. Hicken, “Transient Optical Polarization Response of Aluminium at an Interband Transition”, J. Phys.: Condens. Matt. **16**, 4607 (2004).

131 A.V. Kimel, F. Bentivegna, V.N. Gridnev, V.V. Pavlov, R.V. Pisarev, and Th. Rasing, “Room-Temperature Ultrafast Carrier and Spin Dynamics in GaAs Probed by the Photoinduced Magneto-Optical Kerr Effect”, Phys. Rev. B **63**, 235201 (2001).

132 G.A. Burdick, “Energy Band Structure of Copper”, Phys. Rev. **129**, 138 (1967); N.E. Christensen and B.O. Seraphin, “Relativistic Band Calculation and the Optical Properties of Gold”, Phys. Rev. B **4**, 3321 (1971); H. Eckardt, L. Fritsche, and J. Noffke, J. Phys. F: Met. Phys. **14**, 97 (1984).

133 D.W. Lynch, C.G. Olson, and J.H. Weaver, “Optical Properties of Ti, Zr, and Hf from 0.15 to 30 eV”, Phys. Rev. B **11**, 3617 (1975).

134 P.B. Johnson and R.W. Christy, “Optical Constants of Transition Metals: Ti, V, Cr, Mn, Fe, Co, Ni, and Pd”, Phys. Rev. B **9**, 5056 (1974).

135 J.H. Weaver, “Optical Properties of Rh, Pd, Ir, and Pt”, Phys. Rev. B **11**, 1416 (1975); J.H. Weaver and R.L. Benbow, “Low-Energy Interband Absorption in Pd”, Phys. Rev. B **12**, 3509 (1975).

136 E.D. Pawlik (Editor), *Handbook of Optical Constants of Solids*, Academic Press, London, 1985.

137 R.W. Schoenlin, W.Z. Lin, J.G. Fujimoto, and G.L. Eesley, “Femtosecond Studies of Nonequilibrium Electronic Processes in Metals”, Phys. Rev. Lett. **58**, 1680 (1987).

138 H.E. Elsayed-Ali, T.B. Norris, M.A. Pessot, and G.A. Mourou, “Time-Resolved Observation of Electron-Phonon Relaxation in Copper”, Phys. Rev. Lett. **58**, 1212 (1987).

139 R.H.M. Groeneveld, R. Sprik, and A. Lagendijk, “Ultrafast Relaxation of Electrons Probed by Surface Plasmons at a Thin Silver Film”, Phys. Rev. Lett. **64**, 784 (1990).

140 R. Rosei and D.W. Lynch, “Thermomodulation Spectra of Al, Au, and Cu”, Phys. Rev. B **5**, 3883 (1972).

141 V.E. Gusev and O.B. Wright, “Ultrafast Nonequilibrium Dynamics of Electrons in Metals”, Phys. Rev. B **57**, 2878 (1998).

142 A.P. Kanavin, I.V. Smetanin, V.A. Isakov, Yu.V. Afanasiev, B.N. Chichkov, B. Wellegehausen, S. Nolte, C. Momma, and A. Tünnermann, “Heat Transport in Metals Irradiated by Ultrashort Laser Pulses”, Phys. Rev. B **57**, 14698 (1998).

143 A.V. Lugovskoy and I. Bray, “Ultrafast Electron Dynamics in Metals under Laser Irradiation”, Phys. Rev. B **60**, 3279 (1999).

144 B. Rethfeld, A. Kaiser, M. Vicanek and G. Simon, “Ultrafast Dynamics of Nonequilibrium Electrons in Metals under Femtosecond Laser Irradiation”, Phys. Rev. B **65**, 214303 (2002).

145 M. Yamamoto, C.T. Chan, K.M. Ho, M. Kurahashi, and S. Naito, “First-Principles Calculation of the Longitudinal Phonon in the Surface-Normal Direction of a Zirconium(0001) Slab: Localization Mode at the Subsurface”, Phys. Rev. B **53**, 13772 (1996).

146 C. Stassis, J. Zarestky, D. Arch, O.D. McMasters, and B.N. Harmon, “Temperature Dependence of the Normal Vibrational Modes of hcp Zr”, Phys. Rev. B **18**, 2632 (1978).